Nanostructures Templated on Biological Scaffolds for Light Harvesting, Energy Transfer, Charge Transfer, and Redox Reactions

by

Yoon Sung Nam

B.S., Seoul National University (1997)
M.S., Korea Advanced Institute of Science and Technology (1999)

Submitted to the Department of Biological Engineering
in partial fulfillment of the requirements for the degree of

Doctor of Philosophy in Biological Engineering

at the

MASSACHUSETTS INSTITUTE OF TECHNOLOGY
[June 2010]
April 2010

Author .....
Department of Biological Engineering
April 12, 2010

Certified by .....
Angela M. Belcher
Professor
Thesis Supervisor

Accepted by .....
Peter Dedon
Chairman, Department Committee on Graduate Students

Thesis Committee Certification of Approval

of

Nanostructures Templated on Biological Scaffolds for Light Harvesting, Energy Transfer, Charge Transfer, and Redox Reactions

by

Yoon Sung Nam

Graduate Thesis Commitee

Angela M. Belcher, Ph.D.
Germeshausen Professor of Materials Science
and Engineering and Biological Engineering

Scott Manalis, Ph.D.
Professor of Biological Engineering
Thesis Committee Chair

Paula T. Hammond, Ph.D.
Bayer Chair Professor of Chemical Engineering

For my wife, Jihyun Kim, with all my love

Nanostructures Templated on Biological Scaffolds for Light Harvesting, Energy Transfer, Charge Transfer, and Redox Reactions

by

Yoon Sung Nam

Submitted to the Department of Biological Engineering
on April 12, 2010, in partial fulfillment of the
requirements for the degree of
Doctor of Philosophy in Biological Engineering

Abstract

Solar energy provides an unparalleled promise to generate enormous amounts of clean energy. As the solar industry grows rapidly with a focus on power generation, new, but equally important challenges are emerging, including how to store and transfer the generated solar energy. Light-driven water splitting to generate hydrogen has received increasing attention as a means of storing solar energy. However, in order to evolve hydrogen with no energy input beyond sunlight, it is important to develop a stable and efficient catalytic system for water oxidation, which is the more challenging half-reaction of photocatalytic water splitting. Over several billion years, cyanobacteria and plants have evolved highly organized photosynthetic systems for the efficient oxidation of water. Water oxidation by mimicking photosynthesis has been pursued since the early 1970s; however, the approaches have been primarily limited to the extraction and reconstitution of the existing natural pigments, photosystems, and photosynthetic organisms, which suffer from instability. Metal oxide catalysts, often coupled with pigments, are similar to the reaction centers in natural photosystems and have been shown to photochemically oxidize water. Unfortunately, various approaches involving molecular design of ligands, surface modification, and immobilization still show low catalytic efficiencies unless they are used under relatively harsh conditions (*i.e.*, in highly alkaline or acidic solutions under ultraviolet radiation). The current work aims to demonstrate the impact of nano-scale assembly of organic and inorganic molecules on energy and charge transfers, and related redox reactions. Genetically modified M13 viruses are explored as biological scaffolds to guide the formation of metal oxide catalysts-pigments hybrid nanostructures that enable efficient transports of both energy and electrons for photochemical water oxidation. This dissertation deals with three aspects of the virus-templated nanostructures - photonic, photochemical, and electrochemical properties. First, organic pigments are arranged into a one-dimensional light-harvesting antenna on the M13 virus. Chemical grafting of zinc porphyrins to the M13 virus induces spectroscopic

changes, including fluorescence quenching, the extensive band broadening and small red-shift of their absorption spectrum, and the shortened lifetime of the excited states. Based on these optical signatures a hypothetical model is suggested to explain the energy transfer occurring in the supramolecular porphyrin structures templated on the virus. Second, through further genetic engineering of M13 viruses, iridium oxide hydrosol clusters (catalysts) are co-assembled with zinc porphyrins. When illuminated with visible light, this system evolves about 100 oxygen molecules per surface iridium molecule per minute in a prolonged manner. In addition, porous polymer microgels are used as an immobilization matrix to improve the structural durability of the assembled nanostructures and enable the recycling of the materials. The system also maintains a substantial level of its catalytic performance after repeated uses, producing about 1,200 oxygen molecules per molecule of catalyst during 4 cycles. These results suggest that the multiscale assembly of functional components, which can improve energy transfer and structural stability, should be a promising route for significant improvement of photocatalytic water oxidation. Lastly, electrochemical properties of the virus-templated iridium oxide nanowires are examined as an electrochromic film on a transparent conductive electrode. The prepared nanowire film has a highly open porous morphology that facilitates ion transport, and the redox responses of the nanowires are limited by the electron mobility of the nanowire film. These results demonstrate that a bio-templating approach provides a versatile platform for designing complex nanostructures that can facilitate the transport of electrochemical molecules in a broad range of photoelectrochemical devices.

Thesis Supervisor: Angela M. Belcher
Title: Professor

Acknowledgments

I thank my advisor, Professor Angela M. Belcher, for her guidance and encouragement. Her guidance was not like "Follow me" but rather "Let's find together", and that was the reason I could pursue and enjoy many new research ideas with her. M13 bacteriophage is a very interesting biological template explored by her for assembly of diverse molecules for the past decade. In my thesis work I used it as a template for co-assembly of inorganic metal oxides and organic pigments. In a sense the Belcher group plays the same role with M13 bacteriophage as it provides diverse people with a wonderful ground where they are assembled for creative research. The Belcher people have a wide range of academic backgrounds, including Materials Science, Chemistry, Biology, Bioengineering, Chemical Engineering, Electrical Engineering, Mechanical Engineering, and Civil Engineering. It is amazing to see how those people work together in one lab. It sounds like the Belcher Institute! Despite the differences they work together very closely and effectively, and learn completely something new from each other. The Belcher group is a beautiful place for open-minded people who want to pursue something not typical as M13 bacteriophage works a template for assembling materials to create new functionalities and performances. It was my greatest pleasure of being surrounded by such diverse, intellectual people who know how to communicate and interact. I believe that Prof. Belcher's generousness and patience is a key element to enable the lab members to closely collaborate with each other - I can say that she is a natural-born advisor. I have no doubt that many conversations we had were the invaluable intellectual asset that will deeply affect my thought on designing, performing, and publicizing scientific research in the future. Her passion to education as well as research is not very common for such a famous scientist, and it was delightful to see how many students (from high school students to her graduate advisee like myself) are motivated for scientific research from her talks and demonstration. Being a student in the Belcher group is an experience that I will miss in my whole life.

I am also deeply thankful to my thesis committee members: Prof. Paula T. Hammond (MIT Chemical Engineering) and Prof. Scott Manalis (MIT Media Lab and Biological Engineering). I was indebted to them for their extensive support for the past three years. Prof. David A. Weitz (Harvard University) allowed me to work in his laboratory and also shared his time to carefully read and edit my manuscript for publication. The idea on the incorporation of genetically engineered viruses into microgels was initiated from the personal conversation between Dr. Jin-Woong Kim and myself in early 2007. At that time Dr. Kim was a postdoc in the Weitz's group. Since he left for a job at the Amore Pacific Corp. R&D Center in Korea, Dr. Daeyeon Lee (now a professor in the University of Pennsylvania) devoted enormous efforts to this project with his generous understanding my situation. Dr. Lee carefully studied the fabrication conditions to consistently produce the similar microgel samples. Late night after the experiments we often went out to grab a beer. Tasting fresh air and beers while sitting next to the street at night is a really good memory for this collaboration. Prof. Keith Nelson (MIT Chemistry) allowed me to collaborate with

Mr. Taeho Shin to obtain the time-resolved absorption spectra of the porphyrin nanoantennae. Mr. Shin kindly spent his time to set up pump-probe spectroscopy system for my work. I will miss my small talks with him in front of Building 4.

I thank Prof. Douglas A. Lauffenburger for his very considerate support for me and his tremendous service for building such a wonderful academic community - MIT BE! I am proud of being a part of it. I have also been fortunate to be surrounded by many great advisors, mentors, and friends in BE. I particularly want to thank the following people: Prof. Pete Dedon, Prof. Ram Sasisekharan, Prof. Kimberly Hamad-Schifferli, Prof. Peter So, Prof. Jongyoon Han, Prof. Alan P. Jasanoff, Prof. Alan J. Grodzinsky, Ms. Dalia Fares, Dr. Nate Tedford, and Dr. Pete Wishnok for their support and advices. I also want to express my special appreciation of the guidance and advice I received from my first BE advisor, Prof. Bevin P. Engelward, who spent much time to kindly teach me DNA damage and repair from scratch. Although I could not complete my work in the Engelward group, I deeply appreciate her help and admire her scientific efforts. Dr. Natalie Kuldell was also a very special advisor to me. I was assigned to TA her 20.109 class, and it was undoubtedly the best one I have ever seen. Her efforts to develop the class were enormous, and I learned so many things from her.

Dr. Andrew P. Magyar is my closest collaborator. Throughout my thesis work we worked very closely on almost every aspect of the study. His creative perspectives, fresh ideas, open attitude and enormous support are deeply appreciated. I always told him like: "Hey, Andrew. This instrument doesn't work. Do you have any idea? - I mean, can you fix it?", "Hi, Andrew. Can you make this for me?", or "Andrew, I have no idea about what this guy is talking about. Do you have time to read this paper? (And let me know what it is.)". Then, he has been always ready to help. He was a Triplet A of my research - though he always did it for free! I believe he will make a great advisor and teacher and researcher - I can imagine how many students will be encouraged and inspired from him. Maybe, in the future, if I make an academic advisor and have a student whom I can't deal with, then I may ask him "Hey, Andrew. Can you teach this guy for me?" I hope what I just said doesn't scare him. Or, he might say "Yoon Sung, I'm now a Ph.D. You should pay." - "Thanks, Andrew. I will. Eagerly." My life in the Belcher group was a way much more enjoyable thanks to him.

Heechul is a hidden player of my thesis work. He has been involved in many parts of the study, and I appreciate his assistance. Mr. Thomas "Scott" Pollom, Jr., and Katherine Choi worked with me as a UROP student. Both of them joined me during their freshman year. I really enjoyed working with them. They edited almost all of my writing, and I deeply appreciate what I have learned from them. I also thank many labmates: Mr. Vesal Dini for his lab management and humanism (or his humanistic lab management), Ms. Michelle Barron and Mr. Jared Embelton for their administrative assistance, Mr. Roberto "Robbie" Barbero, Dr. Chung-Yi Chiang and Ms. Hyunjung Yi for their warm neighborhood, Dr. Rebekah Miller for her critical comments on my work, Mr. Forrest W. Liau for his help and trust on many different things, and Dr. Yun Jung Lee, Dr. Debadyuti "Rana" Ghosh, Dr. Mark Allen, Dr. Georg Fantner, Dr. Brian Neltner, Ms. Shanying Cui, Dr. Kisuk

Kang, Dr. Sreekar Bhaviripudi, Dr. Dong Soo Yun, Dr. Jifa Qi, Dr. Nicholas "Nick" Orf, Dr. Jennifer Hsieh, Dr. Paul Widboom, Mr. Fred "John" Burpo, Mr. Xiangnan Dang, Mr. David S. Gray, Mr. Gaelen T. Hess, Mr. Aditya Kohli, Ms. Rebecca Lynn Ladewski, Ms. Youjin Lee, Ms. Julie E. Norville, Ms. Dahyun Oh, Ms. Elizabeth Wood, Dr. Eric Krauland, Dr. Ahmad "Mo" Khalil, Dr. Steve Kottman for their affirmative interactions with me during my stay in the Belcher group.

I also have greatly benefited from my interactions with my old friend, Dr. Haeshin Lee, during his stay at MIT as a postdoc in the Langer group. We share a history of hard times, which cannot be replaced with any other things. I am very proud of being his friend who went through all such obstacles and made such a wonderful academic advisor at KAIST. I thank Dr. Jung Ah Lee, Dr. Byeong-Su Kim, Dr. Seung Woo Lee, Dr. Avni Argun, and Dr. Nathan Ashcraft in the Hammond group for all of the discussion and collaborations. I thank Dr. Sangjin Ryu, Dr. Jongnam Park, Dr. Daekeun Hwang, Dr. Hyuk Sang Kwon, Dr. Werner Olipitz, Dr. Dominika Wiktor-Brown, Mr. James T. Mutamba, Mr. David M. Weingeist, Mr. Anderson Shum, Dr. Daekeun Kim, Dr. Changsik Song, Dr. Moon-Ho Ham, Mr. Wonjoon Choi, Dr. Byeong Sun Kong, Ms. Anne Gorham, Mr. Yong Zhang, Mr. Patrick Boisvert, Ms. Elisabeth L. Shaw, Mr. Tim McClure, Dr. Scott A. Speakman, Ms. Deborah Pheasant for their help.

I also thank my previous advisors and mentors: Prof. Tae Gwan Park for his enormous influence on my career. My academic life started with him, and a lot of his advices have helped me during my study at MIT. I thank Prof. Byung-Gee Kim, my undergraduate advisor, for his strong support. I always learn a lot through my conversation with Prof. Kim, who carefully listens to my thoughts on many different issues. I thank Prof. Kookheon Char, Dr. Ih-Seop Chang and Dr. Sang Hoon Han for their extensive support and valuable advices.

Finally, and most importantly, all of my thanks go to my family. My lovely wife, Jihyun Kim, has supported me for the past six years. I have felt sorry about a lot of things she gave up for my study at MIT. Without her tremendous love and trust I would have not made such a progress in my academic career. I want to give my very special thanks to her with all my love. My mother, Jae Hee Choi, is the person who has given me her inexhaustible support for my whole life. Whenever depressed, I am reminded of what she had suffered for me. That has been the origin of my strength, and will be. My father, Jung Sik Nam, gave me a warm heart. His grandson, Hoyoung, seems to get it from him. It is my great pleasure to see them smile to each other. I thank my father for his encouragement. My son, Elliot Hoyoung Nam, is such a lovely boy who filled my life at MIT with enormous joy. "Thanks for being my little one, honey. I love you so much!"

I acknowledge that my thesis work was supported from Eni, S.p.A. (Italy) through the MIT Energy Initiative Program.

"Thank you!"

Contents

List of Figures

List of Tables

Chapter 1

Introduction

1.1 Solar Energy Storage

Environmental pollution and limited sources of fossil fuels are forcing our society to seeking alternative, renewable sources of energy. Sunlight is one of the most abundant resources on earth, providing is 3 x 10^{24} joules a year, which is 10^4 times the amount needed to supply the total global energy consumption: *i.e.*, only 0.1 % coverage of the Earth's surface is required to fulfill the energy consumption if a solar cell with an efficiency of 10 % is used. Undoubtedly, solar energy provides an unparallel promise to generate enormous amounts of clean energy with less concern for global warming. However, the use of solar energy has several intrinsic drawbacks, including the low power density (about 1 kW m^{-2} in average), the intermittency, and heterogeneous global distribution. In addition, energy demand is highly fluctuating with time, resulting in a serious mismatch between the supply of solar energy and the energy demand. In order to overcome these limiting factors of solar energy, scientists have paid increasing attention on the conversion of solar energy into chemical fuels that can be transported to the places of demand and be stored for a long period of time [18].

The solar energy conversion into chemical fuels can be performed in two different ways: thermal processes and photonic processes. In solar thermal systems the photon energy is first converted to heat, which can be stored in a medium or converted to mechanical electrical energy. Currently, the heat storage is more efficient and much cheaper than storage of electricity. Solar thermal energy conversion processes can be divided to (i) 'low to medium' temperature applications and (ii) high temperature applications. The former is based on a flat plate collector and high temperature applications, while in the latter system solar radiation is concentrated using a technique called 'concentrated solar power' based on parabolic mirrors or lenses. A low temperature system is used for domestic water heating systems, but the storage density and time are very limited. A high temperature system is used for the light-driven production of steam in a parabolic trough power plant. The advantage of the high temperature system is that the heat storage efficiency and the energy conversion efficiency of heat engines increase with increasing the temperature of the heat source. It also reduces the size of collectors and the land use, minimizing the environmental effects of a power plant.

Another approach for solar energy storage, relevant to this thesis, is to directly convert photon energy into clean chemical fuels, such as hydrogen and oxygen, as it is found to be done in natural photosynthesis [107, 8, 38, 41, 9]. Storing solar energy by mimicking photosynthesis has been pursued since the early 1970s; however, the approaches have been primarily limited to the extraction and reconstitution of the existing natural pigments, photosystems, and photosynthetic organisms. Chemists and materials scientists have also found that a variety of synthetic organic and inorganic molecules can mediate redox reactions, which can photochemically or electrochemically generate clean fuels, oxygen and hydrogen. In 1972, Akira Fujishima and Kenichi Honda of the University of Tokyo, Japan, reported the first experimental demonstration of the evolution of hydrogen and oxygen through the photoelectrochemical water

splitting using n-type TiO_2 [1] illuminated with near UV light [33]. Anodic current began to flow for wavelengths shorter than 415 nm, which corresponds to the band gap energy of TiO_2 (about 3.0 eV). The photocurrent also increased with the increased light intensity (Figure 1-1a). In their system, a semiconducting photocatalyst uses a photon to generate electron-hole pairs. At the junction between a pair of different materials, the effect can set up an electric potential difference across the interface and two redox reactions can occur. One is the water oxidation in which the hole in the valence band can be filled with an electron produced by the oxygen generation at the anode. The other is the water reduction in which the excited electron is consumed at the cathode (*e.g.*, a platinum black electrode) (Figure 1-1b). Fujishima and Honda demonstrated that oxygen evolution occurred at - 0.5 eV *vs.* SCE in a 0.1 N Na_2SO_4 electrolyte solution at pH 4.7, which was more negative than the standard potential (0.7 eV[2] *vs.* SCE for the reversible oxidation of water to oxygen at the same pH) [32]. This result indicates that the water oxidation potential negatively shifted by about 1.2 eV. This shift was driven by the absorption of the photon energy by the semiconducting anode. It is now very well established that a potential difference of more than 1.23 eV is necessary between anode and cathode for photoelectrochemical water splitting, as summarized below.

$$H_2O \rightarrow H_2 + 1/2\ O_2,\ E = 1.23\ eV$$

$$2H_2O + e^- \rightarrow H_2 + 2OH^-,\ E_o\ (pH\ 7) = -\ 0.41\ eV\ vs.\ NHE$$

$$2H_2O \rightarrow O_2 + 4H^+ + 4e^-,\ E_o\ (pH\ 7) = +\ 0.82\ eV\ vs.\ NHE$$

[1] They used a single crystal wafer of n-type rutile TiO_2 after treatment at 700°C at $10^{-4} \sim 10^{-5}$ torr for about 4 h to increase the conductivity of the crystal. The wafer was about 1.5 mm thick and the exposed (001) surface area was about 1.0 cm^2.

[2] 1 eV = 1.602 x 10^{-19} J

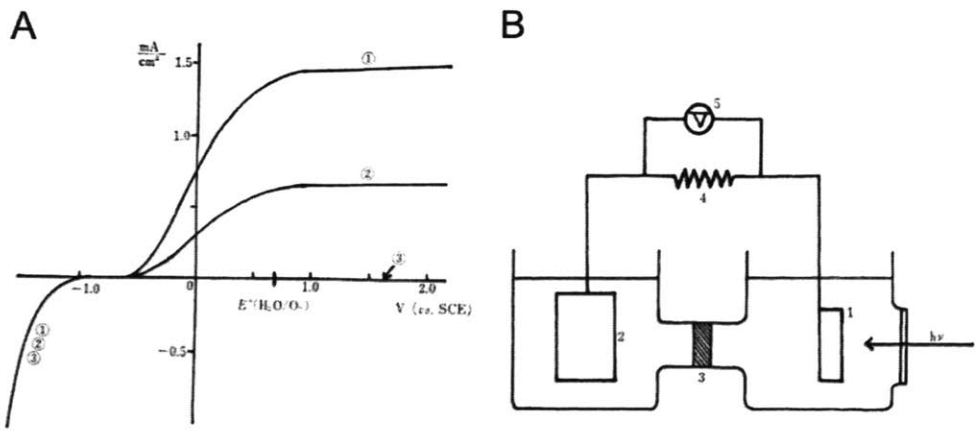

Figure 1-1: **Photoelectrochemical water splitting system using a titanium oxide anode (Fujishima and Honda, 1972). A**, Current-voltage curves for TiO_2 n-type semiconductor with and without illumination at pH 4.7: (1) under irradiation (relative light intensity, 100%); (2) under irradiation (relative light intensity, 50%; and (3) without irradiation. **B**, An electrochemical cell with TiO_2 electrode under irradiation: (1) TiO_2 electrode; (2) Pt electrode; (3) sinter-glass diaphragm; (4) an outer load; and (5) a voltameter. The images were adapted from [32] and [33].

1.2 Photocatalytic Water Splitting

Fujishima and Honda demonstrated that a TiO_2 electrode can decompose water under illumination by photons of energy greater than the band gap of the semiconducting electrode. However, the potential difference required for water splitting is only about 1.23 eV, which corresponds to the energy of the wavelength of about 1,008 nm. Thus, it is theoretically possible that the light having a relatively shorter wavelength can decompose water. This idea has brought extensive research on visible light-driven water cleavage for the past nearly 40 years, though little commercially attractive technology has been yet developed in terms of the efficiency and stability.

In 1976, Tetsuo Osa and Masamichi Fujihira of Tohoku University, Japan, reported a photoelectrochemical cell based on an optically transparent semiconducting electrode chemically modified with sensitizing pigments [103]. This approach is a very early version of dye-sensitized systems for water splitting systems driven by visible

light, where the arrays of organic pigment molecules absorb the light. Rhodamine B was chemically attached as a sensitizer onto the surface of SnO_2 and TiO_2 electrodes using two different linkages: a amide bond with γ-aminopropyltriethoxysilane as a linker and an ester bond by directly coupling a carboxylic acid group of rhodamine B with a surface hydroxyl group of the metal oxide electrode [31]. It was found that the sensitized photocurrent was about two orders of magnitude greater on the ester-linked electrode than the photocurrent observed on the amid-linked electrode (Figure 1-2). It was speculated that the difference in distance of the conjugated π electronic system of rhodamine B from the electrode surface accounts for such difference in efficiency of the electron injection from excited pigments to the conduction band of semiconductor electrodes. In the amide-linked electrode, the insulating alkyl chains seemed to intervene as an energy barrier inhibiting the electron injection.

In 1978, John Kiwi and Michael Grätzel of Ecole Polytechnique Federale Lausanne, Switzerland, reported a redox catalytic system for oxygen evolution [64, 66]. First, photochemical oxygen evolution was demonstrated using platinum oxide, PtO_2 (Adams catalyst), as a redox catalyst coupled with a reversible electron shuffling molecule, cerium(IV) sulfate, in aqueous H_2SO_4 where Ce^{4+} is relatively stable. The redox potential of Ce^{4+} is about 1.44 eV and thus thermodynamically water oxidation is a spontaneous reaction in the presence of Ce^{4+}. The reduction of Ce^{4+} to Ce^{3+} was spectroscopically observed and correlated with the oxygen evolution. It was also shown that oxygen evolution through the reduction of tris(2,2'-bipyridine)ruthenium(II), $Ru(bpy)_3^{3+}$, by water can be promoted by redox catalysts, PtO_2 or iridium oxide (IrO_2). The approach was extended to a system of two coupled colloidal redox catalysts enabling simultaneous evolution of oxygen and hydrogen through photochemical water splitting [58]. The experiments were performed with dimethylviologen (N,N'-dimethylbipyridine dication, MV^{2+}) and $Ru(bpy)_3^{2+}$. Photon-excited $Ru(bpy)_3^{2+}$ reduced MV^{2+} in a diffusion-controlled process and then the prod-

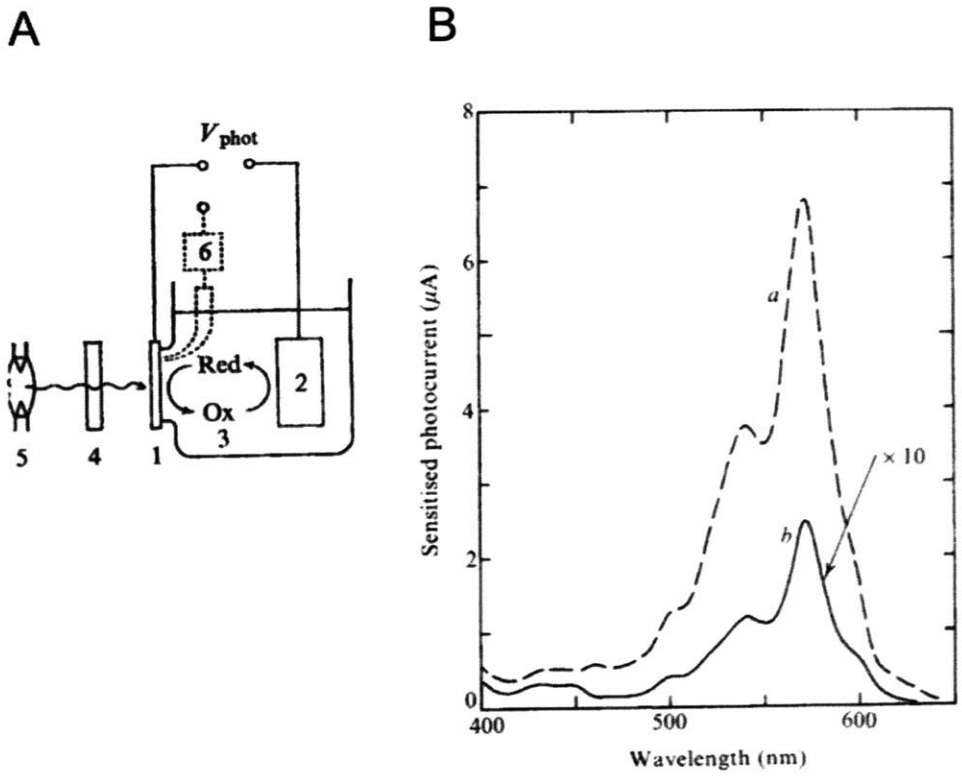

Figure 1-2: **Photocell system using covalently-bound pigments on semiconductor surfaes (Osa and Fujihira, 1976). A**, an electrochemical photocell consisting of a transparent semiconducting anode chemically modified with rhodamine B (1) and a Pt electrode (2) in contact with an electrolyte containing a redox system (3). A 500-W xenon lamp (5) was used as a light source with optical filters and/or a monochromator (4). **B**, Spectral dependence of the photocurrent at the chemically modified SnO_2 electrodes with rhodamine B. The anode was polarized at + 0.4 eV against a SCE and illuminated through the electrode: (a) photocurrent spectrum sensitized by a sub-monolayer of ester-linked rhodamine B in contact with a Britton-Robinson buffer (pH 3.9) containing 10 mM hydroquinone as a supersensitizer and (b) photocurrent spectrum sensitized by the amide-linked rhodamine B in contact with 0.2 M Na_2SO_4 containing 5 mM hydroquinone, which is magnified 10 times for comparison. The images were adapted from [103] and [31].

ucts, $Ru(bpy)_3^{3+}$ and reduced MV^+, are thermodynamically able to produce oxygen and hydrogen from water. Colloidal ruthenium oxide (RuO_2) catalysts were used to facilitate these processes because the back reaction can occur with a rate constant of $k = 2.4 \times 10^9\ M^{-1}\ s^{-1}$ and Pt sol was employed to reoxidize MV^+ in microseconds and reduce water to produce hydrogen.

In 1997, Masayuki Yagi and his colleagues of Niigata University, Japan, reported a photoelectrochemical system based on a multilayered indium tin oxide (ITO) anode consisting of a Nafion membrane incorporating $Ru(bpy)_3^{2+}$ and an electrodeposited Pt black adsorbing trinuclear ruthenium complex (Ru-red) ($[(NH_3Ru(\mu\text{-}O)Ru(NH_3)_4(\mu\text{-}O)Ru(NH_3)_5]^{6+}$ as a water oxidation catalyst (Figure 1-3, top) [124]. This interesting anode design can be thought of as a combination of the Osa and Fujihira's system [103] for a dye-sensitized electrode and the Grätzel's colloidal water oxidation system [64]. The multilayered photocatalytic electrode showed visible light-driven oxygen evolution and photocurrent, though both the turnover numbers of $Ru(bpy)_3^{2+}$ and Ru-red were very low, indicating the low catalytic efficiency of the system (Figure 1-3, bottom). This low catalytic performance might be related to the lack of any structural consideration of the assembly of multiple materials at the nanoscale level. This study implies that more sophisticated structural design is very important for the exciton migration among $Ru(bpy)_3^{2+}$ incorporated in the Nafion layer and the charge transfer between the photosensitizer layer and the catalyst layer. In particular, the Nafion membrane was too thick (about 1 μm) and thus it seems impossible that individual $Ru(bpy)_3^{2+}$ molecules are interconnected throughout the whole layer. In the reported experimental conditions, only a small portion of $Ru(bpy)_3^{2+}$, Ru-Red, and ITO may maintain a good contact of each other for the photocatalytic water oxidation.

In 1998, Oscar Khaselev and John A. Turner of the National Renewable Energy Laboratory (Golden, CO, USA) reported a new design of a photoelectrochemical cell

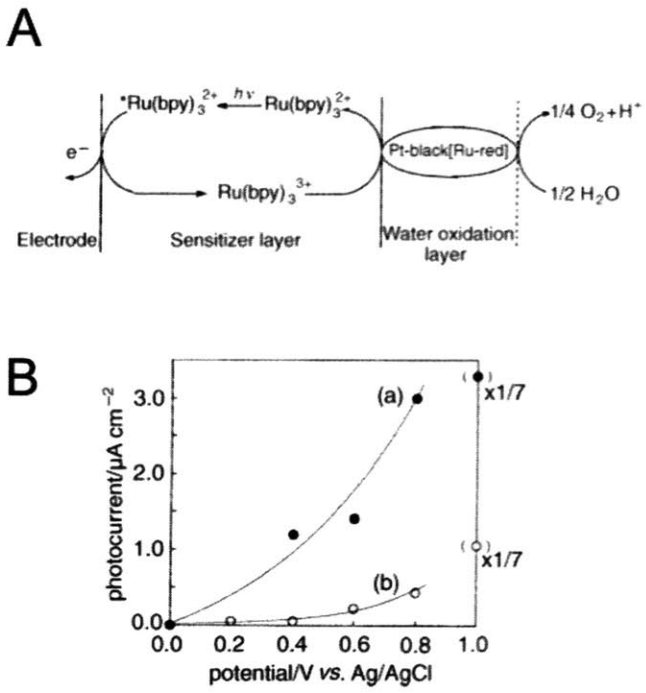

Figure 1-3: **Visible light-driven water splitting system using a multilayered photoanode (Masayuki Yagi and his colleagues, 1997). A**, mechanism of photoinduced oxygen generation in the ITO/Nafion[$Ru(bpy)_3^{2+}$]/Pt-black[Ru-red] system. **B**, relationship between photocurrent and applied potentials using an (a) ITO/Nafion[$Ru(bpy)_3^{2+}$]/Pt-black[Ru-red] and (b) ITO/Nafion[$Ru(bpy)_3^{2+}$] [124].

integrated with a photovoltaic device [62]. The device was a solid-state tandem cell composed of a GaAs bottom cell connected to a $GaInP_2$ top cell through a tunnel diode interconnected (Figure 1-4). The top p/n $GaInP_2$ junction was designed to have a band gap of 1.83 eV to absorb the visible light and the bottom p/n GaAs junction to have a band gap of 1.42 eV to absorb the near-infrared light. The hydrogen evolution efficiency of the system was 12.4 %, which was calculated from the short-circuit current and the lower heating value of hydrogen. The theoretical limit solar-to-electrical efficiency was about 34 % for the combination of band gaps used for the study. The cathodic reaction was used to drive full water splitting reactions because water reduction has the lowest overpotential losses and semiconductors have a better chemical stability at the cathode. The current limitation of this approach seems to be a low chemical stability of the semiconductors in the electrolytes used for their study (3.0 M H_2SO_4)[3]. Further studies are being actively performed in the same group that utilize both of the anodic and cathodic photocatalytic reactions.

In 2002, Shahed Khan and his colleagues reported a visible light-driven water splitting by a chemically modified TiO_2 [61]. A Ti metal sheet was thermally pyrolyzed in the presence of combustion products in a natural gas flame with controlled amounts of oxygen added. The flame-made TiO_2 shows threshold wavelengths of 535 nm (2.32 eV) and 440 nm (2.82 eV) while oven-made reference TiO_2 has a threshold wavelength of 414 nm (3.0 eV). Photocurrent densities from the water splitting by the chemically modified TiO_2 was 3.60 mA cm^{-2} under illumination of light of 40 mW cm^{-2} at an applied potential of 0.30 V, which corresponded to the maximum photoconversion efficiency ϵ_{eff} of 8.35 %, though there has been disagreement about the efficiency [4]

[3]To my knowledge, the systems worked only for 20 minutes for their published results. Currently it seems to last for about an hour. This information originates from my personal communication with a researcher in the NREL and the numbers may be not so precise

[4]The photoconversion efficiency ϵ_{eff} (photo) of light energy to chemical energy in the presence of an external applied potential E_{app} was expressed as $\epsilon_{eff}(photo) = [j_p \frac{E^o_{rev} - |E_{app}|}{I_o} \times 100]$, where j_p is the photocurrent density (mA cm^{-2}), E^0_{rev} is the standard state-reversible potential (which

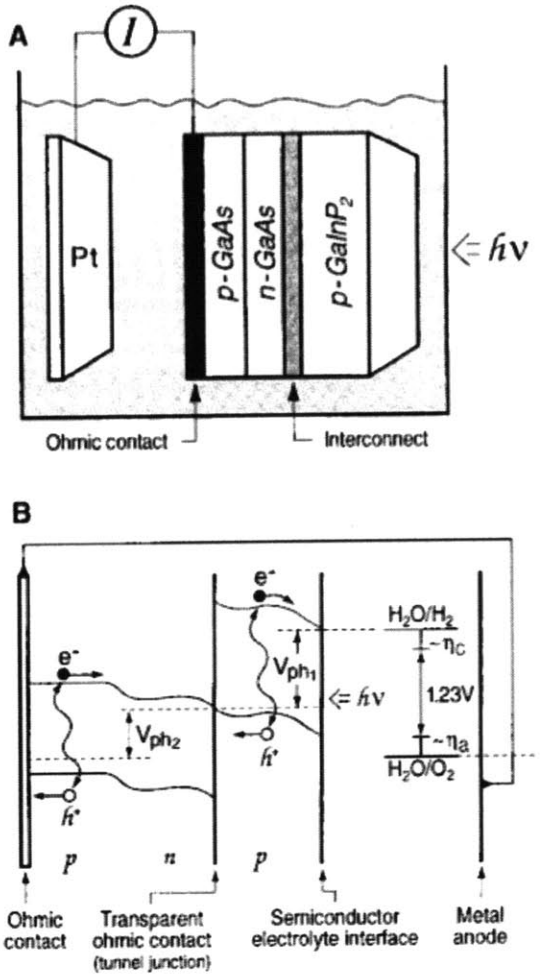

Figure 1-4: **Monolithic photoelectrochemical-photovoltaic device (Khaselev and Turner, 1998). A**, Schematic of the monolithic PEC/PV device. **B**, idealized energy level diagram for the monolithic PEC/PV photoeletrolysis device [62].

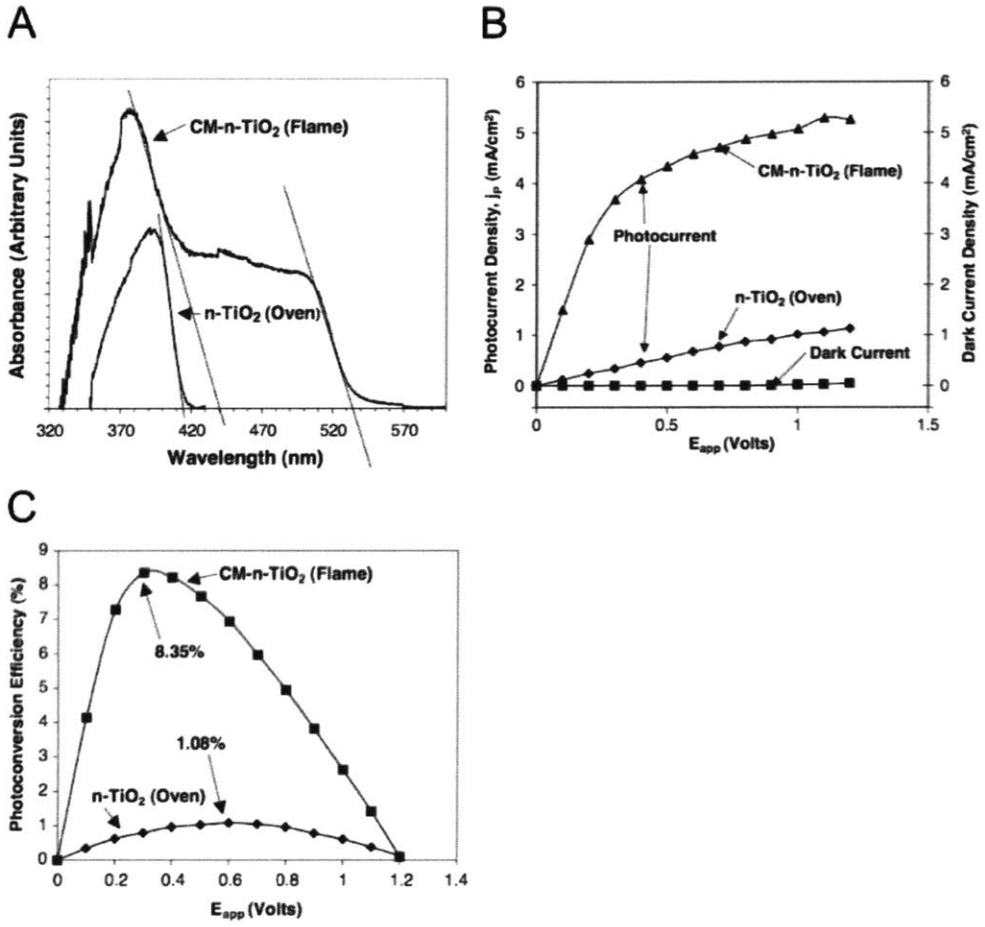

Figure 1-5: **Photocatalytic water splitting by a chemically modified titanium dioxide (Khan et al., 2002).** **A**, The absorption spectra of chemically modified TiO_2 (CM-n-TiO_2, flame-made) and reference n-TiO_2 (electric tube furnace- or oven-made). The flame-made sample shows threshold wavelengths of 535 nm (band gap of 2.32 eV) and 440 nm (band gap of 2.82 eV), while the electric tube furnace- or oven-made sample shows a threshold wavelength of 414 nm (band gap of 3.0 eV). **B**, Photocurrent density as a function of applied potential at the photoelectrodes under xenon lamp illumination at an intensity of 40 mW cm^{-2}. **C**, Photoconversion efficiency as a function of applied potential under the same condition [61].

In 2005, Craig Grimes and his colleagues of the Pennsylvania State University reported the photocatalytic water splitting using TiO_2 nanotubes grown from a titanium sheet (Figure 1-6) [91]. Their nanotube arrays were prepared via potentiostatic anodization in an electrolyte of 0.5 % HF mixed with acetic acid at 7:1 using a Pt counter electrode. The anodized nanotubes were annealed at 500°C in an oxygen ambient for 6 h. Under 50 W metal hydride lamp illumination (320 $\sim$ 400 nm, about 100 mW cm^{-2}) in 1 M KOH, the photoconversion efficiency was about 6.8 % at maximum. To examine the effect of the morphology of the titania nanotube arrays on the photocurrent efficiency, the nanotube arrays were prepared via anodization at 10 V at four different electrolyte bath temperatures: 5, 25, 35, and 50°C. The pore diameter was about 22 nm for all of the prepared samples, while the wall thickness increased with decreasing processing temperature from 9 nm at 50°C to 34 nm at 5°C. Interestingly, the photocurrent increased with decreasing the processing temperature: the photocurrent density of the 5°C arrays was approximately three times that of the sample prepared at 50°C at 1.5 V of the applied potential. It was speculated that the thicker walls of the nanotubes increased the band bending potential, which decreased the charge carrier recombination which in turn increased the photocurrent. Their explanation brought up an interesting issue on the impact of nanostructures on the performances of photoelectrochemical systems: a large contact area at the semiconductor-electrolyte interface and light scattering within a porous structure can be advantageous for photocatalytic reactions, while the electronic structures or charge mobility can negatively affected by nanostructures. Balancing these positive and negative effects seems to be critically important consideration for optimization

---

is 1.23 eV for the water-splitting reaction), I_0 is the intensity (power density) of the incident light (mW cm^{-2}), and E_{app} is the applied potential, which is obtained as $E_{app} = (E_{meas} - E_{aoc})$, where E_{meas} is the electrode potential at which j_p was measured, and E_{aoc} is the electrode potential at open circuit in the same electrolyte solution and under the same illumination of light at which j_p was measured. For the chemically modified TiO_2 electrode, E_{aoc} = -1.0 V vs. SCE was observed at illumination intensity of 40 mW cm^{-2} in 5 M KOH solution; E_{meas} and E_{aoc} were with respect to the same reference electrode (SCE).

of nanostructures.

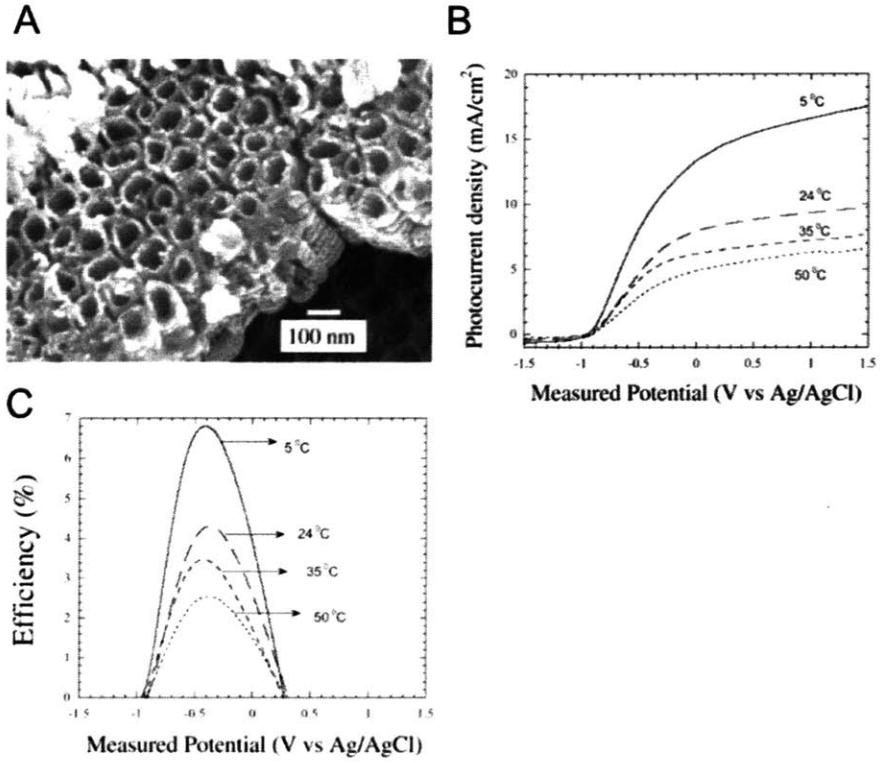

Figure 1-6: **Photocatalytic water splitting by an anodized titanium oxide nanotube arrays (Mor et al., 2005).** **A**, Cross-sectional field emission scanning electron micrograph of 10 V TiO_2 nanotube arrays anodized at 25°C. **B**, Photocurrent density vs. measured potential for 10 V TiO_2 nanotube arrays anodized at different bath temperatures: 5, 15, 35, and 50°C. **C**, Photoconversion efficiency as a function of measured potential for 10 V TiO_2 nanotube arrays anodized at different bath temperatures: 5, 15, 35, and 50°C [91].

In 2006, Allen J. Bard and his colleagues of the University of Texas at Austin reported the use of vertically grown carbon-doped TiO_2 nanotube arrays with high aspect ratios for visible light-driven water splitting. TiO_2 nanotube arrays with 3.3 μm in length were grown from a 0.25 mm-thick Ti substrate via anodization in 1 M $(NH_4)H_2PO_4$ containing 0.5 wt% NH_4F at an applied voltage of 15 V with a Pt counter electrode. It was found that the TiO_2 morphology is an important parameter for water oxidation catalysis: the photocurrent depends on the aspect ratio of the

TiO_2 nanotube. The array of TiO_2 nanotubes with 3.3 μm in length produced a photocurrent more than 10 times that of a 15 μm-thick TiO_2 nanoparticle (Degussa P25) film in 1 M KOH under about 100 mW cm^{-2} of xenon lamp irradiation. It was speculated that an increased light penetration depth and better scattering within a regular pore structure contribute to the increased anodic photocurrent via water splitting. The carbon dopant was introduced into the TiO_2 nanotube arrays, resulting in $TiO_{2-x}C_x$, by annealing at 600°C under a controlled CO gas flow. This doping process replaced oxygen with nitrogen or carbon, producing a mixed $2p$ state. The calculated band gap energy of the $TiO_{2-x}C_x$ nanotube array was 2.22 eV as determined by extrapolation of the photocurrent vs. the absorption coefficient. Accordingly, the $TiO_{2-x}C_x$ nanotube array showed a visible light-driven water oxidation activity with the open circuit of approximately - 0.4 eV vs. Ag/AgCl, or - 0.2 eV vs. NHE, which was about 0.2 eV more positive compared to the undoped TiO_2 under unfiltered Xe lamp radiation. To the TiO_2 nanotube array, O Ok Park and his colleagues of Korea Advanced Institute of Science and Technology (KAIST) introduced tungsten trioxide (WO_3) as a coating layer. Prior to their work, nanostructured WO_3 films have been shown to have photocatalytic activity for water oxidation in 1 M $HClO_4$ with an open circuit voltage of 0.45 V vs. RHE. In addition to its good stability against corrosion in an aqueous solution, WO_3 has a band gap of about 2.5 eV, enabling the use of visible light. A WO_3-coated TiO_2 nanotube array was prepared by electrochemical deposition of $WO_{3-x}{\cdot}H_2O$ sol to TiO_2 nanotube array. When illuminated by a xenon lamp (150 mW cm^{-2}) in 1 M $HClO_4$, The WO_3-coated TiO_2 nanotube array exhibited a maximum conversion efficiency of 0.87 %.

Another approach for visible light-driven water splitting on anodized nanotube arrays was introduced by Craig A. Grimes and his colleagues in 2007 [90]. Vertically oriented Ti-Fe-O nanotube arrays with the iron content from 69 % to 3.5 % were prepared by anodizing Ti-Fe metal films sputtered onto FTO glass in a mixture of

ethylene glycol and NH_4F. The photoelectrochemical properties of the prepared Ti-Fe-O nanotube arrays were examined using 1.0 M NaOH as an electrolyte with platinum foil as a counter electrode and saturated Ag/AgCl as a reference electrode. A 300 W xenon lamp (100 mW cm^{-2}) was used as a light source with AM 1.5 filter. The highest photocurrent of Ti-Fe-O was about 2.0 mA cm^{-2} at 0.65 V *vs.* Ag/AgCl, below which the dark current for water oxidation was negligible. This photocurrent was much better than a pure nanoporous α-Fe_2O_3 film (1.5 μm in thickness) on FTO glass, which had a maximum photocurrent of 20 - 25 μA cm^{-2} at 0.4 V. What was interesting in their works was that the maximum photocurrent was obtained from a Ti-Fe-O sample containing 6.6 % Fe while the lowest photocurrent from a sample containing 3.5 % Fe. Above 6.6 %, the mixed results of photocurrents were shown. They speculated that minimal levels of Fe^{3+} ions act as trap sites, while significant amounts of Fe^{3+} ions increase the recombination rate of the photogenerated electron-hole pairs.

To reduce the recombination, several nanostructures have been reported and evaluated for photocatalytic water splitting. In 2007, Xie Quan and his colleagues reported TiO_2-multi-walled carbon nanotube (MWNT) heterojunction arrays on a Ti substrate as an electrode (Figure 1-7A-C) [127]. The formation of heterojunction between TiO_2 and MWNTs was demonstrated from a rectifying behavior in the current-voltage curve, while MWNTs and the Ti substrate formed an ohmic contact (Figure 1-7D). Photoelectrochemical properties of the system were investigated using 10 mM Na_2SO_4 as an electrolyte and a 300 W high pressure mercury lamp as a light source (a main wavelength of 365 nm and the UV intensity of 0.75 mW cm^{-2}). It was shown that MWNTs effectively increased the photocurrent density and reached its maximum with a small positive bias potential. In contrast, the photocurrent of TiO_2/Ti increased with increasing the bias potential because TiO_2 is a simple semicondutor and the current depends on only the external electric field (Figure 1-7E). Prashant

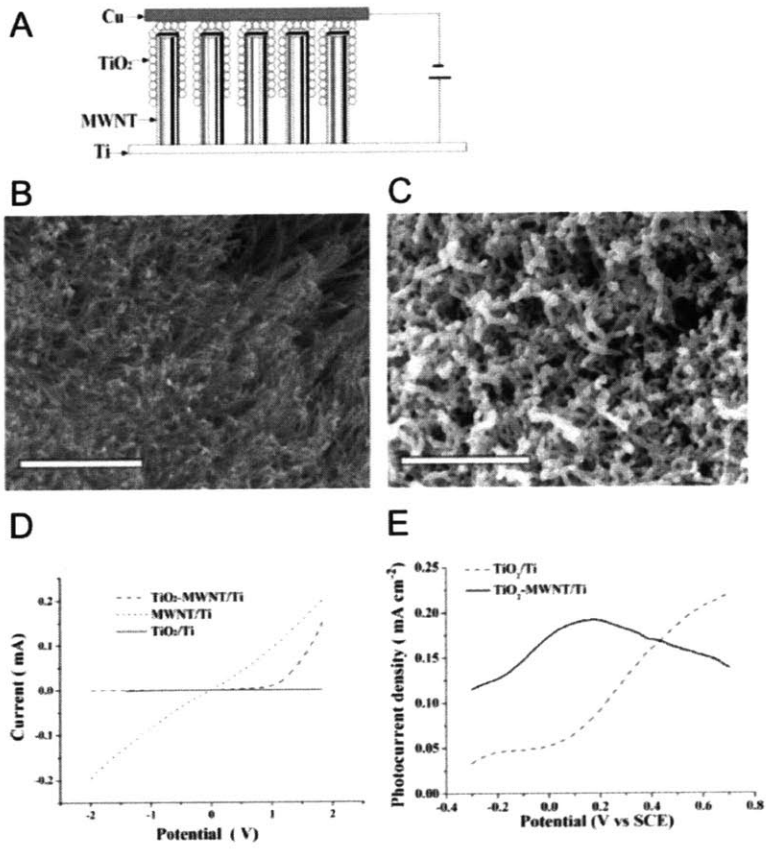

Figure 1-7: **Titanium dioxide-multiwalled carbon nanotube heterojunction arrays for efficient charge separation (Yu et al., 2007).** **A**, Schematic of the TiO_2-MWNT structure. **B and C**, Scanning electron micrographs of the MWNT array (B) and TiO_2-MWNT array (C) (scale bar = 5 μm). **D**, Current-voltage characteristic of the MWNT/Ti, TiO_2-MWNT/Ti, and TiO_2/Ti. **E**, Photocurrent density *vs.* applied potential for TiO_2-MWNT/Ti and TiO_2/Ti in 10 mM Na_2SO_4 with UV light of 0.75 mW cm^{-2}.

V. Kamat and his colleagues also reported the application of single-wall carbon nanotube (SWNT) substrates with TiO_2 nanoparticles (Degussa P-25) to photocatalytic water splitting [69]. It was found that the photocurrent of SWNT-TiO_2 was significantly higher that that of TiO_2 presumably because the electron accepting ability of semiconducting SWNTs facilitated the charge transfer from TiO_2 to the electrode through SWNTs. The flat band potentials were - 0.86 V vs. SCE for TiO_2 and - 0.79 V for SWNT-TiO_2. This shift of about 70 mV was interpreted as charge equilibration between TiO_2 and SWNTs, though the band energies of SWNTs used were assumed rather than experimentally shown. Similar core-shell structures having TiO_2 as a shell material was suggested by Denwei Wang and his colleagues. Highly conductive, two-dimensional $TiSi_2$ nanonets were coated with a layer of crystalline TiO_2 by an atomic layer deposition technique, resulting in $TiO_2/TiSi_2$ heterostructures. The photoelectrochemical properties were examined in 50 mM KOH or HCl under illuminations of a 150 W xenon lamp. To utilize visible light, tungsten was incorporated to TiO_2 at a ratio of 3:7, which reduced the optical band gap from 3.2 to 2.0 eV.

In 2009, Thomas E. Mallouk and his colleagues reported a photoelectrochemical water splitting system based on dye-sensitized water oxidation catalysts [126]. A new heteroleptic ruthenium dye was designed as a molecular linker to connect hydrated iridium oxide (IrO_2) nanoparticles to a porous TiO_2 electrode. Basically, three bipyrine ligands were used with chemical modification of side chains: phosphonates for TiO_2 and malonates for IrO_2. Photoelectrochemical performances were evaluated in a solution of 30 mM Na_2SiF_6 buffered to pH 5.75 with $NaHCO_3$ and 500 mM Na_2SO_4. With visible light (> 410 nm) a photocurrent was detected above - 325 mV *vs.* Ag/AgCl. A current density of 12.7 μA cm^{-2} was obtained with a 450 nm light source at 7.77 mW cm^{-2}, which corresponds to 4.5 x 10^{-3} external quantum efficiency, or 0.9 % internal quantum efficiency. However, under steady illumination, the current decayed over a period of about 4 h because of the chemical decomposition of the ruthenium

complex dyes.

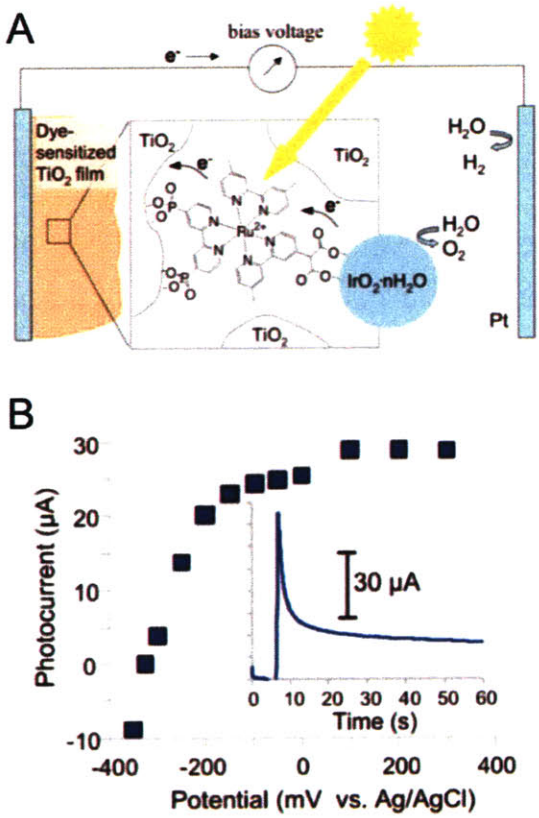

Figure 1-8: **Photoelectrochemical water splitting system based on visible light-absorbing dyes (Youngblood et al., 2009).** **A**, Schematic of the water splitting dye sensitized solar cell. **B**, Steady-state photocurrent *vs.* applied potential in a three electrode system. Insert indicates a chronoamperometric profile recorded at 0 V *vs.* Ag/AgCl/saturated NaCl.

1.3 Natural Photosynthesis and Biomimetic Approaches

Life on earth is maintained by the conversion of solar energy into chemical energy by biological photosynthesis carried out by plants and cyanobacteria [76]. In this process sunlight converts water and carbon dioxide to oxygen and the reduced or-

ganic species that serve as fuel and food, respectively. One of the most fascinating aspects of natural photosynthesis is the sophisticated self-organization of each component, as represented in Figure 1-9. In the natural photosystems, dozens of chlorophyll molecules within the light-harvesting complex are capable of capturing photons and transferring the photon energy to a reaction center in the photosystem (PS) complex. This energy absorption and transduction process highly depends on both spatial and molecular configurations of the pigments [71]. In the reaction center, photon energy is converted to a pair of spatially separated charge carriers: that is, an electrochemical potential across a thylakoid membrane. The key feature of this natural process is that light absorption and charge separation are decoupled and optimized for photosynthesis. Another interesting feature is that a relatively large number of molecules are used for photon harvesting, while a small number of reaction centers induce the charge separation. The stoichiometry of the functional molecules can be very important for the optimization of photosynthetic reaction kinetics by synchronizing multiple events. Once charge separation is complete in the reaction center, subsequent multistep charge transfer occurs along the array of chromophores embedded in the transmembrane protein, in a sequence from the dimer, to the accessory chlorophyll, pheophytin, quinones, producing a charge-separated state across a low dielectric membrane with a quantum efficiency of nearly 100 %. It finally results in the local creation of an about 1 V electrochemical potential difference. The primary electron donor is either chlorophyll or bacteriochlorophyll, and the electron acceptor is bacteriochlorophyll (type I) or bacteriopheophytin (type II) [71]. The rate of charge recombination, which is the reverse process of the light harvesting process, is extremely low as charge stabilization occurs through metastable oxidation and reduction of internal donor and acceptor groups.

Light harvesting antenna have an structure templated with proteins that can effectively increase the frequency and effective cross section for light absorption. For

instance, the light-harvesting (LH) 1 complex contains LH1-α and LH1-β polypeptides that have molecular weights of about 6 kDa and contains about 65 % α-helical character based on far-UV and circular dichroism (CD). Olsen et al. proposed a model for the structure of the minimal unit of the LH1 complex from *Rhodobacter sphaeroides* [7]. A site-directed mutagenesis was used to test the model and showed that a hydrogen bond between BChla and a tryptophan at the C-terminal region of the LH1 polypeptides plays an important role in the organization of BChla. The estimated rate of spontaneous photon absorption is 1.7 x 10^{-2} to 1.7 x 10^{-3} s^{-1}, which is a practical limit to antenna molecular size. Calculations based on either energy transfer kinetics or hopping kinetics show a limit for antenna size of about 200 chromophores [71].

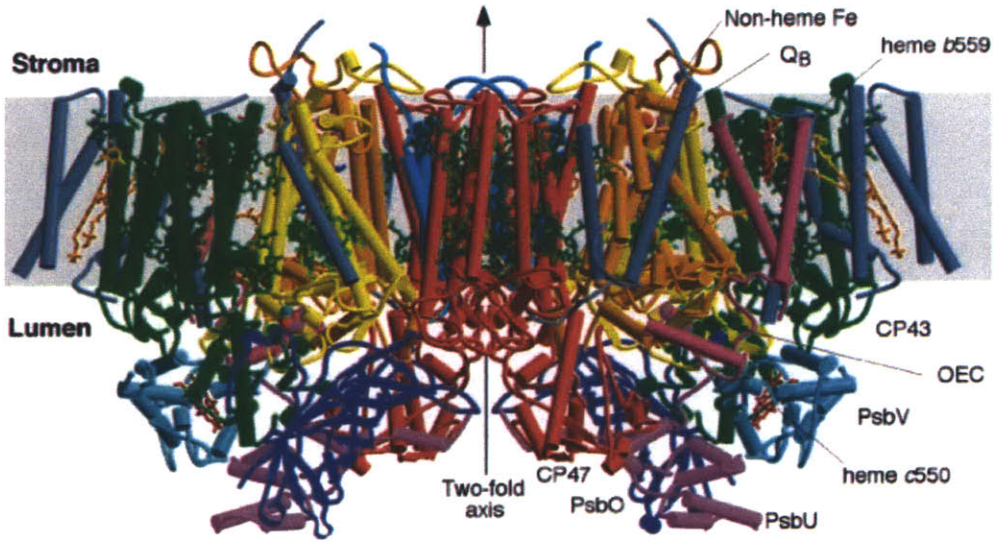

Figure 1-9: Overall structure of photosystem II isolated from *Thermosynechococcus elongatus*. OEC stands for oxygen-evolving center where oxygen is generated as a result of water splitting. Cylindrical molecules are peptide alpha-helices. Green (and some orange) molecules between cylinders are pigments that harvest the solar energy. They are well-interconnected to increase the energy transfer efficiency. The image adapted from Ferreira *et al. Science* (2004) 303: 1831.

A somewhat more intriguing situation occurs in the case of the photosynthetic apparatus. In higher plants, two reaction centers cooperate to produce carbohydrates

and oxygen from water and carbon dioxide. Photosystem I (PS I) functions at 700 nm (1.77 eV) and PS II functions at 680 nm (1.82 eV). The excess energy absorbed is lost as phonons. UV light is not absorbed by most plants because they do not have a capability of dealing with the high-energy photon in the UV region. The high-energy photons can induce genetic mutations of the plant's genome, induce apoptosis, and photochemically facilitate the degradation of LHCs. Low-energy photons are also not used for photosynthesis: hence, about 47 % of the energy from the available incident solar spectrum is out of the range that is used by the natural photosynthetic machineries. Given the spectral distribution of light on earth, the net energy has been shown to have a maximum of 9.2 %. If the energy consumed by the plant is excluded, a maximum net efficiency of about 5 % is commonly reported.

In purple bacteria, only cyclic electron transport takes place which resembles the operation of the solar cell. This similarity is more than superficial, as the operation of the photosynthetic system generates an electrostatic potential across the photosynthetic membrane (the bacterial wall), in addition to raising the concentration of the high-energy chemical species. Thus, the bacterial photosynthetic system provides, in some sense, a bridge between, and a generalization of, the photochemical and photovoltaic conversion mechanisms. The photosynthetic reaction center of purple bacteria consists of a protein complex which binds cofactors of the active branch of the electron transport chain: the primary electron donor (a bacteriochlorophyll dimer), a bacteriochlorophyll molecule (denoted by B), bacteriopheophytin H and a quinone Q. The quinone Q_B of the inactive branch forms the final electron acceptor in the chain: after reduction to Q_BH_2 it diffuses away from the reaction center, the ground state of the primary donor is replenished and the electron transfer cycle can start again. The electron transport occurs across a photosynthetic membrane and drives two energy sources for the bacterium: an electrostatic potential difference across the membrane, and a proton gradient. These are utilized by other enzymes embedded in

the membrane which are considered as 'users'-indicated by the meter symbol which has been labelled work. The overall electron transfer from P^* to Q occurs with a high quantum yield (> 90 %), indicating that the electron transitions between the reduced states are much faster than the recombination reaction from the reduced states to the ground state P. This has also been confirmed by direct measurements of all the transitions, with the exception perhaps of the reverse transition from P^+Q^- to P^+H.

1.4 Scope of Work

This work is based on the idea that the natural photosystems are sufficiently tractable, and the construction of model assemblies of nanosized metal oxide catalysts and organic pigments executing the process is achievable [71]. Accordingly, this dissertation deals with nanoscale materials assembled on genetically engineered virus scaffolds for photoelectrochemical cells for water splitting. Major issues include (i) how the nanoscale materials can be integrated into the macroscopic design of the final product and (ii) what advantages biological systems have for this purpose.

Chapter 2 describes the exciton migration among the porphyrins assembled on the M13 virus and discusses the application of the assembled porphyrins as light-harvesting nanoantennae for photochemical applications. Chapter 3 experimentally demonstrates the impact of the stable co-assembly of iridium oxide nanoparticles (as catalysts) and porphyrins (as photosensitizers) on the efficiency and stability of photochemical activity for water oxidation. Genetically modified M13 viruses are used as scaffolds for the co-assembly of metal oxide nanoparticles and organic pigments. Chapter 4 is concerned with the biomineralization of the genetically engineered M13 viruses encapsulated with polymer microgels. Chapter 5 describes the application of virus-templated iridium oxide nanowires to electrochromic applications. Finally, Chapter 6 is concerned with the preliminary study on the photochemical oxidation

of small organic molecules as an electron source using titanium oxide nanoparticles assembled on electrospun polymer nanofibers. This chapter is described from the viewpoint of the environmental application of the system to photochemical water purification.

Chapter 2

Virus-Templated Light-Harvesting Porphyrin Nanoantennae

Pigment assembly has drawn attention for its potential applications to sensors, photocatalytic systems, and photonic devices. The capsid proteins of viruses are very useful for assembling organic molecules because of their unique nanoscale structures and chemical diversities. This chapter describes the supramolecular organization of organometallic pigments into a photosensitizing nanostructure, as is found in the natural light-harvesting complexes. Zinc porphyrins are arranged into into a one-dimensional light-harvesting antenna on the M13 virus, and the the energy transfer between the assembled porphyrins are investigated.

2.1 Introduction

An electron can be promoted to an excited state by absorbing photons or phonons, by electrostatic interactions between neighboring molecules, or by electrical injection. Once in the excited state the electron tends towards the ground state, losing energy via both radiative and non-radiative processes. Various dissipative pathways complete for the energy of the excited state where individual contributions are determined by

the relative magnitudes of their rate constants. The energy states of molecules are determined by electronic, vibrational, rotational, and translational degrees of freedom. The electronic transitions with energy spacing of a few eV are dominant, and each electronic state corresponds to a bonding or anti-bonding molecular orbital. To each electronic level corresponds a vibrational manifold with typical sub-level spacings on the order of $\sim$ 0.1 eV, and to each vibrational sub-level corresponds a manifold of rotational and translational molecular energies with $\sim$ 0.01 eV interlevel spacing. Absorption of a photon can promote an electron from its σ, π, or n ground state to a σ^* or π^* excited state. Such electronically excited states of a molecule contain two unpaired electrons in different orbitals. The spin states of the two electrons can be either even or odd under exchange, giving rise to triplet (T_n) or singlet (S_n) states, respectively.[1] The ground state of organic molecules is practically a singlet state since molecular oribitals are almost always filled with paired electrons in the lowest energy state. The triplet state is typically at a lower energy than the corresponding singlet state. The orbital overlap must be significant so as to promote an electron from the lowest energy electron orbital Φ_0 to the excited-state orbital Φ_1. Since the Pauli's exclusion principle is not applied to electrons with antiparallel spins, they are on average closer and thus the average Coulomic repulsive energy is larger in the singlet state than in the triplet state: that is, the former has a higher energy. The singlet-triplet (S-T) energy difference varies according to the degree of spatial overlap of Φ_0 and Φ_1. Therefore, for (n, π^*) excited states where typically the overlap is small, the S-T splitting is smaller than for the (π, π^*) states where the molecular orbitals have a larger overlap.

In the natural light-harvesting complexes of cyanobacteria and plants, energy transfer is essential for increasing the exciton flux into the reaction center, where the electron transfer is triggered to drive photosynthesis [53]. Sophisticated self-

[1]The states of different spin multiplicity are separated horizontally in the Jablonski diagram.

organization of the natural photosystems serves as a model for artificial photosynthetic systems that require efficient energy and electron transfers [8, 48, 47, 17, 16]. Accordingly, the synthesis and supramolecular self-assembly of a variety of pigments have been widely explored with the aim of constructing photochemical and photoelectronic devices, including photovoltaics, nonlinear optical materials, and photoswitched conductors [24, 115, 22, 23, 70, 68]. Dendritic systems have been widely studied for multipigment arrays; however, it is very challenging and time-consuming to produce such complex molecules in a reasonable yield. Recent studies have shown that biological materials (*e.g.*, DNA, proteins, and viruses) can serve as templates guiding nanoscale organization of pigments via chemical linkage or electrostatic interactions [89, 29, 13, 26, 27]. Viruses are particularly attractive scaffolds because of their highly ordered coat protein structures and chemical diversity [109, 74, 55, 95, 75].

2.2 Metalloporphyrins linked to M13 viruses

The viruses have a filamentous structure composed of about 2,700 copies of α-helical proteins, named pVIII, which are symmetrically arrayed on the viral DNA to compose the about 880 nm long coat that is about 6.5 nm in diameter. The full amino acid sequence of the pVIII protein is as follows: EGDDPAKAAFNSLQASATEYIGYAWAMVVVIVGATIGIKLFKKFTSKAS. The chemical modification of the M13 coat proteins is straightforward because of the exposed N-terminus and lysine residue (both of them are indicated as arrows in Figure 2-1a) on the viral surface, which can be conjugation sites for pigments. In Figure 2-1b, the locations of primary amines are indicated as letters, **a**, **b**, **c**, and **d** for the N-termini, and **o** for the lysine. The calculated average distances between the N-termini and the lysine are $\overline{\mathbf{oa}} \approx 10.1$ Å, $\overline{\mathbf{ob}} \approx 16.8$ Å, $\overline{\mathbf{oc}} \approx 24.8$ Å, and $\overline{\mathbf{od}} \approx 24.2$ Å. Thus, it is highly probable that such close distances between the primary amines on the viral surface allow the energy transfer

to occur between neighboring pigments attached to the virus. Moreover, the flexible N-terminus of pVIII proteins may allow the attached pigments to have considerable freedom in their orientation and thus facilitate interactions between pigments.

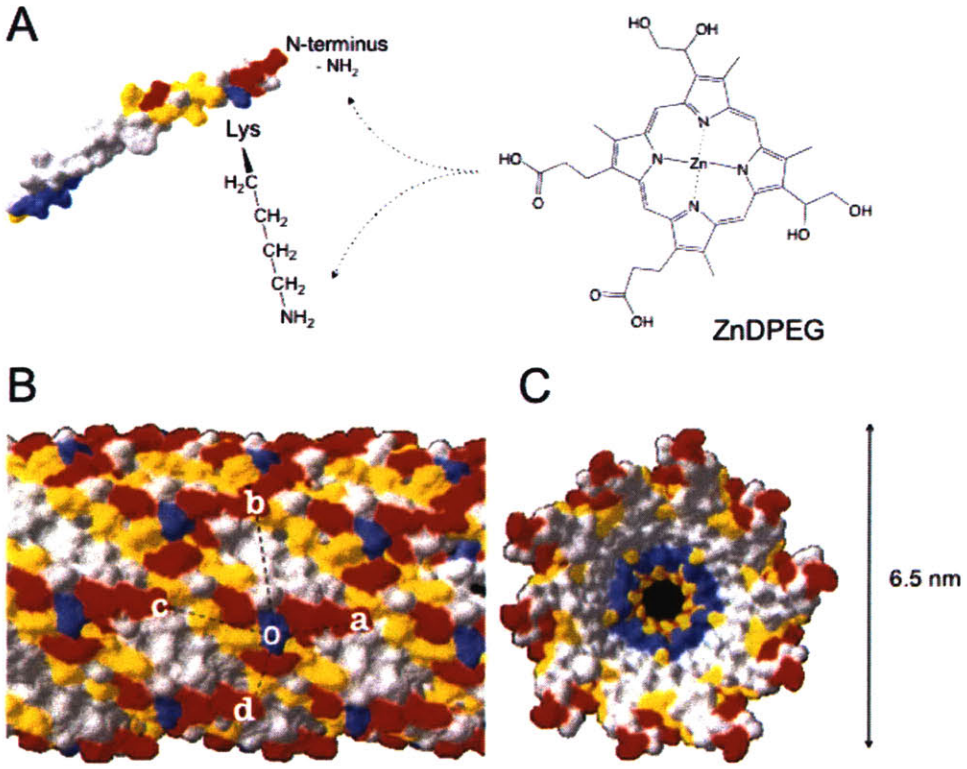

Figure 2-1: **Conjugation of zinc porphyrins to the M13 virus. A**, molecular model of a single pVIII representing negatively charged amino acids in red; positively charged ones in blue; neutral, hydrophilic ones in yellow; and hydrophobic ones in white (software: Swiss-PDB and structure model: 1IFJ). The arrows indicate the sites of primary amines to which ZnDPEG can be conjugated. **B** and **C**, side view (**B**) and cross section (**C**) of the assembled pVIII peptides. In (**B**), approximate locations of primary amines on the virus are indicated as letters, **a**, **b**, **c**, and **d** for the N-termini, and **o** for the lysine.

Zn(II) deuteroporphyrin IX-2,4-bis(ethylene glycol) (ZnDPEG, 2-1A) was chosen as a model pigment because of its well-known optical properties, water solubility, and pendant carboxylic groups. The zinc porphyrins were conjugated to pVIII via a carbodiimide coupling reaction. Carboxylic acids in ZnDPEG (0.5 mM, Frontier Sci-

entific, Inc.) were pre-activated by incubating with N,N'-dicyclohexylcarbodiimide (1 mM, Sigma-Aldrich) and N-hydroxysuccinimide (1 mM, Sigma-Aldrich) in anhydrous dimethyl sulfoxide for 1 h at room temperature. The activated ZnDPEG was then added to a virus suspension in 1 mM phosphate-buffered saline (PBS, pH 7.4) and incubated for 15 h with magnetic stirring at about 100 rpm. The virus concentration was 10^{10} pfu μL^{-1} as determined by the standard bacteriophage titer analysis. The detailed procedures are available at the New England Biolabs website (http://www.neb.com). Two different molar ratios of ZnDPEG to NH_2- were used: 1:1 for ZP-M13-1 and 3:1 for ZP-M13-2. The reaction mixture was centrifuged at 8,000 rpm for 2 min to remove the insoluble urea byproducts. The unreacted ZnDPEG was removed via dialysis (Spectra/Por® membrane 4, molecular cut-off: 12 $\sim$ 14 kDa, Spectrum, Rancho Dominguez, CA) against excess amount of deionized water in the dark for 2 days. When collected as pellets, the resulting ZnDPEG-conjugated M13 viruses (denoted ZP-M13) appeared red while unconjugated viruses were white (Figure 2-2). Two samples, ZP-M13-1 and ZP-M13-2, were prepared using different ratios of ZnDPEG and M13 viruses. Approximately, 1,564 and 2,900 porphyrins were conjugated per virus for ZP-M13-1 and ZP-M13-2, respectively. The number of ZnDPEG molecules conjugated to the virus was determined by measuring the zinc concentration using inductively coupled plasma-atomic emission spectrometry (ICP-AES, ACITVA, Horiba Jobin Yvon, Edison, NJ). Three % hydrochloric acid was prepared by diluting 35.5 % hydrochloric acid (reagent grade, Mallinckrodt Chemicals) with reagent grade water (Ricca Chemical Company) and used as a blank solution. A series of zinc solutions at different concentrations (10.0, 20.0, 40.0 and 80.0 ppm) was prepared by diluting a commercial zinc standard solution (Ultra Scientific, Inc.) with the prepared 3 % dilute hydrochloric acid. The porphyrin-virus conjugates were also diluted with hydrochloric acid (the final concentration = 3 %). The zinc calibration curve was validated within a 1 % relative standard deviation,

which is defined as the ratio of the standard deviation to the average multiplied by 100.

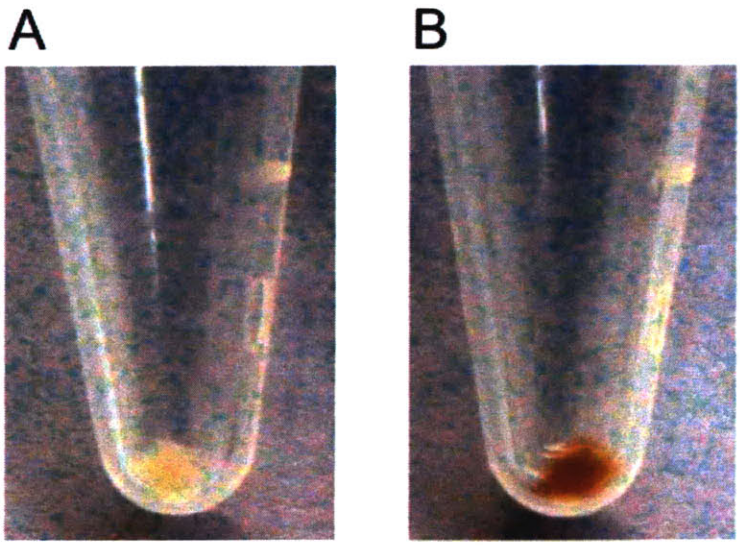

Figure 2-2: **The photographic images of M13 virus pellets (A) and ZP-M13-2 pellets (B).** The pellets were obtained via centrifugation of the virus solution after incubation in 4 % polyethylene glycol (nominal molecular weight of 8 kDa) and 0.5 M NaCl at 4°C for 12 h.

2.3 Structural characterization

The transmission electron microscopy (TEM) images of porphyrin-M13 nanoantennae were taken on a 200CX electron microscope (JEOL, Akishima, Japan) at 200 kV after negatively staining with 1 wt% uranyl acetate. Atomic force microscopy (AFM) images were obtained with a Nanoscope IV (Digital Instruments, Sterling Heights, MI) in tapping mode under ambient conditions using etched silicon cantilever tips. M13 viruses are relatively flexible and thus easily contorted on a flat surface [60]. Interestingly, however, ZP-M13-2 exhibited a very straight structure, as shown in Figure 2-3 and 2-4. Such a morphological change in ZP-M13-2 is thought as a result

of the interactions of the hydrophobic, π-conjugated macrocycles of the porphyrin with the viral coat protein.

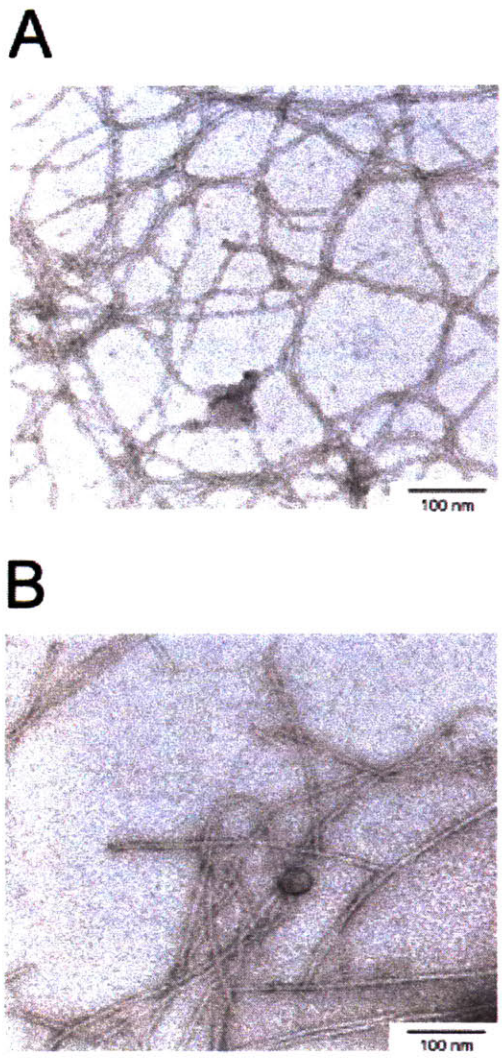

Figure 2-3: Transmission electron micrographs of native M13 viruses (**A**) and ZP-M13-2 (**B**) after negatively staining with 1 wt% uranyl acetate.

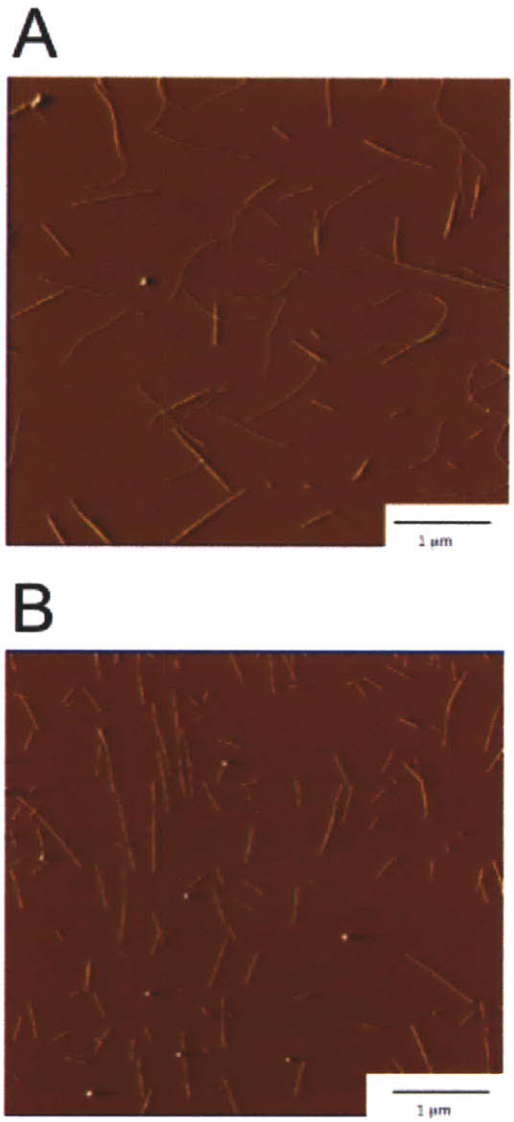

Figure 2-4: **Atomic force micrographs** of native M13 viruses (**A**) and ZP-M13-2 (**B**) on mica. The measured thickness of ZP-M13 is 2.7 ± 1.2 nm, which is significantly smaller than 4.7 ± 1.6 nm of native M13 viruses (the number of measurements ≥ 15).

2.4 Spectroscopic analyses

Accordingly, the tryptophan fluorescence of ZP-M13 was considerably lower than that of native M13 viruses (Figure 2-5). Fluorescence emission spectra were recorded on a FluoroLog-3 spectrofluorometer (Horiba Jobin Yvon, Edison, NJ). This change indicated the conformational change of pVIII; that is, the tryptophan residues were exposed to the outer aqueous environment presumably through their interaction with the attached porphyrins. Protein structures in the natural light harvesting complexes play a critical role in modulating the site energy levels of individual pigments via interactions with protein residues and neighboring pigments, which in turn affect the pathway of excitation energy transfer [105]. Such protein matrix effects could be observed in the absorption spectral changes of ZP-M13-2. Absorption spectra were obtained on a DU 800 spectrometer (Beckman Coulter) at ambient temperature with a 0.8-cm path-length quartz cuvette. Figure 2-6 shows the absorption spectrum of monomeric ZnDPEG monomers exhibited a strong Soret band at 406 nm and two weak Q bands at 538 nm and 574 nm. Compared to free ZnDPEG, the porphyrins assembled on the virus had a considerably broader Soret band with a reduced intensity at the similar peak wavelength. This spectral broadening can be explained by the diverse pigment-protein interactions, which generate different site energies of the excited states. Such heterogeneous microenvironments of the viral surface are illustrated by the various surface functional groups, as shown in Figure 2-1b, rendering diverse local effects of dipole-dipole interactions and hydrogen bonding to the attached porphyrins.

In order to determine whether excitons migrate along the pigments assembled on the virus, pump-probe transient absorption spectroscopy was used (Figure 2-7). The transient absorption change of the Soret band (Figure 2-8) indicated that the excited state of ZP-M13 was relaxed significantly faster than that of ZnDPEG, implying the delocalization of the excitions through the pigments assembled on the virus. The

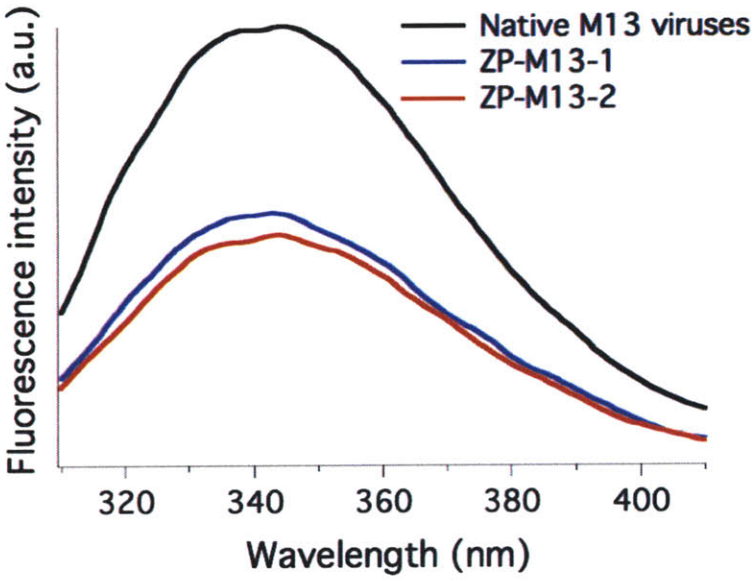

Figure 2-5: **Tryptophan fluorescence emission spectra** of native M13 viruses and ZP-M13 with excitation at 295 nm.

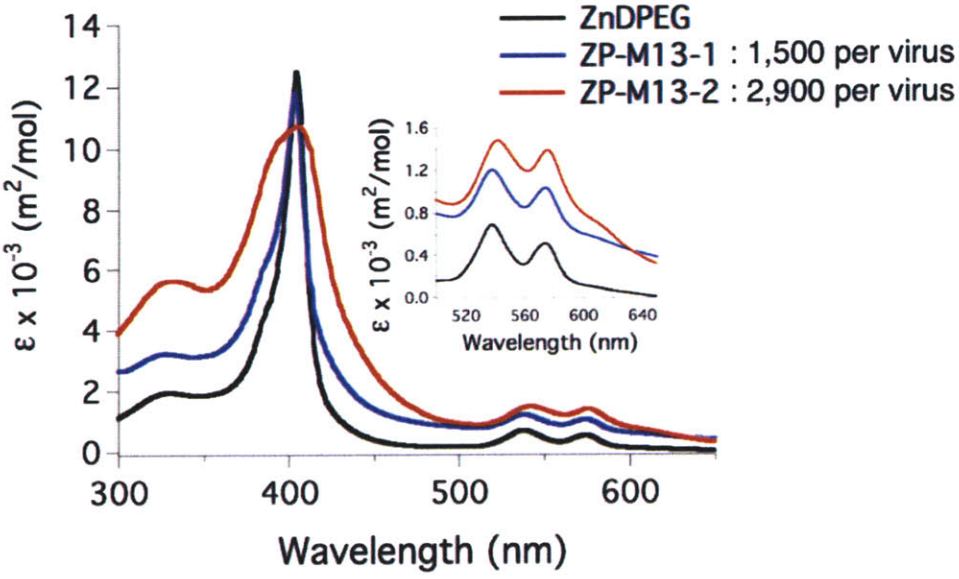

Figure 2-6: **Absorption spectra of ZnDPEG and ZP-M13.** In the y-axis, ϵ denotes the molar extinction coefficient. The insert shows a magnified version of the spectra of the Q bands.

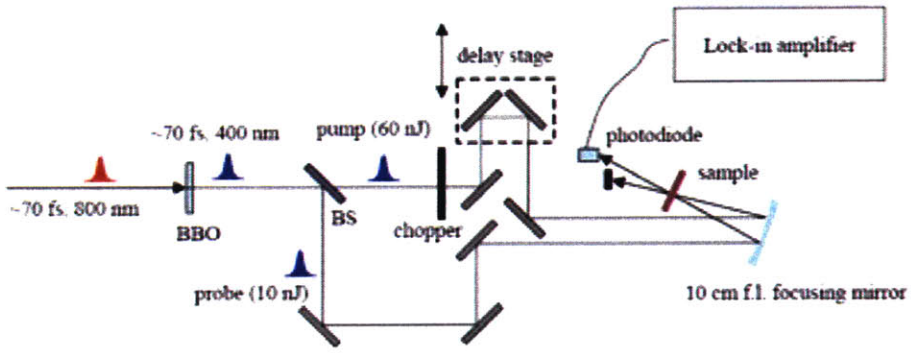

Figure 2-7: **Experimental set-up for pump-probe transient absorption measurements.** A 1 kHz Ti:sapphire regenerative amplifier system produces 70 fs optical pulses centered at 800 nm. The frequency of such pulses was doubled using a 0.1 mm-thick type-I BBO, and the optical beams were split into a pump and probe arm. The pump beam was time-delayed with a motorized translation stage. The energies of pump and probe were adjusted to 60 nJ and 10 nJ, respectively, and focused at the sample in a cuvette of 500 μm-pathlength. To supply a fresh sample for each laser shot, the sample solution was flowed through the cuvette at a constant flow rate of about 50 μm ms^{-1}. The pump beam was chopped at a rate of 500 Hz and the modulated probe beam intensity was recorded with a lock-in amplifier via a photodiode.

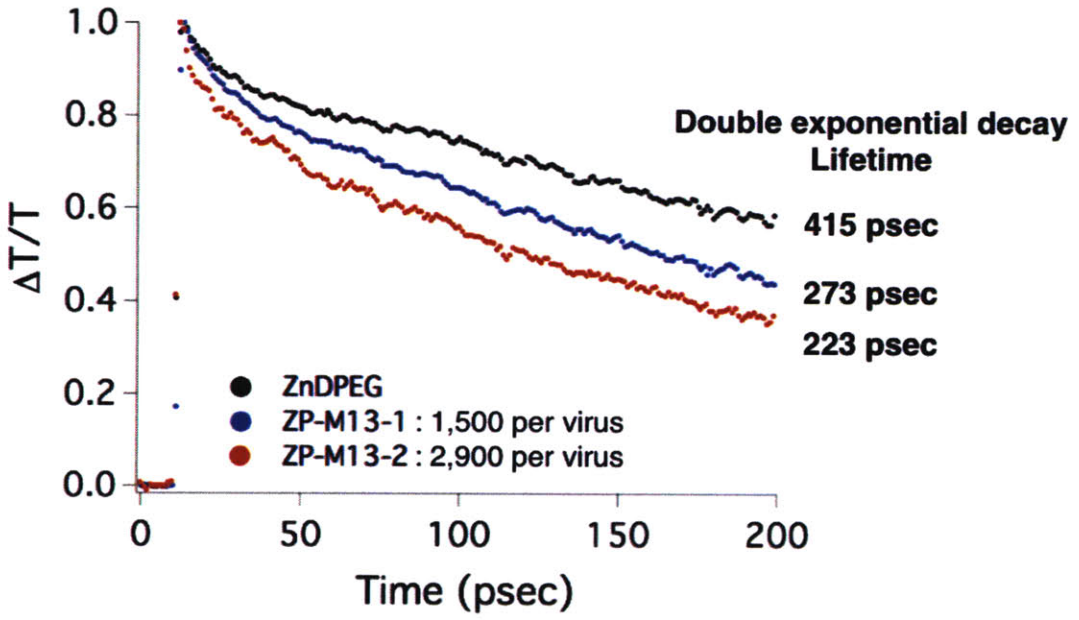

Figure 2-8: **Transient absorption decay profiles** of ZnDPEG and ZP-M13 at 400 nm.

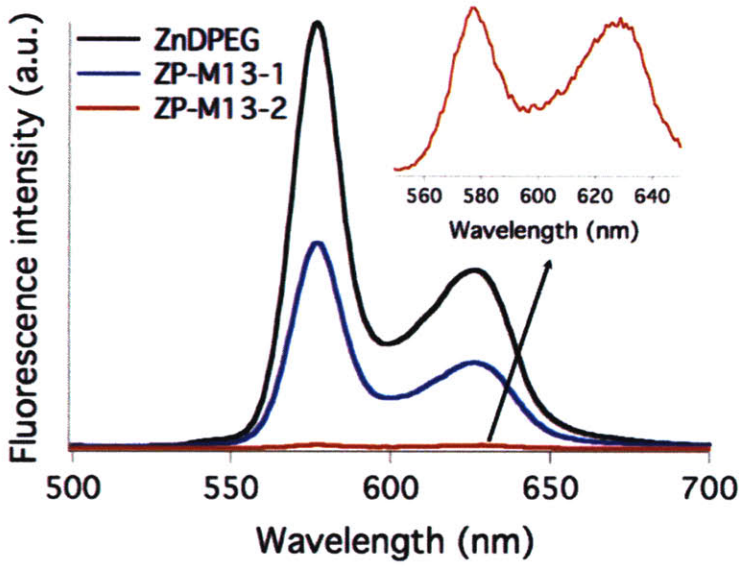

Figure 2-9: **Fluorescence emission spectra** of ZnDPEG and ZP-M13 with excitation at 400 nm. The insert shows a magnified version of the fluorescence emission spectrum of ZP-M13-2.

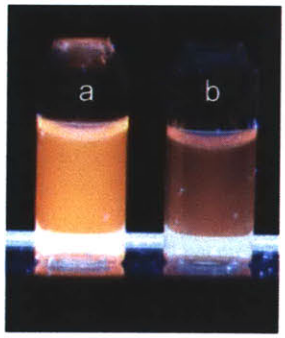

Figure 2-10: Photographic images of the solutions of ZnDPEG (**A**) and ZP-M13 (**B**) under illumination at 365 nm.

relatively long distance between the pigments assembled on the virus (about 3.5 nm in average for ZP-M13-2) and no significant shift of the Soret band in the absorption spectrum of ZP-M13 suggest that such exciton delocalization is driven via the Fŏrster resonant energy transfer (FRET), though the Dexter mechanism seems to contribute to fluorescence quenching process as described below.

The most dramatic optical variation of ZP-M13 was the quenching of the fluorescence emission (Figure 2-8 and 2-10). This effect can be explained by a small red shift found in the Q bands of the absorption spectrum of ZP-M13 ($538 \sim 543$ nm and $574 \sim 577$ nm, respectively) (Figure 2-6). It is known that the red shift of the Q bands reflects the formation of the electronic coupling between pigments although such interaction may be not very strong in the ZP-M13 presumably because the porphyrin used in this study lacks of meso-substituents, which are known to stabilize the J-type aggregates [102]. The orbital disordering caused by the pigment-pigment interactions may induce a significant change in the nuclear coordinates of the excited state relative to the ground state. This change caresult in the formation of trap sites where the rate of non-radiative relaxation is much larger than the radiative transition rate. This explanation is supported by the result that the fluorescence quenching increases with increasing degree of conjugation, which implies that the electronic interactions between porphyrins are essential for the quenching process [30]. Therefore,

the photons absorbed by the pigments assembled on the virus seem to travel through long-range dipole-dipole interactions and quenched in the trap sites generated by the electron coupling of the pigments, as illustrated in Figure 2-11.

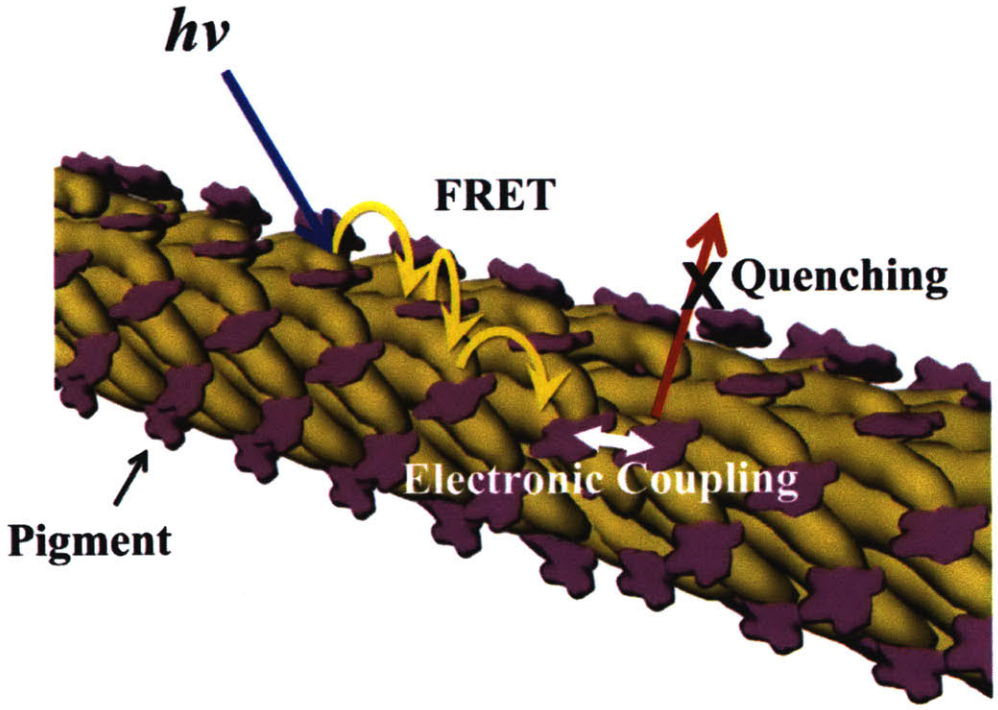

Figure 2-11: **A hypothetical model to explain the energy transfer occurring in the supramolecular porphyrin structures templated with the virus.** Chemical grafting of porphyrins to M13 viruses induces distinctive spectroscopic changes, including fluorescence quenching, the extensive band broadening and small red-shift of their absorption spectrum, and the shortened lifetime of the excited states. Based on these optical signatures, it was expected that further genetic engineering of M13 viruses can allow us to co-assemble other functional materials (*e.g.*, catalysts and electron transfer mediators) with pigments, implying potential applications to photochemical devices, which is the topic of the following chapters in this dissertation.

2.5 Conclusion

In summary, chemical grafting of zinc porphyrins to M13 viruses induces distinctive spectroscopic changes, including fluorescence quenching, the extensive band broadening and small red-shift of their absorption spectrum, and the shortened lifetime of the excited states. Based on these optical signatures a hypothetical model was suggested to explain the energy transfer occurring in the supramolecular porphyrin structures templated with the virus. Although the precise control of energy transfer is not presented, this study showed that the energy transfer of the assembled pigments might be controllable by genetically inserting or deleting amino acids on pVIII, which may modify the site energies and the pigment-pigment distances. Through genetic engineering, catalysts and electron transport mediators can be co-assembled with pigments on M13 viruses. It was expected that such co-assembled nanostructures would be applied to photochemical devices which often require a large charge flux to catalytic sites through energy transfer. The following chapters address this issue using the genetically engineered M13 virus displaying a binding peptide for electrochemically active inorganic catalysts.

Chapter 3

Virus-Templated Co-assembly of Metal Oxide and Pigments for Photochemical Water Oxidation

Unique multi-scale structures of natural photosystems have evolved to efficiently handle complex photochemical processes. This chapter is dedicated to the investigation of the use of biological scaffolds to spatially organize multiple functional materials for photochemical water oxidation. Viruses can serve as versatile templates for assembly of various materials through both genetically controllable biomineralization and chemical linkage. Here, genetically modified M13 viruses are used to co-assemble metalloporphyrins and catalytic metal oxide nanoclusters into photocatalytic hybrid nanostructures. The metalloporphyrins are placed in close enough proximity to each other to allow excitonic migration, which increases the photosensitization efficiency, as described in the previous chapter. This chapter focuses on the impact of the co-assembly of metalloporphyrins with nano-sized metal oxide catalysts on oxygen evolution by photochemical water oxidation. A microfluidic technique is also employed to physically stabilize such co-assembled hybrid nanostructures within a hydrogel matrix.

3.1 Electron Transfer

Many biochemical processes, such as photosynthesis and respiration, are operated in a very complex system relying on electron transfers between cofactors in proteins. A simple description of electron transfer has been proposed by Rudolph A. Marcus.[1] It is basically similar to the way to describe that chemical reactions in an energy-vs-reaction coordinate diagram. The energy level of a molecule as a function of nuclear displacement is represented using a parabola. In Figure 3-1, ΔG is the free energy change between the molecules, electron acceptor and doner and ΔE is the activation energy. λ is the rearrangement energy, which is the amount of energy required to distort the nuclear configuration of the electron doner to have the same configuration as the electron acceptors without electron transfer occurring. The point of crossing between the parabolas and the transfer rate (from ΔE) can be derived from the Figure 3-1. Let me set the bottom of the doner and acceptor at the point of (0, 0) and (a, b), respectively. The intersection of the two parabolas is then (x,y) = ($\frac{(b-a)^2}{2a}$, $\frac{(b-a^2)^2}{4a^2}$). As the y-value of the intersection is ΔE and $\lambda = a^2$, the activation energy and the rate constant of electron transfer (k) are as follows:

$$\Delta E = \frac{(\Delta G + \lambda)^2}{4\lambda} \tag{3.1}$$

$$k = A \exp\left(-\frac{(\Delta G + \lambda)^2}{4\lambda RT}\right) \tag{3.2}$$

The coefficient A is often expressed as an exponential term itself depending upon the distance (r) between the electron doner and acceptor:

$$k = C \exp\left(-\beta r\right) \exp\left(-\frac{(\Delta G + \lambda)^2}{4\lambda RT}\right), \tag{3.3}$$

[1]Rudolph A. Marcus is currently a professor at California Institute of Technology. His theory of electron transfer, named 'Marcus theory', was recognized by the 1992 Nobel Prize in Chemistry.

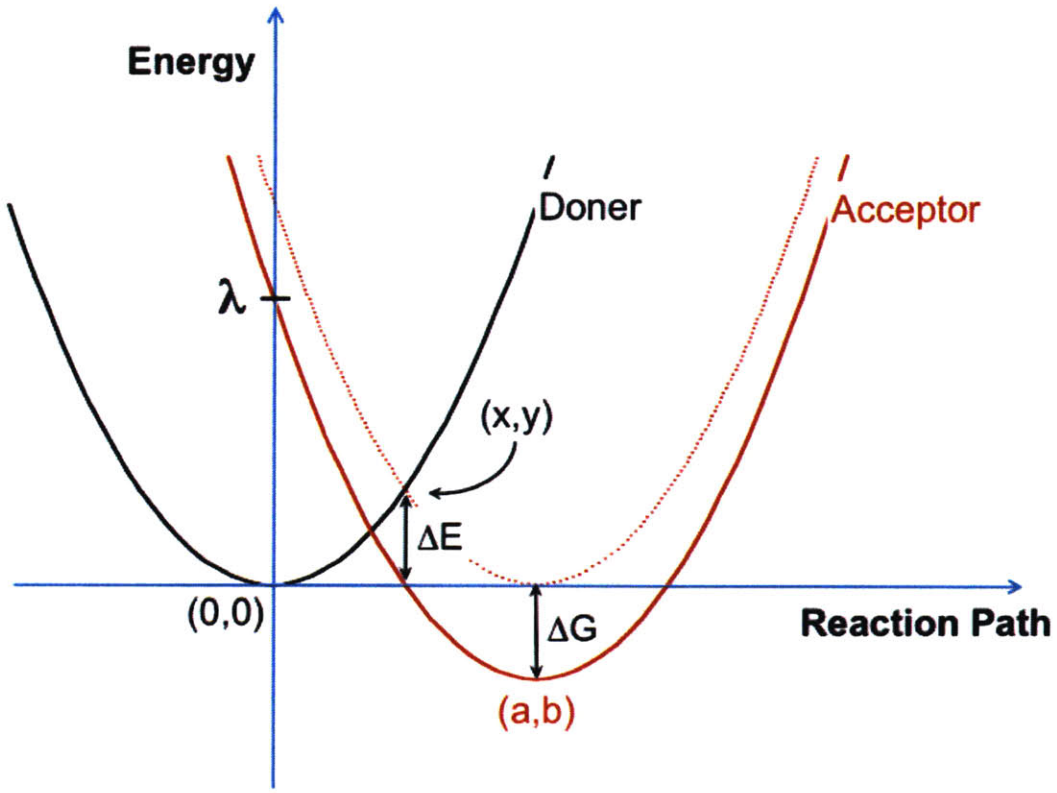

Figure 3-1: **Schematic description of the potential energy curves used in Marcus theory.** The barrier to charge separation (ΔE), the overall Gibbs free energy change (ΔG) and the total reorganization energy (λ) are represented.

where C is a constant, β is a factor which depends upon the properties of the medium between the molecules, R is the ideal gas constant (8.314472 J K^{-1} mol^{-1}), and T is thermodynamic temperature (K). From the above expression, the rate of electron transfer can be calculated using the given properties of the system, including the free energy, the reorganization energy, temperature, and β. Note that the maximum rate constant for electron transfer occurs when λ is equal to $-\Delta G$, and k decreases with decreasing ΔG if it has past the point where it cancels out λ.

3.2 Light-driven Water Oxidation Based On Metal Oxide Colloids Coupled With Pigments

Multiple attempts to mimicking natural photosystems for light-driven water oxidation have had limited success; most require oxygen-transfer oxidants to catalyze oxygen formation [116]. Until now, the most promising systems are based on metal oxide colloids (*e.g.*, ruthenium oxide, manganese oxide, cobalt oxide, and iridium oxide), which drive the photochemical oxidation of water with several different components cooperatively: a photosensitizer (*e.g.*, porphyrins and ruthenium complexes) absorbs visible light and subsequently transfers an electron to an electron acceptor, stimulating the transfer of a hole from the photosensitizer to the catalyst [67, 64, 63, 65, 49, 37, 93, 45, 92, 51, 50, 44, 43, 42]. Repeated cycles of light absorption lead to the accumulation of four holes in the catalyst and the holes drive the evolution of a molecule of oxygen from water ($2H_2O \rightarrow O_2 + 4H^+ + 4e^-$). Distances between functional components are critically important in these colloidal systems; non-optimal spacing between photosensitizer, electron acceptor, and catalyst can kinetically promote corrosive mechanisms, leading to the degradation of catalytic materials [93, 45]. Various approaches to developing efficient, sustainable metal oxide catalysts driven by visible light have been undertaken; these approaches include the polyelectrolyte-mediated

complexation of catalysts and photosensitizers [93], ligand design [50], and heterogeneous catalysts [46, 42]. However, it is very challenging to design multi-component systems with controlled structural arrangement at the molecular level; the lack of this precise arrangement can hinder the appropriate trafficking of chemical and electron species between individual active components [50]. Polymers are often used as intermediate binders to couple photosensitizers to the surface of metal oxide catalysts [42, 93]. These polymers, however, often undergo conformational variations during charge building and the subsequent chemical reactions. These structural changes can affect the distances between and relative orientations of catalysts and photosensitizers, which in turn highly affect charge transfer kinetics [39]. Therefore, to formulate efficient, sustainable photochemical water splitting systems, it is important to generate and maintain structurally stable and controllable microenvironments that can coordinate complicated electrochemical events.

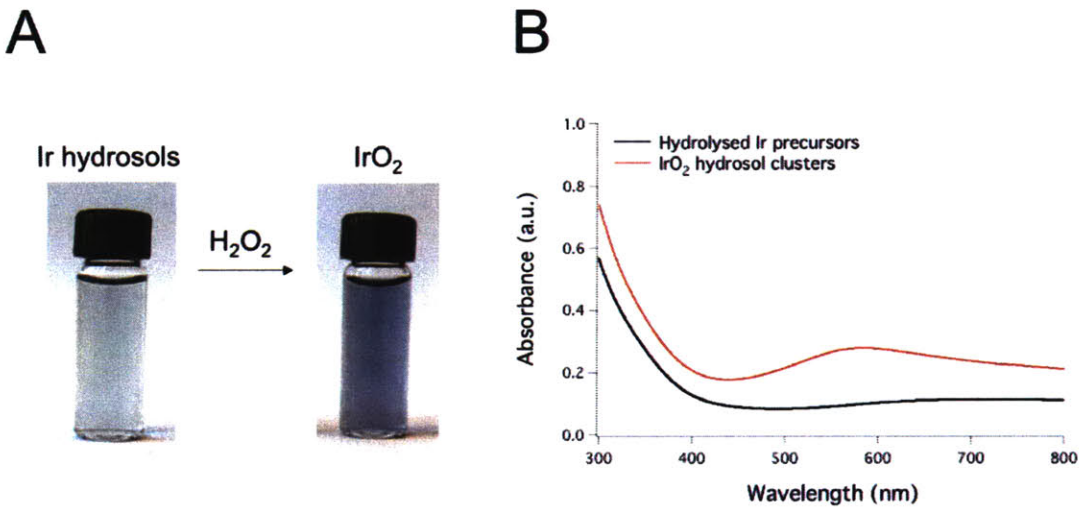

Figure 3-2: **Synthesis of IrO_2 hydrosol clusters.** Photographs (**A**) and absorption spectra (**B**) of the hydrated Ir precursors and the IrO_2 hydrosol clusters.

3.3 Synthesis of Iridium Oxide Nanostructures

Iridium oxide (IrO_2) was chosen as a water oxidation catalyst because of its well-known catalytic activity and stability under oxidizing conditions [98, 46, 45, 50, 43]. To synthesize the IrO_2 nanoparticles, hydrated sodium hexachloroiridate ($Na_2IrCl_6 \cdot 3H_2O$, Alfa Aesar) was hydrolyzed with (sodium) citrate as a ligand. An aqueous mixture of sodium hexachloroiridate (1.5 mM) and sodium citrate (4.8 mM) were stirred at 90°C for 4 h followed by rapid cooling to 20°C for 15 min in a water bath. The solution was stirred with 20 g ion exchange resin Monobed MB1 (Sigma-Aldrich) for 30 min to remove the unbound citrate. The resins were then removed by filtration. H_2O_2 was added to the solution at the final concentration of 0.2 % to chemically oxidized the Ir hydrosols into IrO_2 nanoparticles, and then the solution was incubated while exposed to air at room temperature for at least 24 h. The formation of IrO_2 was indicated by the appearance of a characteristic absorbance peak around 600 nm (Figure 3-2a). The Ir concentration was determined by ICP-AES at 224.268 nm.

The water content of IrO_2 hydrosol ($IrO_2 \cdot xH_2O$) at the surface of the nanowires was $x = 1.94$ as determined by X-ray photoelectron spectroscopy (XPS) analysis (Figure 3-5). The calculated density of $IrO_2 \cdot xH_2O$ is 4.62 g cm^{-3}, which corresponds to 9.31 x 10^{-29} m^3 per molecule of the specific volume of a single $IrO_2 \cdot xH_2O$ molecule. If a spherical shape of the molecule is assumed, the calculated radius of $IrO_2 \cdot xH_2O$ is about 2.81 Å. If a square packing of $IrO_2 \cdot xH_2O$ molecule on the viral surface is assumed, the number of the reactive sites per unit area is 3.16 x 10^{18} per m^2. The particle size distribution of the IrO_2 hydrosol clusters was determined using a dialysis method. The calculated median particle size is 25 Å in diameter with the assumption of a Gaussian distribution. The IrO_2 hydrosol clusters are assumed to have a spherical shape, so the volume of the outer shell layer of the hydrosol clusters is about 4.37 x 10^3 $Å^3$, which corresponds to 53% of the total volume of an IrO_2 hydrosol cluster. As for the IrO_2 nanowires, the surface area of the IrO_2 nanowires is 57.4 m^2g^{-1}, as

measured by BET analysis (Figure 3-6). The amount of IrO_2 used for the oxygen evolution is 0.49 μmoles, and hence the total surface area of the IrO_2 nanowires used is 7.28 x 10^{-3} m^2. Then, the total number of the reactive sites on the nanowire surface is 2.30 x 10^{16} or 38.20 nmoles; *i.e.*, about 7.7 % $IrO_2 \cdot xH_2O$ was exposed to the surface.

M13 viruses carrying the IrO_2 binding peptide, AGETQQAM, on the major coat protein were identified through biopanning against IrO_2 using an M13 library displaying random octameric peptides [74]. These engineered M13 viruses were used as templates for self-assembly of IrO_2 nanoscale structures in the shape of nanowires, as shown in Figure 3-3. Virus-templated IrO_2 nanowires were synthesized through the self-assembly of the IrO_2 hydrosol nanoclusters on the engineered M13 viruses. Ir hydrosol nanoclusters were prepared by hydrolyzing aqueous sodium hexachloroiridate in the presence of citrate as a ligand. The viruses were then incubated with the Ir hydrosols for 30 min before chemical oxidation into $IrO_2 \cdot xH_2O$ using hydrogen peroxide. The formation of IrO_2 nanowires was confirmed by TEM (Figure 3-3). The freeze-dried IrO_2 nanowires were amorphous as examined using a Bragg Brettano powder X-ray diffractometer (Rigaku) with Cu-Kα radiation at 18 kW (Figure 3-4). A commercial $Ir^{(IV)}O_2$ powder (99.9 %, Sigma-Aldrich) was used as a control.

3.4 Chemical Linkage of Zinc Porphyrins to IrO_2-binding M13 Viruses

As a photosensitizer, Zn(II) deuteroporphyrin IX-2,4-bis ethylene glycol (ZnDPEG) was selected for its optical and electrochemical properties as well as its functional groups (see Figure 2-1). The redox potentials of ZnDPEG were analysed using a potentiostat (Autolab PGSTAT302, Eco Chemie B.V., The Netherlands) with a pair of platinum meshes as working and counter electrodes and a Ag/AgCl reference elec-

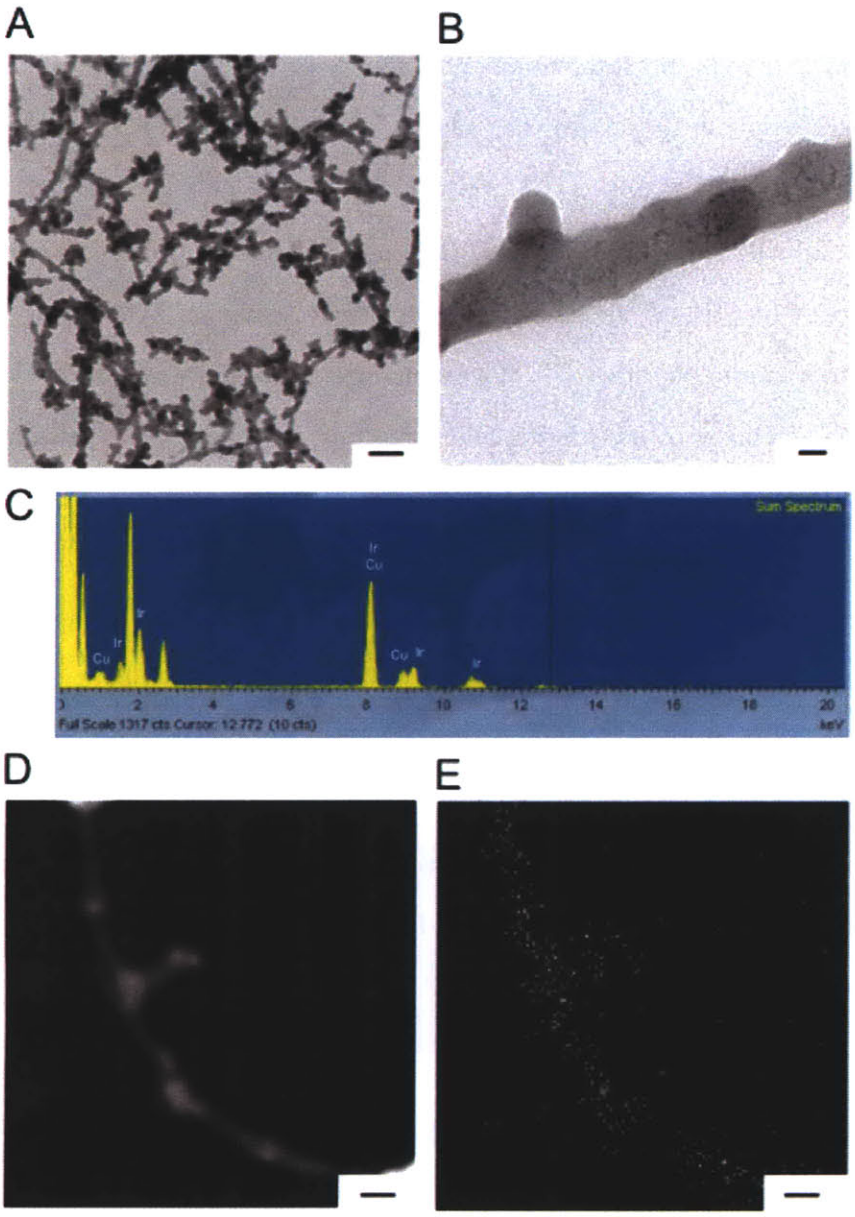

Figure 3-3: **Electron microscopic analysis.** **A**, **B**,TEM images of the virus-templated IrO_2 nanowires obtained on JEOL 200CX. Scale = 100 nm (**A**) and 10 nm (**B**). **C**, Energy-dispersive X-ray (EDX) spectrum of the IrO_2 nanowires. **D**, **E**, Scanning transmission electron microscopy (STEM) image (**D**) and elemental mapping (**E**) of the IrO_2 nanowires obtained on JEOL 2010F. White dots indicate Ir elements in (**D**). Scale bar = 40 nm (**D** and **E**)

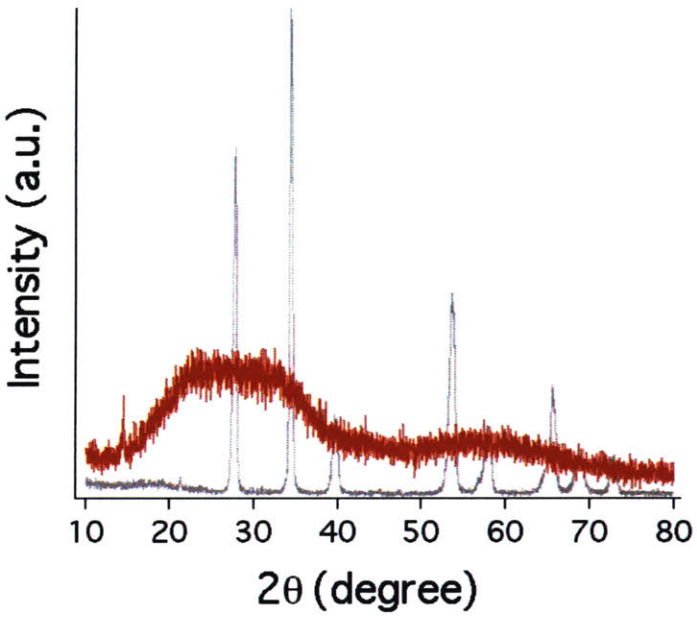

Figure 3-4: X-ray diffraction spectra of the prepared IrO_2 nanowires (red) and commercial IrO_2 powder (gray).

trode. Sodium borate (6.6 mM, pH 11) was used as an electrolyte after argon purging to remove dissolved oxygen. The current responses were measured with changing voltage sweeping rates in the range of $10 \sim 70$ mV s^{-1}, the results of which showed that its redox responses were diffusion-limited. Figure 3-7 shows the cyclic voltammogram of ZnDPEG (black curve) in the presence of ambient light. The solution was purged with argon for 10 min prior to scanning. The scan was initiated at 0 V with the cathodic polarization. At the scanning rate of 10 mV sec^{-1}, ZnDPEG exhibited peak currents of $i_{p,ox} \approx +$ 0.39 V and $i_{p,red} \approx$ - 0.36 V even though the oxidation potential was not clearly resolved. Under the same conditions, the redox responses of ZnDPEG were very similar to those of zinc tetrakis(4-sulphoatophenyl)porphyrin (ZnTSPP), which has been widely used for photochemical water oxidation.

A library of 10^{10} random octameric peptides displayed at the N-terminus of pVIII, the major coat protein, was constructed. The M13KE plasmid (New England Biolabs,

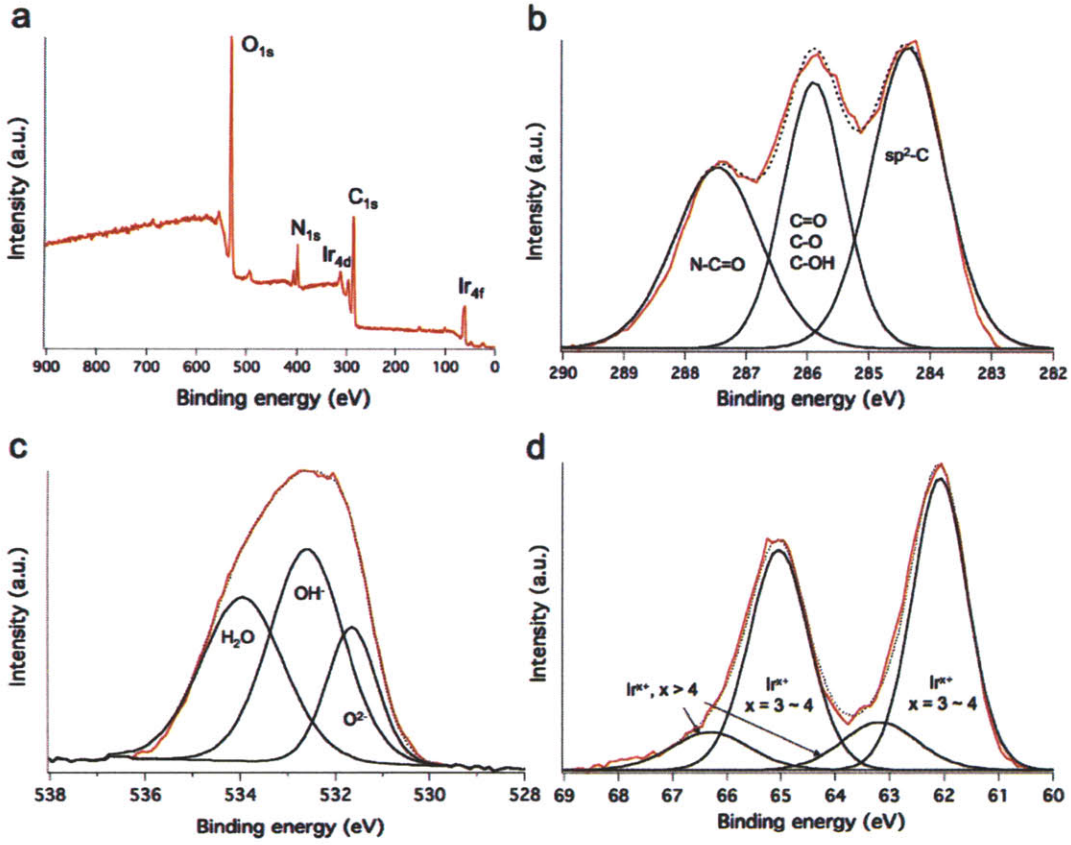

Figure 3-5: **XP spectra of IrO_2 nanowires.** The surface chemistry of IrO_2 nanowires was analysed using a Kratos Axis Ultra X-ray photoelectron spectroscopy (XPS) (Kratos Analytical, Manchester) with a monochromatized Al Kα X-ray source and the take-off angle of 90°. All spectra were calibrated with the C_{1s} emission peak for sp_3 hybridized carbons at 285.0 eV. A Shirley type background subtraction was performed to fit the obtained XP spectral curves. **A**, Wide scan survey. **B**, Fitted spectra for C_{1s}. The red curve represents the best fit to the spectral data. **C**, Fitted spectra for O_{1s}. The lowest binding energy is IrO_2 (O_2^-), the peak at intermediate binding energy is OH^-, and the highest binding energy peak is H_2O. **D**, Fitted spectra for $Ir_{4f5/2}$ and $Ir_{4f7/2}$. The Ir_{4f} levels were much higher than the $Ir_{4f7/2}$ binding energy of 60.9 eV for the Ir metal, indicating the formation of an oxide layer.

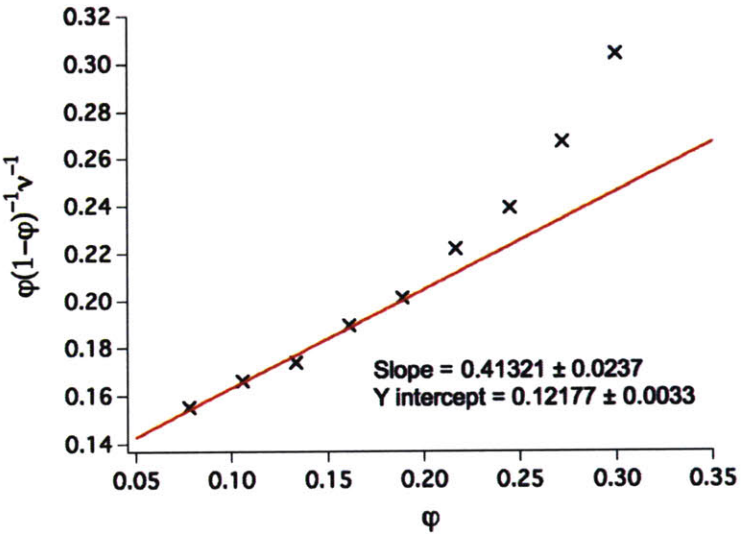

Figure 3-6: **Brunauer-Emmett-Teller (BET) isotherm of the IrO_2 nanowires.** The surface area of the freeze-dried IrO_2 nanowires was calculated from the BET isotherm (ASAP 2020, Micromeritics Instrument Corporation, Norcross, GA) of nitrogen. The samples were degassed for 1 h at 80°C under 10 μmHg followed by additional heating at 100°C for 5 h under 100 mmHg. The BET equation was plotted as a straight line with φ on the x-axis and $\varphi(1\text{-}\varphi)^{-1}\nu^{-1}$ on the y-axis, where φ is the ratio of the equilibrium pressure to the saturation pressure of adsorbates at the temperature of adsorption, ν is the adsorbed gas quantity. Due to a significant deviation at large φ values, only the first five points were used for linear regression with a confidence interval of 0.9937. The adsorption cross-section area was set to be 0.16 nm^2 for nitrogen gas.

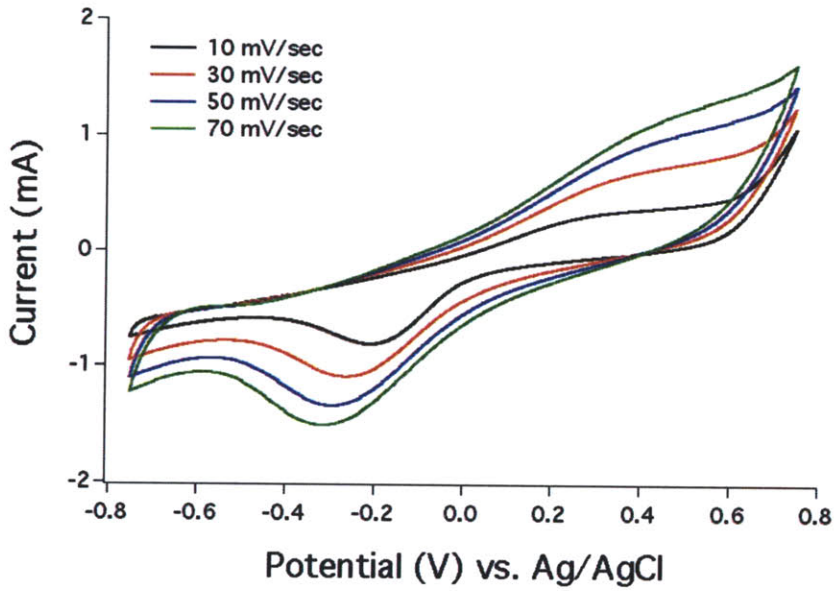

Figure 3-7: Cyclic voltammogram of ZnDPEG in Mill-Q water. The current responses were measured with changing the voltage sweeping rates from 10 to 70 mV s^{-1}.

Ipswich, MA) was modified to insert *PstI* and *BamHI* sites to the 5' end of the pVIII encoding region. After 3 rounds of biopanning against Ir(IV)O_2 powder (99.9 %), M13 viruses carrying a dominant binding sequence, AGETQQAM, in each copy of pVIII were isolated and identified.[2]

ZnDPEG was chemically grafted to the M13 major coat proteins via a carbodiimide reaction. Carboxylic acid groups in ZnDPEG were pre-activated with dicyclohexyl carbodiimide (DCC) and N-hydroxysuccinimide (NHS) at a molar ratio of 1:2:2 in anhydrous dimethyl sulfoxide (DMSO). The activated porphyrins were reacted to the primary amines of the M13 virus (5 x 10^8 pfu μL^{-1}) in phosphate buffered saline (PBS, pH 7.2) at room temperature for 4 h. The insoluble dicyclohexylurea was removed by filtration through 0.45 μm filter membrane, and unreacted porphyrins were eliminated by dialysis (MW cut-off: 12 $\sim$ 14 kDa) against Milli-Q water (18.2 MΩ·cm). The number of ZnDPEGs conjugated to the virus was determined by com-

[2]The phage library was constructed by Dr. Soo Kwan Lee and the biopanning experiments were performed by both Dr. Dong Soo Yun and Dr. Soo Kwan Lee.

paring the elemental ratio of phosphate to zinc. The M13 virus has a single stranded DNA of 6.4 kb, *i.e.*, 6,400 phosphates and 2,700 copies of the pVIII major coat proteins per virus. Each pVIII protein has two primary amines exposed to the viral surface. Accordingly, the theoretically highest ratio of P to Zn is 1.185, which indicates 5,400 ZnDPEGs attached to each virus. The P to Zn ratio was determined by inductively coupled plasma - atomic emission spectroscopy (ICP-AES) (ACTIVA, Horiba Jobin Yvon, Edison, NJ) with a calibration curve for P at 213.618 nm and Zn at 213.856 nm. The ZnDPEG-conjugated viruses were pretreated in 0.33 M HCl at room temperature overnight. Zn and P element standards were purchased from Ultra Scientific (Kingston, RI). ICP-AES analysis indicated that the molar ratio of Zn to P was 0.39:1, which corresponds to about 2,730 porphyrins per virus. The absorption spectrum of ZnDPEG in water shows a strong Soret band at 406 nm and weak Q bands at 538 nm and 574 nm (Figure 3-8). However, the conjugation of ZnDPEG to M13 viruses resulted in a significant broadening of the Soret band and a red shift of the Q bands (insert in Figure 3-8). In addition, the fluorescence emission spectra were recorded on a FluoroLog-3 spectrofluorometer (Horiba Jobin Yvon, Edison, NJ) with excitation at 400 nm. The fluorescence of the conjugated ZnDPEG was dramatically suppressed compared to that of unconjugated ZnDPEG (Figure 3-9). These spectral changes indicate that neighboring porphyrins linked to the virus are placed close enough to induce excitonic migration between them. The tryptophan emission spectrum of the ZnDPEG-conjugated viruses was compared with that of the native viruses. The conjugation of ZnDPEG to the viruses showed the fluorescence quenching ratio of about 2.38 at 340 nm without any significant spectral shift (Figure 3-10). These results indicated that the conjugation of ZnDPEG caused the conformational change of the pVIII coat proteins leading to the exposure of the tryptophan to more polar environment. However, no evidence on the energy transfer from tryptophan to ZnDPEG conjugated to the virus was observed.

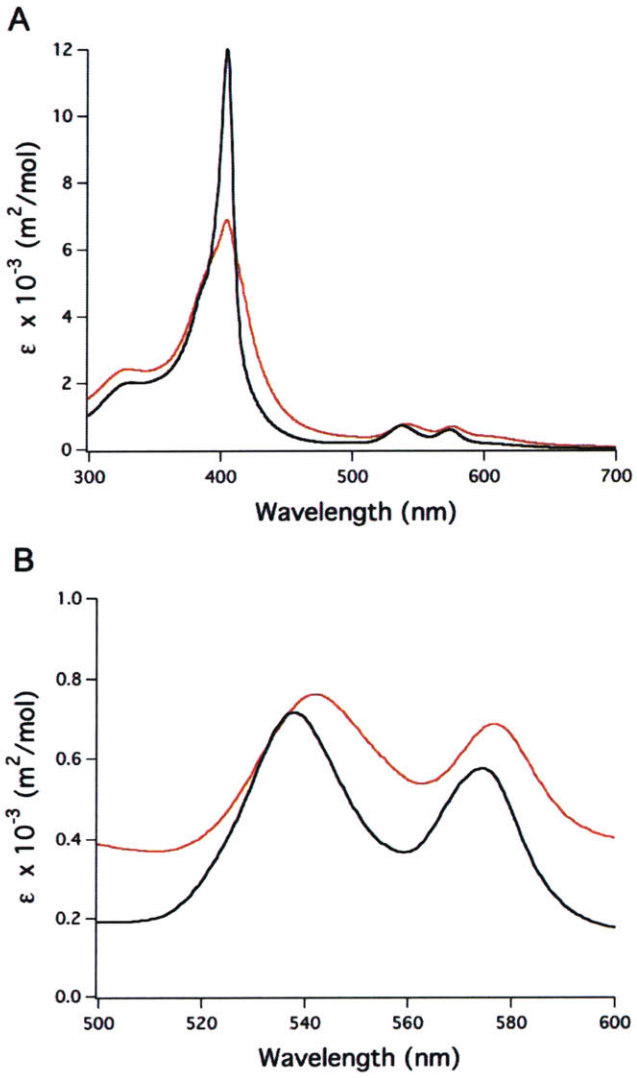

Figure 3-8: **Absorption spectra of porphyrins (black) and ZnDPEG-conjugated viruses (red).** The y-axis denotes the molar extinction coefficient (ϵ). **A** shows the full range of wavelength examined and **B** magnifies the Q-band region.

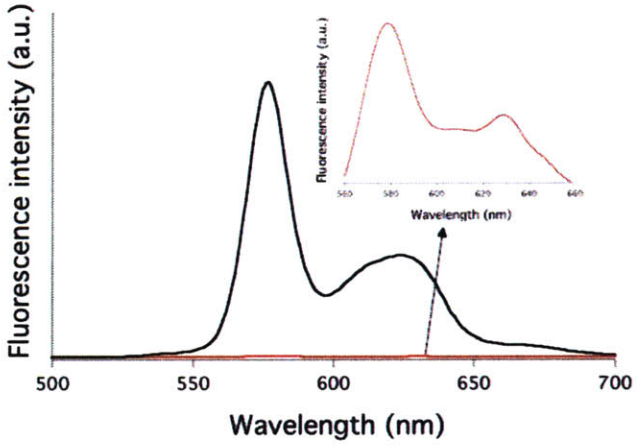

Figure 3-9: **Fluorescence spectra of monomeric ZnDPEGs (black) and the ZnDPEG-conjugated viruses (red) with excitation at 400 nm.** The insert is the magnified version of the spectrum of the ZnDPEG-conjugated viruses.

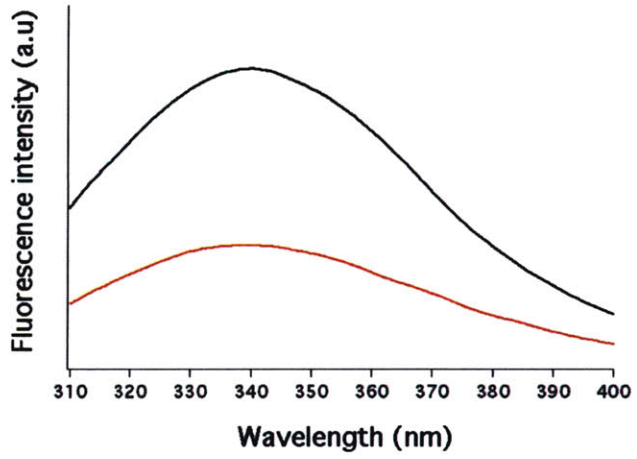

Figure 3-10: Tryptophan emission spectra of the unconjugated M13 viruses (black) and the ZnDPEG-conjugated viruses (red) with excitation at 295 nm.

3.5 Co-assembly of Zinc Porphyrins and Iridium Oxide

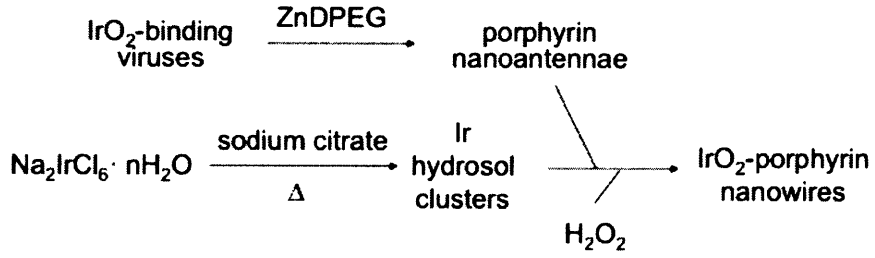

Figure 3-11: Schematic synthetic routes for IrO_2-porphyrin nanowires.

To synthesize the IrO_2 nanowires, aqueous Na_2IrCl_6 was hydrolysed to Ir hydrosols with citrates and mixed with the viruses carrying AGETQQAM. The resulting Ir hydrosols were oxidized on the virus using 0.2 % hydrogen peroxide. To co-immobilize IrO_2 and ZnDPEG on the virus, aqueous sodium hexachloroiridate was hydrolyzed with citrate as a ligand and self-assembled into IrO_2-ZnDPEG core-shell nanowires through their incubation with the ZnDPEG-conjugated M13 viruses at room temperature (Figure 3-11).

Horseradish peroxidase (HRP) catalyses the oxidation of a wide variety of substrates by H_2O_2, and scopoletin (7-OH-6 methoxycoumarin) can act as a reducing substrate for HRP while losing its fluorescence. The HRP-scopoletin assay based on this reaction scheme was used to determine the residual H_2O_2 in the IrO_2 samples used in this study. Scopletin (10 μM, Sigma Aldrich) was prepared in 0.5 M PBS (pH 7.0), and 5.5 nM HRP (Sigma Aldrich) in 50 mM PBS (pH 7.0). Samples (0.5 mL) were mixed with 1 mL scopoletin and 1 mL HRP in the dark at room temperature. The fluorescence emission intensity was determined at 460 nm with excitation at 350 nm. The calculated residual amount of H_2O_2 in the IrO_2 samples examined was in the range of 0.6 $\sim$ 2.0 μmoles.

The color of the IrO_2-ZnDPEG core-shell nanowires was dark green, while those of ZnDPEG and IrO_2 nanowires were red and blue, respectively (Figure 3-12). The IrO_2 shell thickness of the IrO_2-ZnDPEG nanowires was controlled by varying the amount of hydrated Ir clusters while fixing the number of ZnDPEG-conjugated viruses for mineralization. The IrO_2:ZnDPEG ratio, denoted by **r**, was determined by ICP-AES analysis for Ir and Zn. Below are shown the TEM images of the ZnDPEG-conjugated M13 viruses (Figure 3-13) and the IrO_2-ZnDPEG nanowires with different IrO_2 shell thicknesses, $\mathbf{r} = 15$ (Figure 3-14) and $\mathbf{r} = 224$ (Figure 3-15).

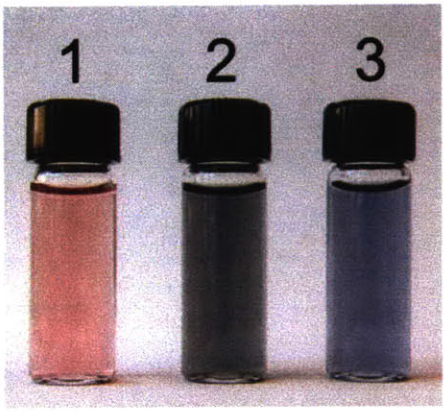

Figure 3-12: Digital camera images of aqueous solutions of ZnDPEG (1), IrO_2-ZnDPEG nanowires (2), and IrO_2 nanowires (3).

3.6 Oxygen Evolution Analyses

For the oxygen evolution studies, sodium borate was used as a proton acceptor and sodium persulfate was used as a sacrificial electron acceptor. To continuously monitor the photochemical oxygen evolution, a custom-maded oxygen analysis system was set up as described in Figure 3-16.[3] The sample solution was illuminated with a 300 W xenon light source (Perkin Elmer, DiX1765) through a long wavelength pass filter ($>$ 400 nm, Thorlabs Inc., Newton, NJ) while purged with N_2 (99.999%, Airgas)

[3]This oxygen analyzer set-up was devised and maintained by Andrew P. Magyar.

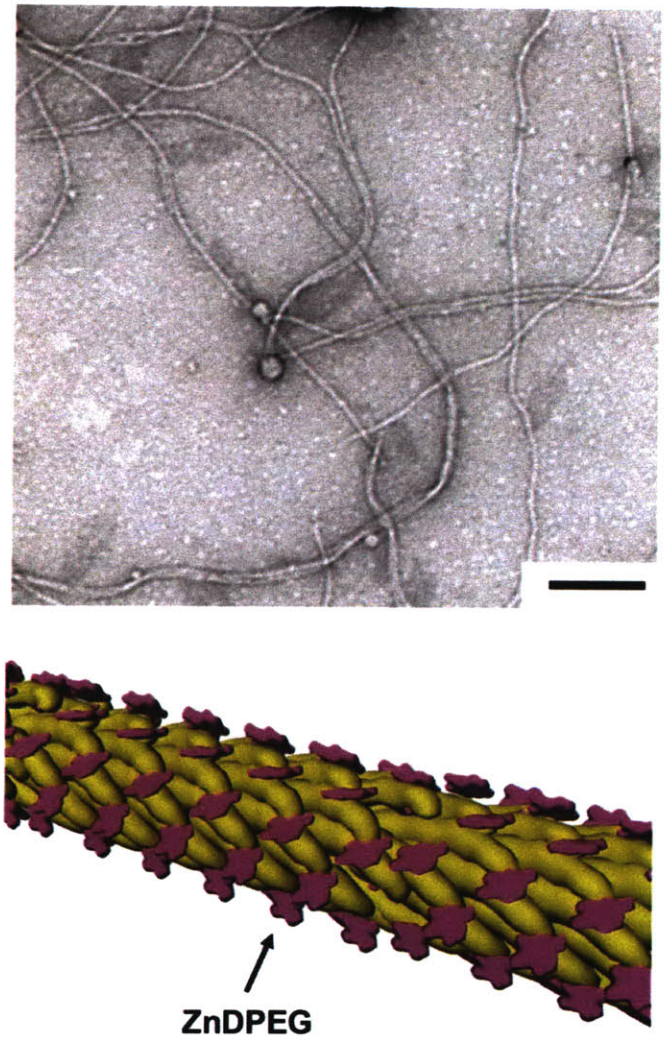

Figure 3-13: **Transmission electron micrograph of ZnDPEG nanoantennas** after negative staining. Scale bar = 200 nm. Below the electron micrograph the schematic structure is drawn using PDB structure 2C0W.

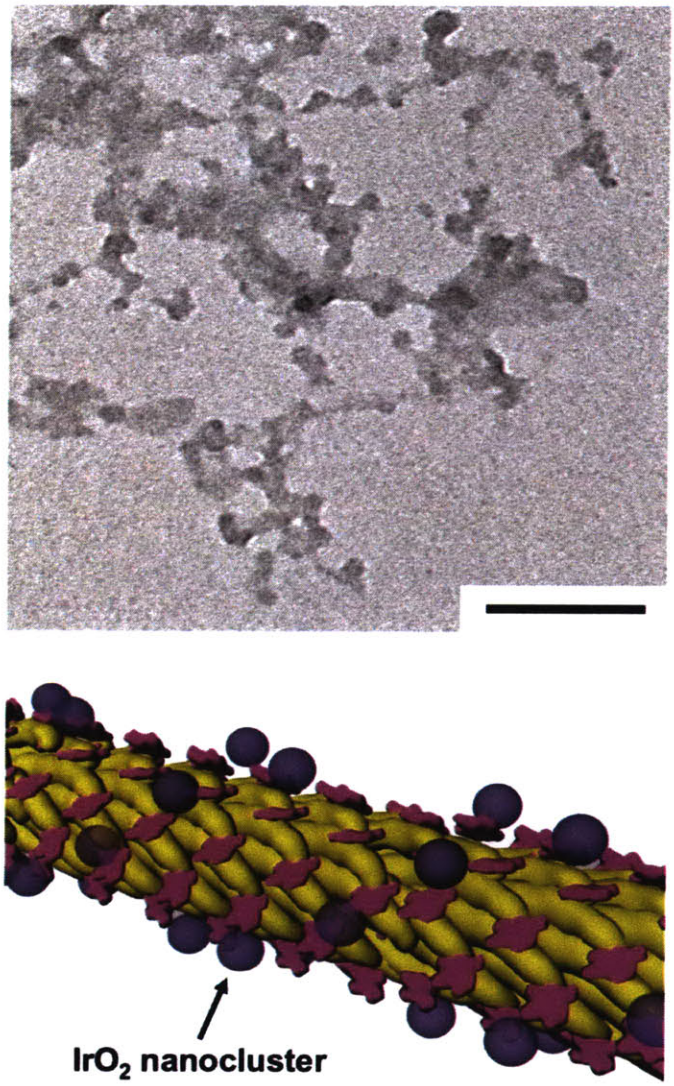

Figure 3-14: **Transmission electron micrograph of IrO_2-ZnDPEG hybrid nanowires** at the IrO_2:ZnDPEG molar ratio, r = 15. Scale bar = 200 nm. Below the electron micrograph the schematic structure is drawn using PDB structure 2C0W.

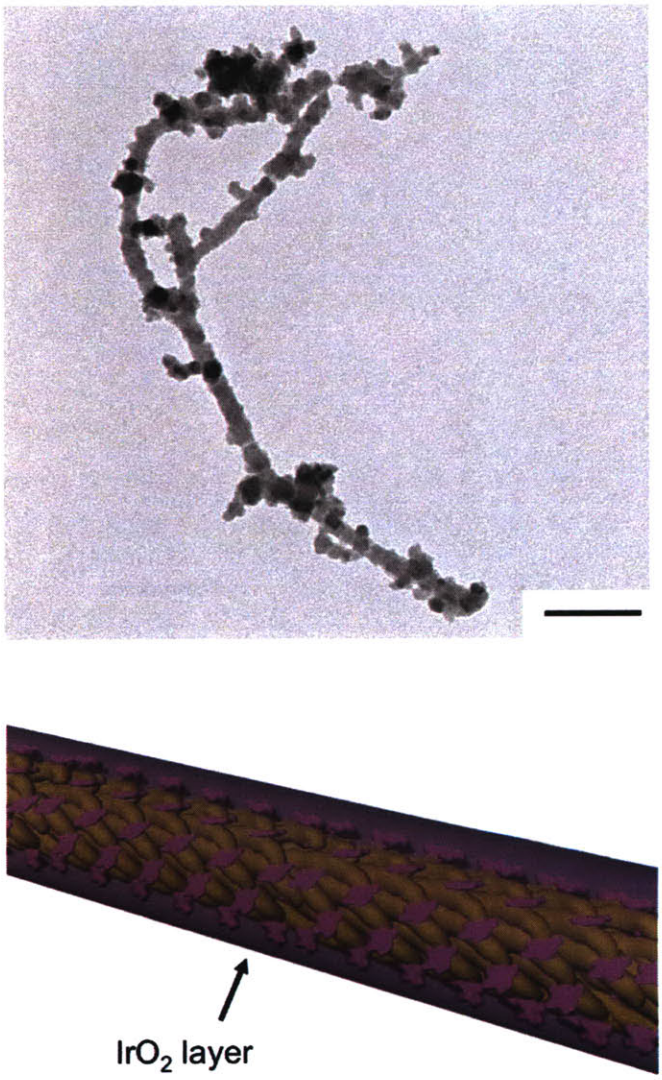

Figure 3-15: **Transmission electron micrograph of IrO_2-ZnDPEG hybrid nanowires** at the IrO_2:ZnDPEG molar ratio, r = 224. Scale bar = 200 nm. Below the electron micrograph the schematic structure is drawn using PDB structure 2C0W.

as a carrier gas. The carrier gas was then flowed through a Nafion PD gas dryer (Perma Pure, Toms River, NJ) at 0.2 mL s^{-1}, and the oxygen concentration was continuously monitored using a ZrO_2-based gas analyser (ZrO 2000, Alpha Omega Instruments Corp, Cumberland, RI). The pH of sodium borate ($Na_2B_4O_7 \cdot 10H_2O$, 6.6 mM) was adjusted to 11 using 1.0 N NaOH. Sodium persulphate solution ($Na_2S_2O_8$, 27 mM) was freshly prepared for oxygen evolution experiments.

IrO_2 hydrosol clusters (32.7 μM) dispersed with unconjugated ZnDPEG (8 μM) at pH 11 exhibited a turnover number (TON), the total number of water molecules the catalyst splits, of about 179 (4 times the amount of O_2 evolved per Ir) (Figure 3-17A). Their turnover rate (TOR), the number of water molecules the catalyst splits per unit time per surface active site, was about 0.076 s^{-1}. This TOR was calculated from the steady state oxygen evolution rate with an assumption that 53 % of the total Ir atoms is exposed to the catalysts surface. These values are comparable to the previously reported data from IrO_2 nanoparticles with different photosensitisers. However, IrO_2 nanowires mixed with unconjugated ZnDPEGs revealed TON $\approx$ 76, only 44 % of those of the IrO_2 hydrosol clusters. This reduced TON seems to be attributed to the smaller surface area per mass (231.5 m^2 g^{-1}) compared to IrO_2 hydrosol clusters. As expected, their TOR ($\approx$ 0.069 s^{-1}) was similar to that of the IrO_2 hydrosol clusters. Astoundingly, even despite the small surface area, IrO_2-ZnDPEG nanowires assembled through the formation of an IrO_2 shell on the ZnDPEG-conjugated M13 core exhibit dramatically higher water splitting activities: TOR $\approx$ 0.85 s^{-1} and TON $\approx$ 796. This high activity seems to be a synergistic effect of the excitonic migration between photosensitisers and the close arrangement of photosensitisers with IrO_2. To determine the effects of the energy transfer on the oxygen evolution, we tested IrO_2 hydrosol clusters with ZnDPEG-conjugated M13, showing TOR $\approx$ 0.35 s^{-1} and TON $\approx$ 313 (Figure 3-17A). Both of these values were significantly higher than those of IrO_2 hydrosol clusters with unconjuated ZnDPEG. Moreover, the IrO_2 shell thickness

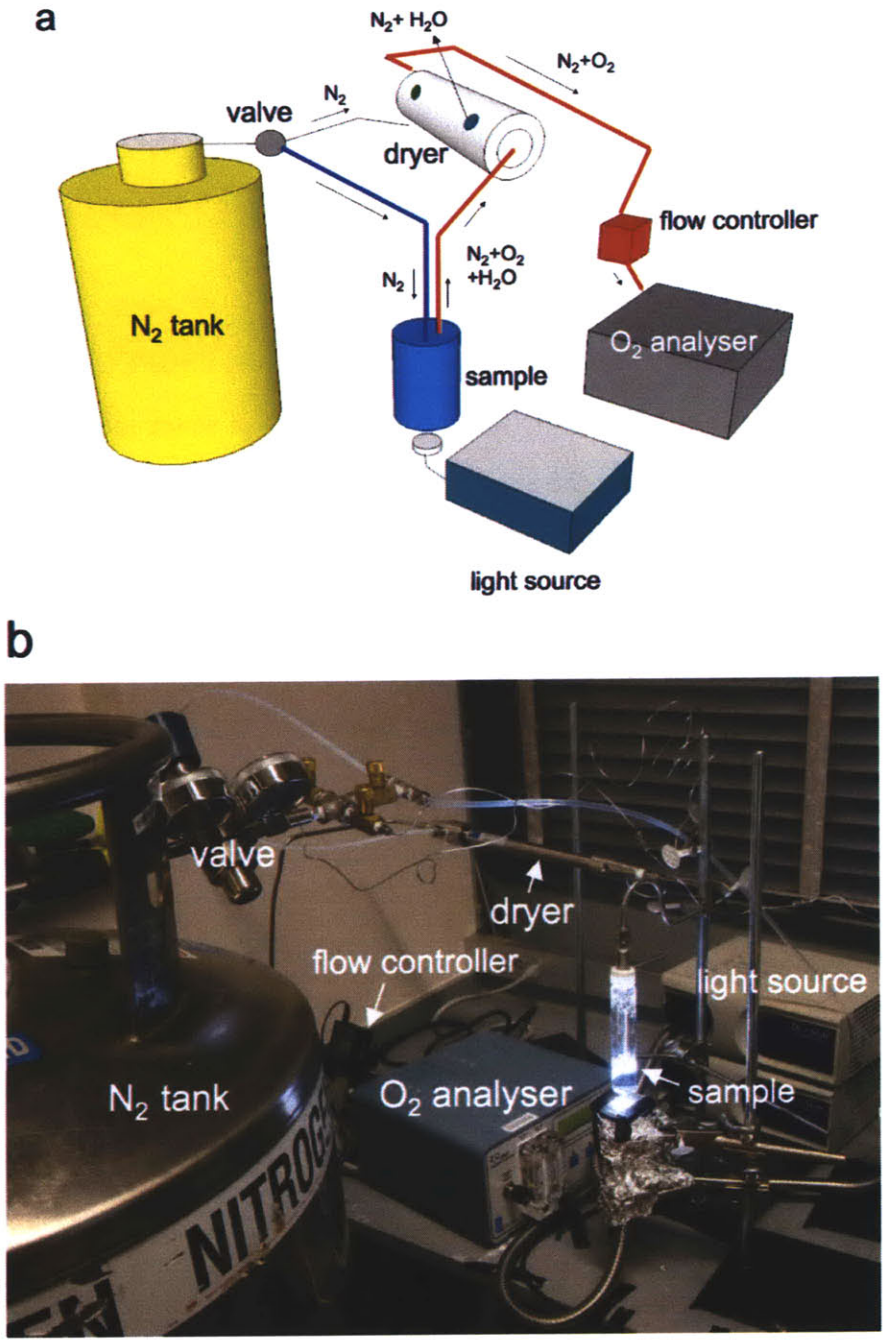

Figure 3-16: **Schematic description (A) and photograph (B) of the experimental set-up for real-time oxygen analysis.** During the experiments, the sample was completely covered with a brown paper cylinder that does not allow the ambient light penetration.

turned out to be a critically important parameter for the water oxidation activity, as shown in Figure 3-17B. Both TON and TOR increased with decreasing r with the highest TON $\approx$ 1,143 and TOR $\approx$ 1.57 s^{-1} at r = 15, which are about 3.5 times larger than the highest values reported for light-driven water oxidation. This fast steady-state reaction kinetics of the IrO_2-ZnDPEG nanowires indicates that appropriate co-assembly of catalysts with photosensitisers is critically important for light-driven water oxidation.

3.7 Regeneration of Catalytic Materials Using Microgels

Photochemical colloidal catalysts are prone to aggregation, and this structural instability limits their practical applications. For instance, the IrO_2-ZnDPEG nanowires showed spontaneous precipitation after an oxygen evolution experiment (Figure 3-18).

To solve this problem, porous microgels were employed as an immobilization matrix for M13 viruses and IrO_2-ZnDPEG nanostructures were synthesized within the microgels. This immobilization strategy was inspired by the structure of the chloroplast, which mechanically supports thylakoid membranes and thus allows the photosynthetic systems to maintain their structural integrity (Figure 3-19).

Using a microfluidic technique (Figure 3-20A), monodisperse aqueous droplets incorporating the viruses and acrylic monomers were generated and subsequently converted to microgels (Figure 3-20B) by initiating polymerization under ultraviolet irradiation. A flow focusing glass capillary device consisting of a tapered cylindrical collection tube having an orifice 150 μm in diameter fitted in a square capillary was fabricated in order to produce monodisperse microgels. Two immiscible fluids were infused into the device from opposite sides of the square capillary. The outer fluid (white mineral oil with 3 wt% Abil® EM90, Degussa) focuses the inner

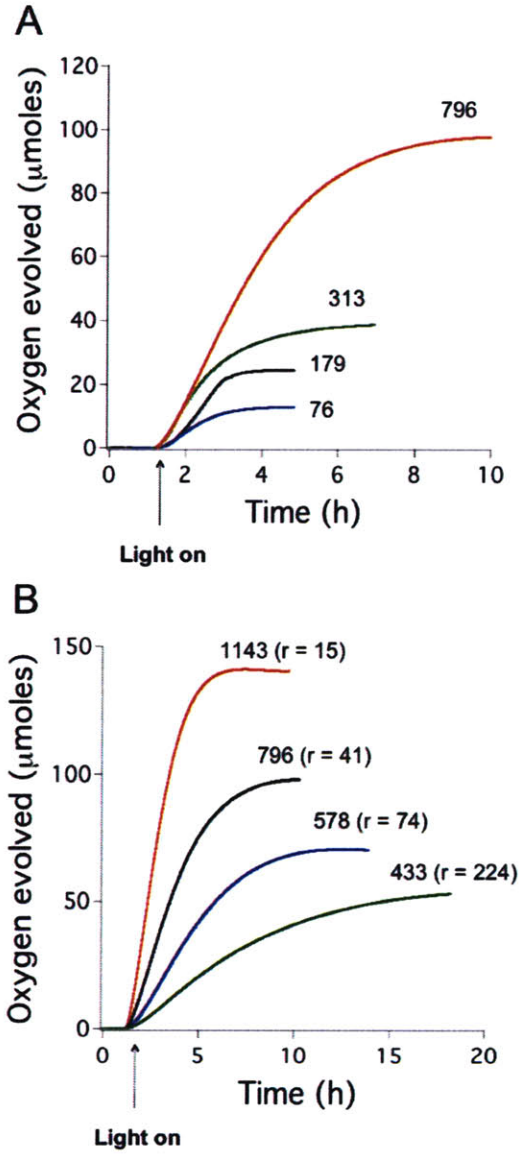

Figure 3-17: **Oxygen evolution from IrO_2-ZnDPEG nanowires.** **A**, Time-course oxygen production profiles for IrO_2 hydrosol clusters mixed with unconjugated ZnDPEG (black), IrO_2 hydrosol clusters mixed with ZnDPEG-conjugated viruses (blue), virus-templated IrO_2 nanowires mixed with unconjugated ZnDPEG (green), and IrO_2-ZnDPEG hybrid nanowires (red). The concentrations of IrO_2 and ZnDPEG were fixed at 32.7 mM and 0.8 mM, respectively. **B**, Time-course oxygen production profiles for IrO_2-ZnDPEG hybrid nanowires having different ratios of IrO_2 to ZnDPEG, r = 15 (red), 41 (black), 74 (blue), and 224 (green). The numbers above the curves indicate TON.

Figure 3-18: **Photographs of the virus-templated IrO_2 nanowires** suspended in 6.6 mM sodium borate before (1) and after (2) the oxygen evolution experiment for 10 h.

fluid (aqueous mixture of acrylamides, bisacrylamides, 2-hydroxyl-2-methyl-1-phenyl-1-propanone (Darocur 1173) and viruses) into the orifice of the collection tube and breaks the inner fluid into monodisperse droplets. Collected emulsions are converted to microgels by initiating polymerization using ultraviolet irradiation (365 nm, 3W). Polyacrylamide was used as a matrix material because of its well-known compatibility with biological molecules, controllable porous structures, and high proton conductivities. The encapsulated viruses were homogeneously distributed within the microgels without any phase segregation as confirmed by fluorescent labeling (inset in Figure 3-20B). Viruses encapsulated in microgels were subsequently used as templates for assembling IrO_2 hydrosol clusters and photosensitisers. ZnDPEG was covalently attached to viruses in the microgel by pre-activating carboxylic acids groups of ZnDPEG with carbodiimides. After rigorous rinsing with water to remove loosely bound ZnDPEG, IrO_2 clusters were assembled on the viruses in situ by diffusion of hydrated Ir precursors into the microgels followed by chemical oxidation. Energy dispersive X-ray (EDX) analysis with scanning electron microscopy indicated the homogeneous distribution of Ir elements in the microgels (Figure 3-20C and D).

Two different IrO_2-ZnDPEG microgels were prepared having r = 35 and 109, as determined by ICP-AES analysis. As observed in the IrO_2-ZnDPEG nanowires, signif-

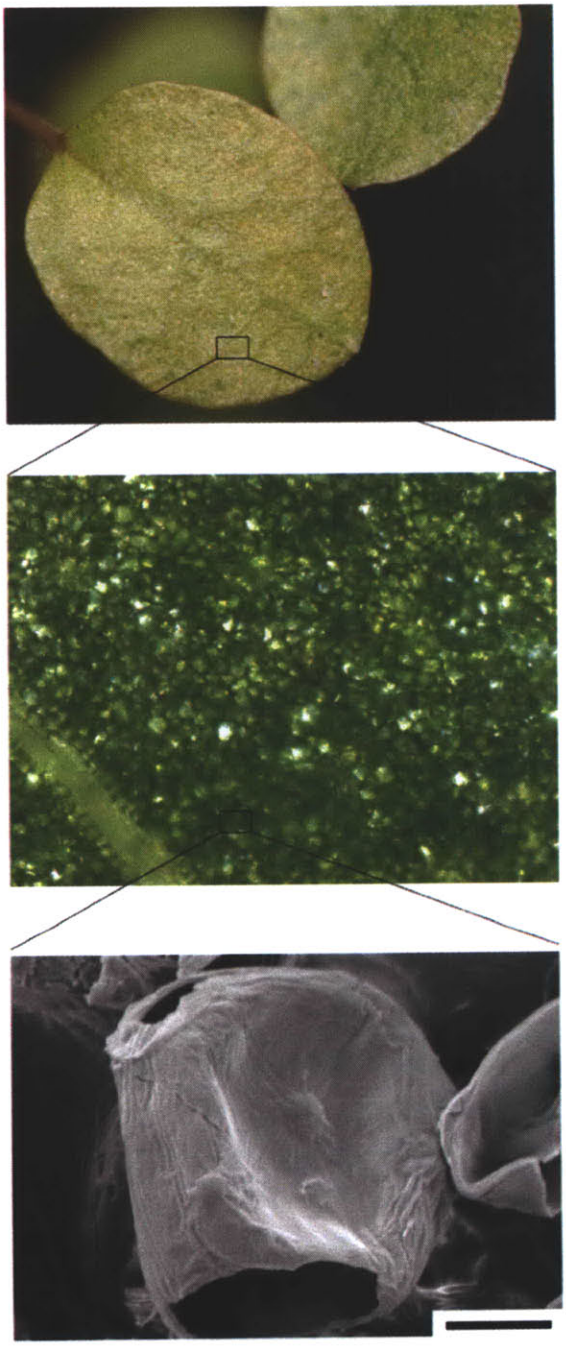

Figure 3-19: **Multiscale structures of a leaf**: a photographic image of a leaf (top), an optical microscopic image of chloroplasts (middle), and scanning electron microscopy (SEM) image of a chloroplast (bottom). Scale bar = 50 μm.

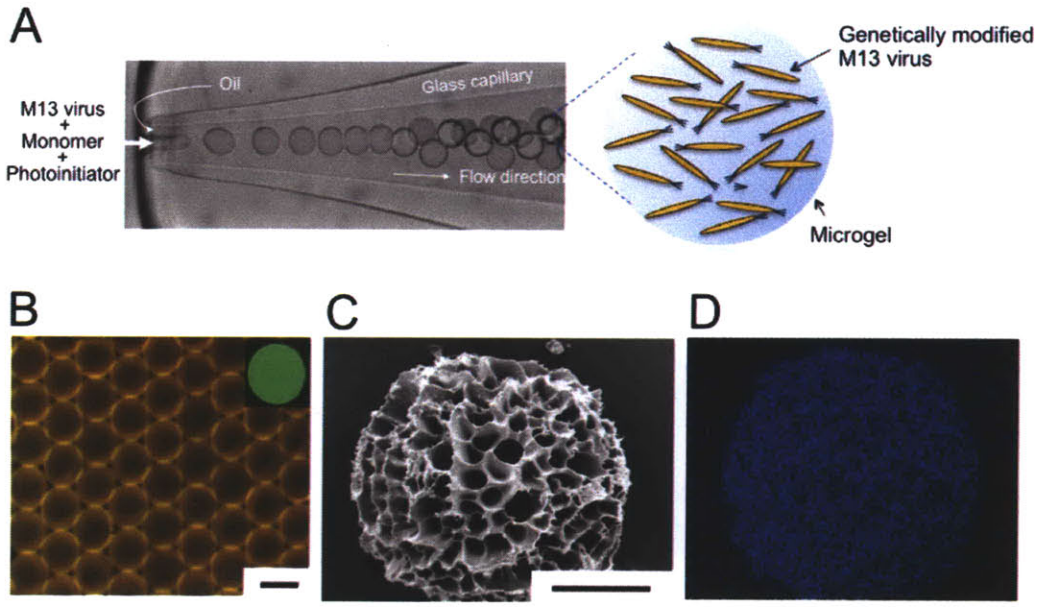

Figure 3-20: **Fabrication of virus-loaded polymer microgels. A**, The injection part of the glass capillary device for fabrication of the virus-loaded microgels. **B**, The monodisperse virus-loaded microgels prepared from the microfluidic device. Scale bar = 100 μm. **C, D**, SEM image (**C**) and elemental map (**D**) of the freeze-dried microgel containing IrO_2-ZnDPEG nanostructures. Iridium is represented by blue dots.

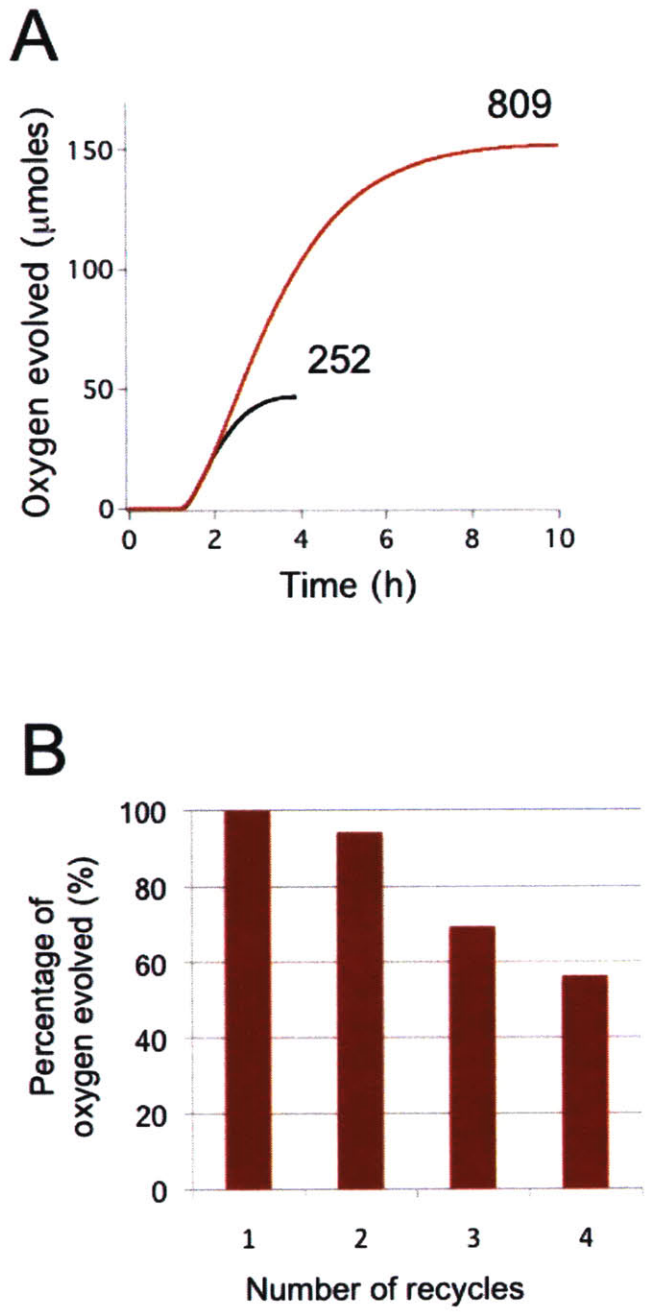

Figure 3-21: **Oxygen evolution profiles from IrO_2-ZnDPEG microgels A**, Oxygen evolution profiles from IrO_2-ZnDPEG microgels having r = 35 (black) and 109 (red). The numbers above the curves indicate TON. **B**, Recycling efficiency of IrO_2-ZnDPEG microgels.

icantly more oxygen evolved from microgels having the lower IrO_2:ZnDPEG ratio, as shown in Figure 3-21A. To demonstrate the recycling capability of the microgel-based system, the oxygen evolution from the microgels was halted at 90 min post illumination. The microgels were then collected through centrifugation and re-suspended in 0.2 % hydrogen peroxide to re-oxidize the catalyst. The regenerated microgels showed about 94 % oxygen evolution compared to the TON in the first cycle, and the value decreased to 56 % in the fourth cycle (Figure 3-21B). As a result, the cumulative TON after 4 reaction cycles became 1.58 times higher than the TON of the full single reaction.

3.8 Conclusion

The oxygen evolution results from the microgel-based system demonstrated for the first time the recycling capability of a light-driven water oxidation system. However, deterioration of the catalytic activity was consistently observed, presumably because of the photochemical degradation of the photosensitizers attached to the virus. To improve the chemical stability of the system, further optimizing both of the materials properties and the reactor design was attempted, as will be discussed later in this dissertation. For instance, despite their high initial performance, the sacrificial electron acceptors used in this study may produce hydroxyl radicals, which seem to facilitate the degradation of catalytic materials. Their replacement with appropriate non-sacrificial materials or the coupling of the current system to a hydrogen evolving catalyst may also reduce certain corrosive processes. In addition, the biomimetic approach was expanded to cobalt oxide (Co_3O_4) catalysts, which were shown to assemble on M13 viruses expressing the peptide tetraglutamate. The synthesis and application of virus-templated cobalt oxide nanowires to photochemical water oxidation will be discussed in the following chapters. It is expected that, for a broad range of catalysts,

multiscale architecture combining a virus-based nanostructure with porous hydrogels could eventually offer a biomimetic platform for artificial photosynthesis that allows the efficient, sustained production of clean fuels from sunlight.

Chapter 4

Genetically Programmed Microgels for Biomineralization

This chapter describes the combination of multiple building blocks - polymer microgels as macroscopic scaffolds and M13 viruses as nano-scale templates for biomineralization. Microgels provide a three dimensional hydrogel network that physically or chemically immobilizes the genetically engineered viruses, which can evolve into nanostructured inorganic materials through site-directed biomineralization in situ. The resulting organic-inorganic hybrid materials may find promising applications in diagnostics, biosensors, medical implants (e.g., emboli), organic synthesis, chemical and biological separation, catalysis, and optical devices.

4.1 Introduction

Over millions of years of evolution, nature has created a myriad of functional materials having elaborate nanostructures within living organisms. Particularly, hard structures (*e.g.*, bone, corals, ivory, enamel, oyster shells) consist of minerals which are closely associated with an organic phase. These biological composite materials are typically formed through a crystallization process of inorganic materials within

organic scaffolds, called 'biomineralization' [83, 84, 82, 81]. Biominerals have hierarchical structures on many length- and timescales, which are often very unique and not achievable in a typical manufacturing process. For example, bone has a complex structure that can be considered on a hierarchy of at least seven separate scales. This broad range of structural dimension requires theories ranging from quantum mechanics and atomistic simulation to continuum mechanics and theories of composites depending on the scale that one is working at. In addition, biomineralization involves nucleation processes, the timescale may be of the order of seconds or more, the following growth may involve a multi-stage process of self-assembly of complex nanoscale units.

Our understanding of the fundamental design principles that nature uses can provide new techniques to engineer novel functional materials and devices. In particular, for industrial applications, this approach inspires 'green chemistry' research by offering environmentally benign synthesis routes for building complex, nanostructured materials [108]. Employing nature's strategies we can make use of aqueous processes at low operating temperatures. Furthermore, a template-mediated precursor technique can extend the approach to final materials that are themselves insoluble in water.

There are countless parameters that can affect physicochemical properties of biominerals, including size, shape, orientation, polymorphic structure, and defect texture. Through rational design and synthesis of novel functional nano-materials via biologically inspired techniques, there is tremendous opportunity to develop bulk materials with desirable properties, even the ones that do not exist in nature. Our intervention can reach fundamental levels of this biological processes using genetic engineering methods. Various natural and genetically engineered biological materials, such as nucleic acids, proteins, viruses and cells, have been studied as a template for synthesis of inorganic materials. It has been demonstrated that the M13 virus

is a particularly attractive building block for arranging nanocrystals, building liquid crystals, and templating nanowires. Combinatory phage-display libraries have been used to select peptides that can selectively bind to a broad range of materials, such as GaAs, InP, Si, ZnS, CdS, Au, and streptavidin. Various interesting nanostructures have been suggested by using the engineered viruses carrying these peptides, including virus 'nanorings', gold nanowire blocks, and nanowire monolayers [55, 73, 74, 75, 86, 85, 96, 97, 95].

For applications to macroscopic devices, nano-scale materials need to be further processed to build larger length scale structures [12]. For instance, it was shown that the viruses can be organized into unique two-dimensional ordered structures in a polyelectrolyte multilayer while displaying a variety of binding motif peptides to the surface layer. Such genetically controlled surface functionalization was successfully employed to the development of a thin anodic electrode for lithium ion batteries. However, little has been reported regarding biological mineralization of three-dimensional macroscopic structures incorporating sophisticated nano-scale structures because it is very challenging to control multiple interactions over different orders of length scale using a single scaffold material. Microgels provide a 3D hydrogel network that physically or chemically immobilizes the viral templates. The viruses can evolve into nanostructured inorganic materials through site-directed biomineralization in situ, while the overall dimension of the final structure is determined by the size and geometry of the microgels.

Micron-scale polymer particles are typically prepared by mechanically dispersing monomers or polymers into an immiscible phase, followed by polymerization or solidification of the dispersed droplets. Metastable small emulsion droplets are transiently generated and merged through coarsening processes, such as Ostwald ripening and coalescence. When biological molecules are encapsulated during the droplet formation, they are exposed to a large number of the oil-water interfaces, leading to their ad-

sorption at the interface. This adsorption often induces their conformational changes and even irreversible inactivation. The structural integrity of biological templates is essential for site-directed mineralization as it is mediated by the specific interactions between metal ions and biological binding motifs. Thus, such structural alternation of the incorporated biological molecules must be avoided for efficient biomineralization.

To overcome such structural instability problem, we here report a microfluidic fabrication method to prepare monodisperse polymer microgels incorporating genetically modified M13 viral templates. Our recent works demonstrated that microfluidic techniques can be employed for fabricating polymer microgels with facile controlling their size and geometry. We expect that this approach could also be advantageous for maintaining the physical stability of the incorporated bio-molecules because they generate only a small fluctuation of the interface in a laminar flow, which can minimize the contact of biological molecules to water-oil interfaces during microgel preparation.

4.2 Genetically Modified M13 Viruses

Three different genetically engineered viruses were prepared through either phage library-based biopanning or site-directed mutagenesis. The M13KE viral DNA vector (New England Biolabs, Ipswich, MA) was modified; *PstI* and *BamHI* sites were inserted to the 5' end of gp8, encoding pVIII coat proteins, while *PstI* in the $lacZ\alpha$ was silently mutated by overlap extension polymerase chain reaction. This modified viral vector was named the M13SK (Figure 4-1). A type 8 phage library was constructed through the ligation of oligonucleotide duplexes encoding $107 \sim 108$ random peptides to gp8 in the M13SK using *PstI* and *BamHI*. Two binding peptide motifs, AGETQQAM for IrO_2 and VSGSSPDS for gold (Au), were identified from three-around biopanning against Ir(IV)O_2 powders (99.9%, Aldrich) and a Au thin film, respectively. The oligonucleotide duplex encoding tetraglutamate (EEEE or E4), in-

stead of the randomized sequences, was directly ligated to pVIII to prepare negatively charged viruses as a binder peptide for metal ions.[1] It is well known that glutamate and other charged amino acids can mediate the binding of metal ion precursors to natural proteins presumably via electrostatic interactions and have been employed to organic templates for biomineralization.

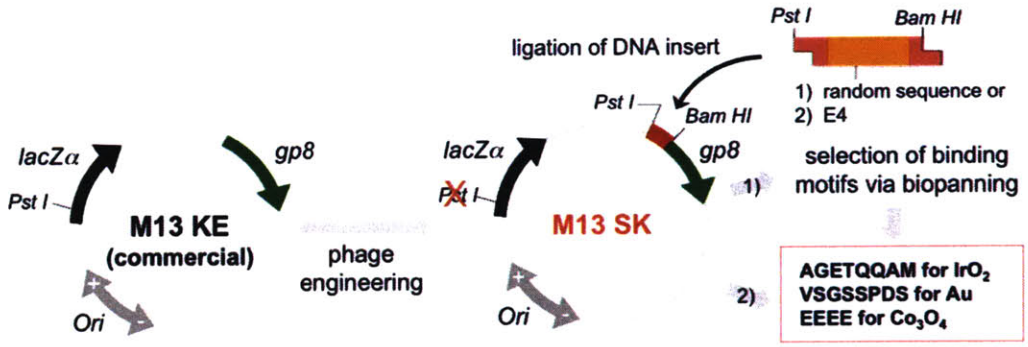

Figure 4-1: **The M13SK viral vector** was constructed by modifying M13KE through the silent mutation of *PstI* in the *lacZα* and the insertion of *PstI* and *BamHI* restriction sites to the 5' end of gp8. The phage library was designed and constructred by Soo Kwan Lee.

4.3 Encapsulation by a Conventional Emulsification Technique

We began by preparing virus-loaded microgels using a simple water-in-oil emulsification method: aqueous droplets were dispersed in the continuous oil phase containing emulsifiers and then were solidified by polymerization. An aqueous mixture included 20 parts of M13 viruses (10^{10} pfu μL^{-1} in deionized water), 20 parts of acrylamide (Sigma-Aldrich) as a monomer, 2 parts of bis-acrylamide (Sigma-Aldrich) as a cross-linker and 1 part of 2-hydroxy-2-methyl-1-phenyl-1-propanone (Darocur

[1]Later it was found that the E4 viruses had a single point mutation of E to A in the third position: that is, they have EEAE rather than EEEE

1173^{TM}, Ciba, Basel, Switzerland) as a photo-initiator. Simple water-in-oil emulsions were prepared by emulsifying the above aqueous solution (2 mL) in white light mineral oil (40 mL, Sigma-Aldrich) containing 5 wt% Degussa Abil EM90^{TM} (cetyl PEG/PPG-10/1 dimethicone, Evonik Goldschmidt GmbH, Germany) as an emulsifier with homogenization at 3,000 rpm for 2 min, followed by further homogenization at 2,000 rpm for 30 min while exposed to the ultraviolet light (3W, $\lambda_{max} = 365$ nm). To remove large agglomerates, the microgel suspension was filtered through a 300 μm sieve. Small microgels were also eliminated by repeatedly harvesting larger particles following sedimentation. Despite the post size selection processes, the resulting microgels exhibited a very wide size distribution (Figure 4-2A). Biomineralization of IrO_2 (the detailed procedures are described below) resulted in highly irregular structures with heterogeneous distribution of IrO_2 as indicated by bluish colors (Figure 4-2B). Presumably, the viruses lost their intact structure as they were continuously exposed to the oil-water interface during the emulsification. The integrity of the viral structure is critically important for directed biomineralization, which is driven by the binding of metal ions coordinated by specific peptide binding motifs expressed to a viral surface.

4.4 Capillary Microfluidic Approach for Encapsulating M13 within Microgels

To overcome this instability problem, we prepared PAAm microgels incorporating M13 viruses using a glass capillary microfluidic technique. The capillary microfluidic device consists of a tapered cylindrical internal injection tube within a square external collection tube (Figure 4-3A and B). In the region near the exit of the internal tube, the outer fluid focuses the inner fluid through the collection tube to form a fluid thread that eventually breaks into drops as a result of hydrodynamic

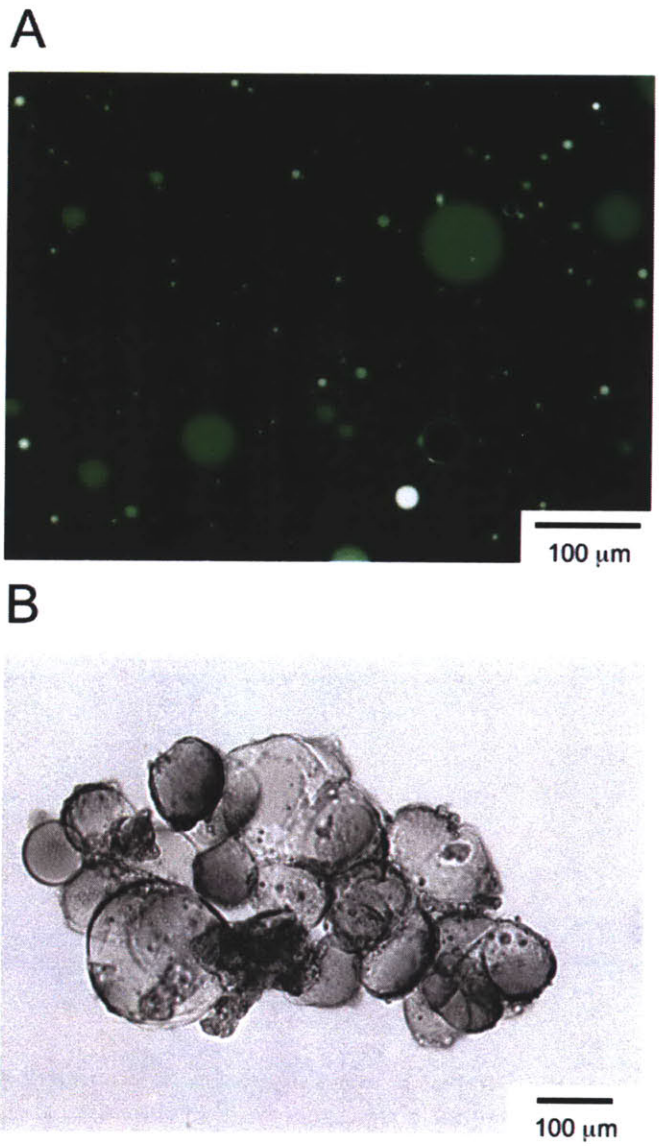

Figure 4-2: **Virus-loaded microgels prepared using a water-in-oil emulsification.** **A**, Fluorescence micrograph of the virus-loaded PAAm microgels prepared by a simple water-in-oil emulsification method. **B**, Optical micrograph of the PAAm microgels after IrO_2 mineralization.

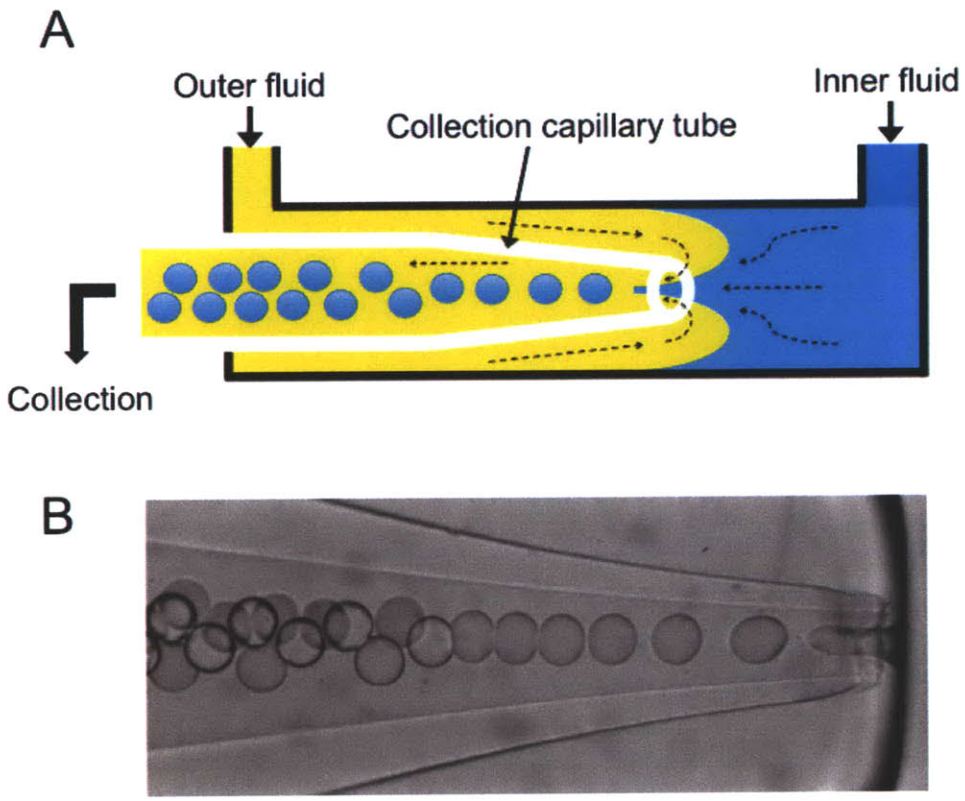

Figure 4-3: **Fabrication procedures for microgels incorporating genetically engineered M13 viruses. A**, Schematic representation of the coaxial glass capillary microfluidic device. **B**, Optical micrograph of pre-microgel droplet production.

instabilities. An aqueous mixture was used as the internal phase fluid, including M13 viruses, acrylamide, bis-acrylamide and Darocur 1173^{TM}. A white light mineral oil was used as the continuous phase. The polymerization was initiated by exposing the embryonic microgel droplets to ultraviolet light immediately after they were formed. The size of the prepared monodisperse microgels was typically about 100 μm in diameter (Figure 4-4) although it could be further modulated by controlling several experimental parameters as demonstrated previously. The homogeneous distribution of the viruses within the microgels was confirmed through labeling the incorporated viruses with fluorescein isothiocyanate (FITC). To demonstrate the validity of the virus-incorporating microgels as genetically programmed platforms for biomineralization, three different viruses were incorporated into the polymer networks during the formation of the microgels. Virus-templated inorganic nanostructures were then self-assembled through diffusion of metal ions into the microgels, followed by chemical oxidation or reduction.

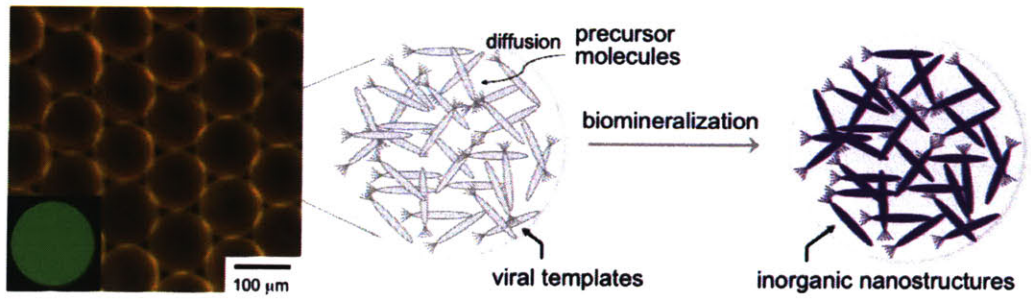

Figure 4-4: **Bright-field micrograph** of virus-loaded PAAm microgels in water (insert: fluorescence image of a microgel labeled with FITC) and schematic description of the biomineralization process using PAAm microgels incorporated with genetically modified M13 viral templates.

4.4.1 Biomineralization of IrO_2 Nanostructures within Microgels

IrO_2 nanostructures were self-assembled through the incubation of IrO_2 nanoclusters with PAAm microgels incorporated with the AGETQQAM-expressing M13 viruses (denoted AG-gels). Microgels loaded with wild type M13KE viruses (denoted KE-gels) were used as controls for biomineralization. To synthesize aqueous IrO2 nanoclusters, an aqueous mixture of sodium hexachloroiridate (1.5 mM, $Na_2IrCl_6 \cdot 6H_2O$, Alfa Aesar) and sodium citrate (4.8 mM) were incubated at 90°C for 4 h followed by stirring with 20 g ion exchange resin (Monobed MB1, Sigma-Aldrich) for 30 min to remove the unbound citrates. The hydrolyzed Ir compounds were chemically oxidized to IrO_2 nanoclusters with 2.5 nm in diameter using 0.2 % hydrogen peroxide. The formation of IrO_2 nanoclusters was indicated by the appearance of deep blue color with a characteristic absorption peak around 580 nm.

Approximately 10^4 virus-loaded microgels (KE-gels and AG-gels) were soaked in 2 ml fresh solution of IrO_2 nanoclusters (51.3 mg L^{-1}) at room temperature for 24 h with orbital shaking at 200 rpm. The photographs of the microgels and the supernatants showed the significantly higher IrO_2 uptake into AG-gels compared to KE-gels (Figure 4-5A). Inductively coupled plasma-atomic emission spectroscopy (ICP-AES) analysis indicated that 9.7 ng IrO_2 was formed per microgel, indicating that about 95 % of the initial IrO_2 nanoclusters was taken up by AG-gels. In contrast, KE-gels exhibited only an about 20 % uptake efficiency. These results clearly demonstrated that the microfluidic technique provides a great value for the encapsulation of virus templates into polymer microgels as the functional structures of the virus were maintained during the microgel fabrication. The homogeneous distribution of IrO_2 within AG-gels was shown using scanning electron microscopy (SEM, Figure 4-6A) with energy dispersive X-ray (EDX) analysis (Figure 4-6B and C) of the freeze-dried microgels. To further analyze the morphology of the IrO_2 nanostructures generated within AG-

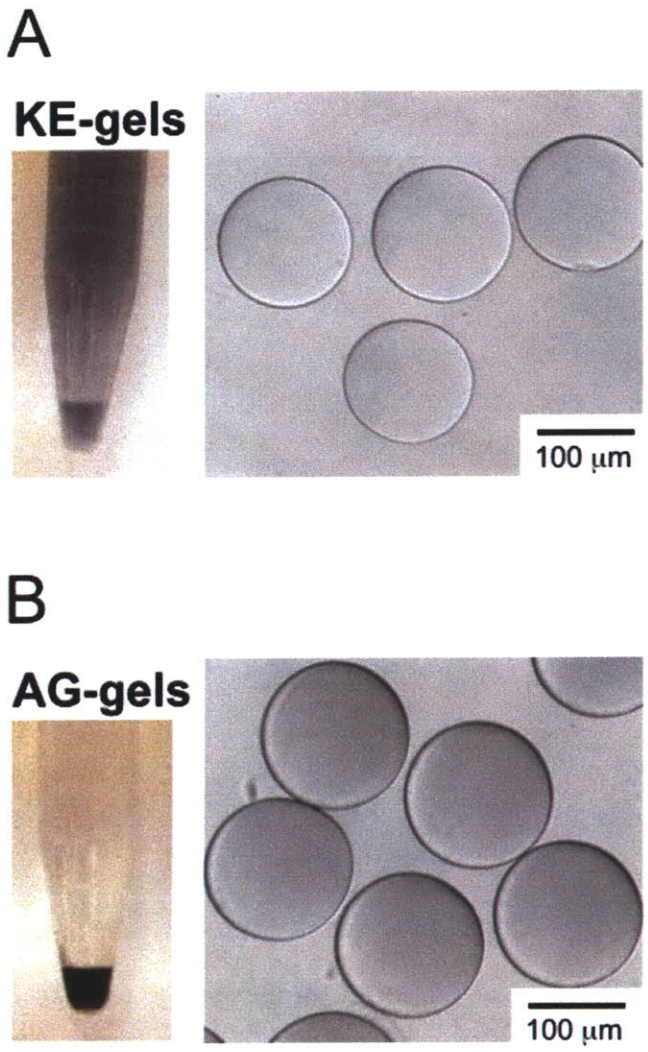

Figure 4-5: **Biomineralization of IrO_2 nanostructures within microgels.** KE-gels (A) and AG-gels (B) mixed with aqueous IrO_2 nanoclusters with optical micrographs of the microgels.

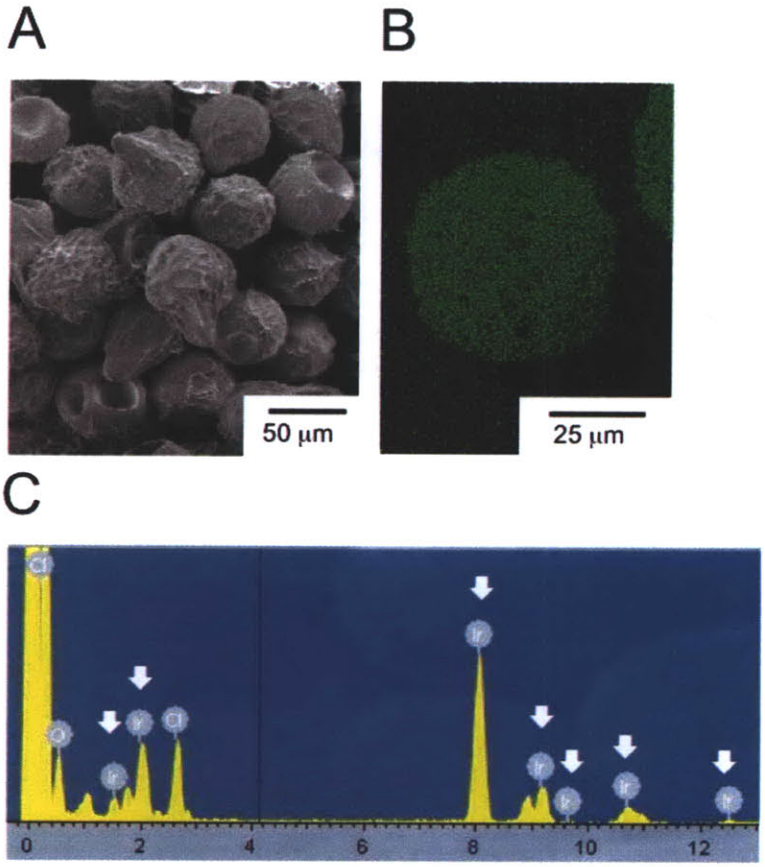

Figure 4-6: **Scanning electron micrograph and elemental map of IrO_2 nanostructures within microgels.** SEM image (A), elemental map (B), and EDX spectrum (C) of the freeze-dried AG-gels post IrO_2 mineralization. Ir elements were represented as green dots in (B).

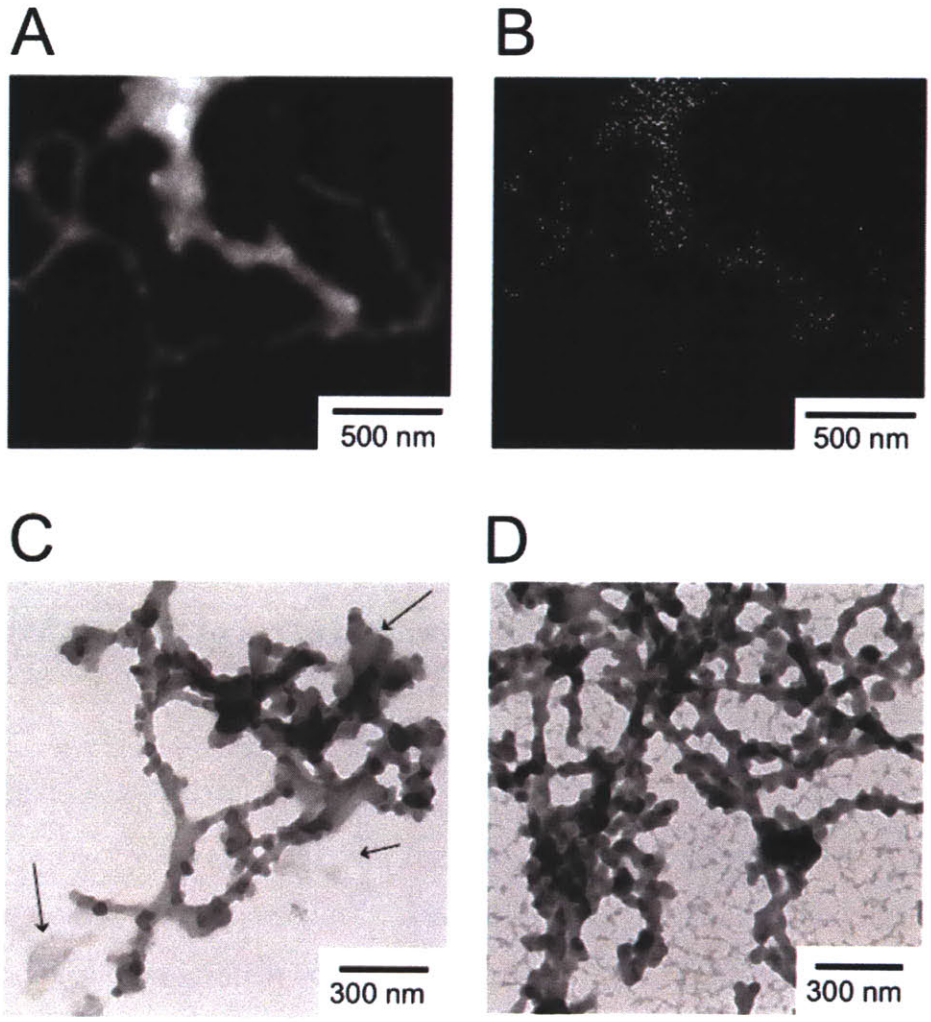

Figure 4-7: **Transmission electron micrograph of IrO_2 nanostructures within microgels.** Dark-field STEM image (A), elemental map (B), and TEM image (C) of IrO_2 nanostructures extracted from AG-gels. Ir elements were represented as white dots in (B). Arrows indicate the microgel debris. (D) TEM image of IrO_2 nanostructures assembled on the AGETQQAM-expressing M13 viruses in a bulk aqueous solution.

gels, the dried microgels were physically disrupted by shearing them between two silicon wafer plates. To extract the IrO_2 nanostructures, the disrupted debris were incubated in deionized water for 2 days with orbital shaking at 300 rpm. The solution was briefly centrifuged at 1,500 × g for 30 s to induce the sedimentation of large debris, and a drop of the supernatant was placed on a carbon-coated copper grid for transmission electron microscopy (TEM, JEOL 200CX and 2010F). The dark-field scanning transmission electron micrograph (STEM, Figure 4-7A) and elemental map (Figure 4-7B) of the extracted IrO_2 nanostructures indicated the formation of the nanowire structures within AG-gels. Such nanowire morphology was more clearly shown in the bright-field TEM image (Figure 4-7C) and comparable with the IrO_2 nanowires assembled in a bulk solution (Figure 4-7D) despite some polymer debris around the structures.

4.4.2 Biomineralization of Co_3O_4 Nanostructures within Microgels

Microgels incorporating the E4 viruses (denoted E4-gels) were used for assembling Co_3O_4 nanostructures. Our previous study showed that the E4 clone served as a good template for assembling Co_3O_4 nanostructures. The microgels were incubated in 20 mM cobalt (II) chloride hexahydrate ($CoCl_2 \cdot H_2O$, Riedel-deHaën) overnight and then rinsed with Milli-Q water. The cobalt ions were reduced by sodium borohydride and then the microgels were magnetically stirred in excess deionized water for 2 days. The microgels showed a black color, indicating the formation of Co_3O_4 (Figure 4-8B), while the microgels were transparent (Figure 4-8A). ICP-AES results indicated that E4-gels converted 57.1 % Co^{2+} to Co_3O_4, while the conversion efficiency of KE-gels is about 36.9 %. This significant increase of mineralization implies the importance of the inserted glutamic acids for biomineralization. However, the morphologies of the Co_3O_4 nanowires self-assembled within the microgels (Figure 4-9A) were quite

different from those synthesized in an aqueous phase (Figure 4-9B).

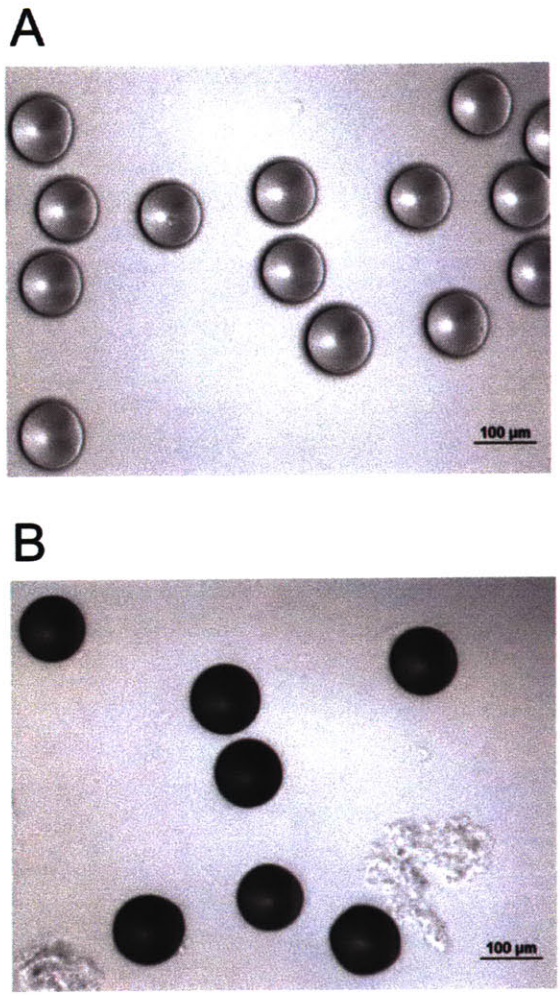

Figure 4-8: **Optical micrograph of E4-gels (A) before and (B) after Co_3O_4 mineralization.**

4.5 Conclusion

Here we have described the biomineralization of various inorganic materials within microgels loaded with genetically modified M13 viruses. The viruses carried specific peptide binding motifs in their coat proteins, which were proven to have distinctive affinities to metal oxides or metals. A microfluidic device was employed to produce

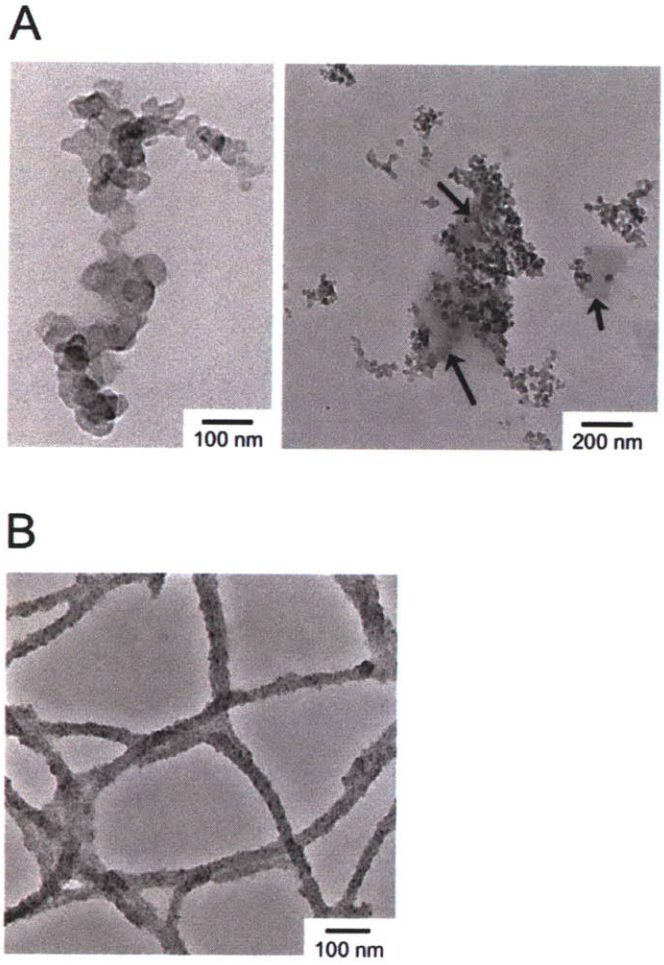

Figure 4-9: **Transmission electron micrograph of Co_3O_4 nanostructures within E4-gels (A) and in a bulk aqueous solution (B).**

monodisperse aqueous droplets containing the viruses in a laminar flow, allowing the maintenance of their structural integrity. Three-dimensional nanostructures of IrO_2 and Co_3O_4 were assembled within polymer microgels. It is expected that the current microgel-supported biotemplating approach can provide a micron-scale building block of inorganic materials useful for sensors, photochemical devices, chemical reactors, drug delivery carriers, embolic materials, etc.

Chapter 5

Electrochromic Nanowires Assembled on Genetically Modified Viruses

We report a method to formulate IrO_2 nanowires self-assembled on genetically modified M13 viruses into an electrochromic film on a transparent conductive electrode. The prepared IrO_2 nanowire film has a highly open porous morphology that facilitates ion transport. Accordingly, the electrochromic responses of the IrO_2 nanowires are limited by poor electron mobility of the nanowire film if the ion conductivity is higher than about 20 mS cm^{-1}.

5.1 Background

Electronic paper is a thin, portable display device exhibiting a paper-like color contrast with ultra-low power consumption. It is designed to provide the viewer the experience of reading from paper, while having the capability of updatable information from other electronic devices. Electronic paper is able to provide the true book-like experience under a wide range of lighting conditions and requires no power

to maintain images. The first paper-like display device, called Gyricon, was developed in the 1970s by Nick Sheridon at Xerox's Palo Alto Research Center. The Gyricon was based bichromal polyethylene microspheres ($20 \sim 100$ μm in diameter) having a dipole structure composed of negatively charged black polymer on one side and positively charged white polymer on the other. The microspheres are suspended in oil bubbles which are embedded within a transparent silicone sheet so that they can rotate freely. The polarity of the voltage applied to each pair of electrodes then determines which of the white and black sides is face-up, thus giving the pixel a white or black color. In the 1990s another type of electronic paper was invented by Joseph Jacobson, who later co-founded the E Ink corporation which formed a partnership with Philips Components to develop and market the technology. In 2005, Philips sold the electronic paper business as well as its related patents to Prime View International. One early version of electronic paper consists of a sheet of transparent microcapsules with a diameter of about 40 μm. Each capsule contains an oily solution containing black dye with numerous titanium dioxide (TiO_2) particles suspended within. The TiO_2 particles are slightly negatively charged, and each one is naturally white. In early versions, the underlying circuitry controls whether the white particles were at the top of the capsule (so it looked white to the viewer) or at the bottom of the capsule (so the viewer saw the color of the oil). This was essentially a reintroduction of the well-known electrophoretic display technology, but the use of microcapsules allowed the display to be used on flexible plastic sheets instead of glass. The microcapsules are held in a layer of liquid polymer, sandwiched between two arrays of electrodes, the upper of which is made from indium tin oxide, a transparent conducting material. The two arrays are aligned so that the sheet is divided into pixels, which each pixel corresponding to a pair of electrodes situated either side of the sheet. The sheet is laminated with transparent plastic for protection, resulting in an overall thickness of 80 μm, or twice that of ordinary paper. The network of electrodes is connected

to display circuitry, which turns the electronic ink 'on' and 'off' at specific pixels by applying a voltage to specific pairs of electrodes. Applying a negative charge to the surface electrode repels the particles to the bottom of local capsules, forcing the black dye to the surface and giving the pixel a black appearance. Reversing the voltage has the opposite effect - the particles are forced from the surface, giving the pixel a white appearance. A more recent incarnation of this concept requires only one layer of electrodes beneath the microcapsules. The current limitation of the E ink technogy is a long screen refreshing time. The fastest color switching time is around 300 ms, which is too slow to make movies on electronic paper.

Transition metal oxides are promising materials for EPDs as some of them exhibit light-absorbing electrochromic properties. Electrochromism is a reversible color change of redox compounds that can be modulated by electric potential application. A variety of electrochromic materials have been studied to improve optical switching speed, color contrast, and electrochemical stability. In particular, fast-responding electrochromic materials could provide a breakthrough for energy-efficient, paper-like display devices. IrO_2 is a very attractive material because of its fast redox switching kinetics, good open-circuit memory, mild operating potential range, and good long-term electrochemical stability. The electrochromic property of IrO_2 originates from the multiple oxidation states of Ir modulated by an electric field-assisted transfer of electrons across the metal/oxide interfaces. For the coloration process, electrons are removed from the oxide to the metal substrate through the application of anodic potential. Charge repulsion causes an equivalent amount of positive mobile charge carriers to be ejected across the metal-electrolyte interface, thus preserving electroneutrality inside the oxide. Similarly, during bleaching, electrons are injected into the oxide film from the metal while compensating positive charge is injected at the oxide-electrolyte interface.

The ion migration through the electrochromic layer is generally the rate-limiting

step of the overall response in a non-porous electrochromic electrode. Anodically grown IrO_2 film (AIROF) prepared on an Ir electrode showed a switching time of 10 $\sim$ 40 ms for 50 $\sim$ 60 % attenuation of reflection in 0.5 M H_2SO_4 in the visible region. The reflectance attenuation of 60 % is equivalent to a transmission change of about 30 %. These fast responses are thought to be a result of the highly porous and hydrated nature of the AIROF: 'free' H_2O molecules in the electrolyte within the pores and 'bound' H_2O on the IrO_2 surface supply the protons required for the reduction of IrO_2. The availability of protons within the film enables fast bleaching rates to be maintained. However, when AIROF was grown on a transparent SnO_2-coated glass electrode (100 Ω sq^{-1}), the response time increased to about 0.2 s for transmission changes of about 30 %. A faster switching response, about 50 ms, for the same optical change was reported in the IrO_2 films sputtered on a more conductive In-doped SnO_2 (ITO) electrode (20 Ω sq^{-1}), but the switching speed was still much slower than the AIROP on an Ir electrode. These results indicate that the overall electrochromic kinetics can be limited by the poor electron mobility of the conductive electrode. Therefore, the design of electrochromic electrodes requires the careful consideration of both the ion and electron transport processes.

5.2 Virus-templated IrO_2 Nanowires

In this study IrO_2 nanowires were prepared using M13 viruses genetically modified to carry an IrO_2-binding peptide, AGETQQAM, which was identified through biopanning using a type 8 phage display library, as described in the previous chapters. To prepare hydrated Ir precursors, 25 mM hydrated $IrCl_3$ (100 mL, Alfa Aesar) was neutralized to pH 7.5 by adding 1 N NaOH and incubated for 48 h at room temperature in the dark. The precursor solution (380 μL) was then mixed with the M13 viruses (10^{11} viruses in 20 μL) and incubated for at least 30 min. An electroporator (Bio-

Rad GenePulser) was used to repeatedly apply 1.05 kV electric pulses, exponentially decayed with $\tau \sim 1$ ms, to the precursor/virus mixture solution between a pair of aluminium electrodes with 2 mm gap distance for 2 min at a frequency of 0.5 Hz. The electric pulses oxidize Ir^{3+} ions, resulting in an apparent color change of the solution from pale brown to dark purple with the appearance of a characteristic IrO_2 absorbance spectrum (Figure 5-1A and B). Transmission electron microscopy (TEM) images (Figure 5-1C and D) show the formation of IrO_2 along the long axis of the virus, and the the nano-crystalline domains (insert in Figure 5-1D). However, there was no detectable formation of inorganic structures on M13 viruses (M13KE, New England Biolabs, Ipswich, MA) that carried no peptide insert. These results indicate that the IrO_2 nanowires were self-assembled through a specific interaction between the IrO_2 nanoclusters and the IrO_2-binding peptide displayed on the virus.

IrO_2 nanowire films were prepared by filtering the nanowires through a 0.45 μm mixed cellulose ester filtration membrane (Figure 5-2A). As the solvent fell through the pores, the nanowires were trapped on the surface of the filter membrane, forming an entangled nanowire cake. The prepared nanowire cake on the filter was transferred to an ITO-coated glass slide (4 - 8 Ω Sq^{-1}, SiO_2 passivated, CG-41IN-S107, Delta Technologies, Ltd., Stillwater, MN), and then a slice of polydimethylsiloxane fully wetted by acetone was laid on the backside of the membrane. It was then dried in air at 50°C for 30 min while all of the layers were compressed with clips to maintain the intimate contact of the nanowires to the ITO glass slide. This incubation also gives the nanowires cohesion with each other, which helps preserve the film integrity. The filter membrane on the top of the IrO_2 nanowires was then removed through dissolution in a fresh acetone bath, resulting in the nanowire film on the ITO glass. The as-prepared IrO_2 film shows an evenly dark purple color (Figure 5-2B) and a highly open porous mesh morphology derived from the entanglement of the nanowires (Figure 5-2C). Such morphology was expected to be advantageous for fast electrochromic

responses because of the large surface area-to-mass ratio of IrO_2, which facilitates the ion transfer across the electrolyte/IrO_2 interfaces.

5.3 Electrochemical Properties of IrO_2 Nanowires

To determine the electrical properties of electrolytes used in this study, the alternating current (a.c.) analysis was carried out using impedance spectroscopy (Model No. 1260, Solartron). A sinusoidal voltage with the amplitude of 10 mV and the frequency range of 1 MHz to 1 Hz was applied to a cell and the sinusoidal current passing through the cell was measured. Aluminium or copper plates were used as an electrode and both of them were considered as a blocking electrode. To fit the data, as an equivalent circiut model representing the a.c. response, we considered the case of a cell consisting of a polymer electrolyte containing one mobile species sandwiched between two blocking electrodes. In this case, the bulk polarization and ionic migration are physically in parallel and thus their representative componenets, the resistor (R) and the capacitor (C), are connected in parallel and both are in series with the eletrode capacitance. The complex admittances of the resistor and capacitor connected in parallel are additive; therefore a complex impedance plot representing an electrolyte can be predicted from the equation (5.1).

$$Z^*_{total} = \frac{1}{\frac{1}{R} + j\omega C} = R\left[\frac{1}{1+(\omega CR)^2}\right] - jR\left[\frac{\omega RC}{1+(\omega RC)^2}\right] \tag{5.1}$$

where Z^* is the complex impedance, R is the resistance, C is the capacitance, and ω is the angular frequency. At high frequencies, the equivalent circuit reduces to a parallel RC combination which gives rise to the semicircle in the complex impedance plane.

Figure 5-3 shows the measured ion conductivities of aqueous electrolytes of $HClO_4$, $LiClO_4$, $NaClO_4$, and $KClO_4$ as a function of the dissolved salt concentration at room

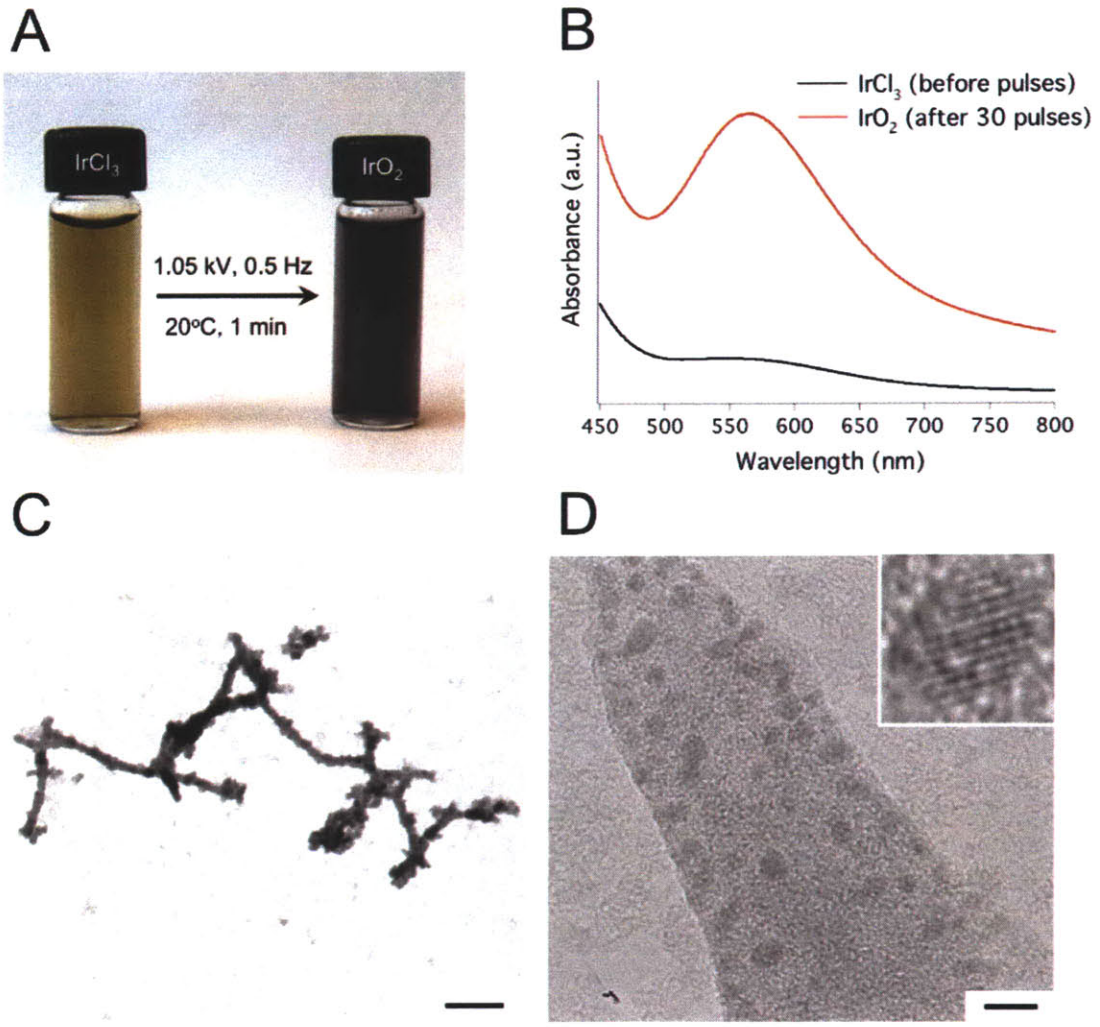

Figure 5-1: **Virus-templated IrO_2 nanowires.** **A** and **B**, Photographs (**A**) and absorption spectra (**B**) of the hydrated Ir^{3+} ions and the IrO_2 nanowires. **C**, TEM image of virus-templated IrO_2 nanowires taken using JEOL 200CX (Akishima, Japan) at 200 kV. Scale bar = 250 nm. **D**, High resolution TEM image of an individual IrO_2 nanowire taken using JEOL 2010 at 200 kV. Scale bar = 5 nm. The insert shows a lattice structure of IrO_2 nanocrystal in the nanowire.

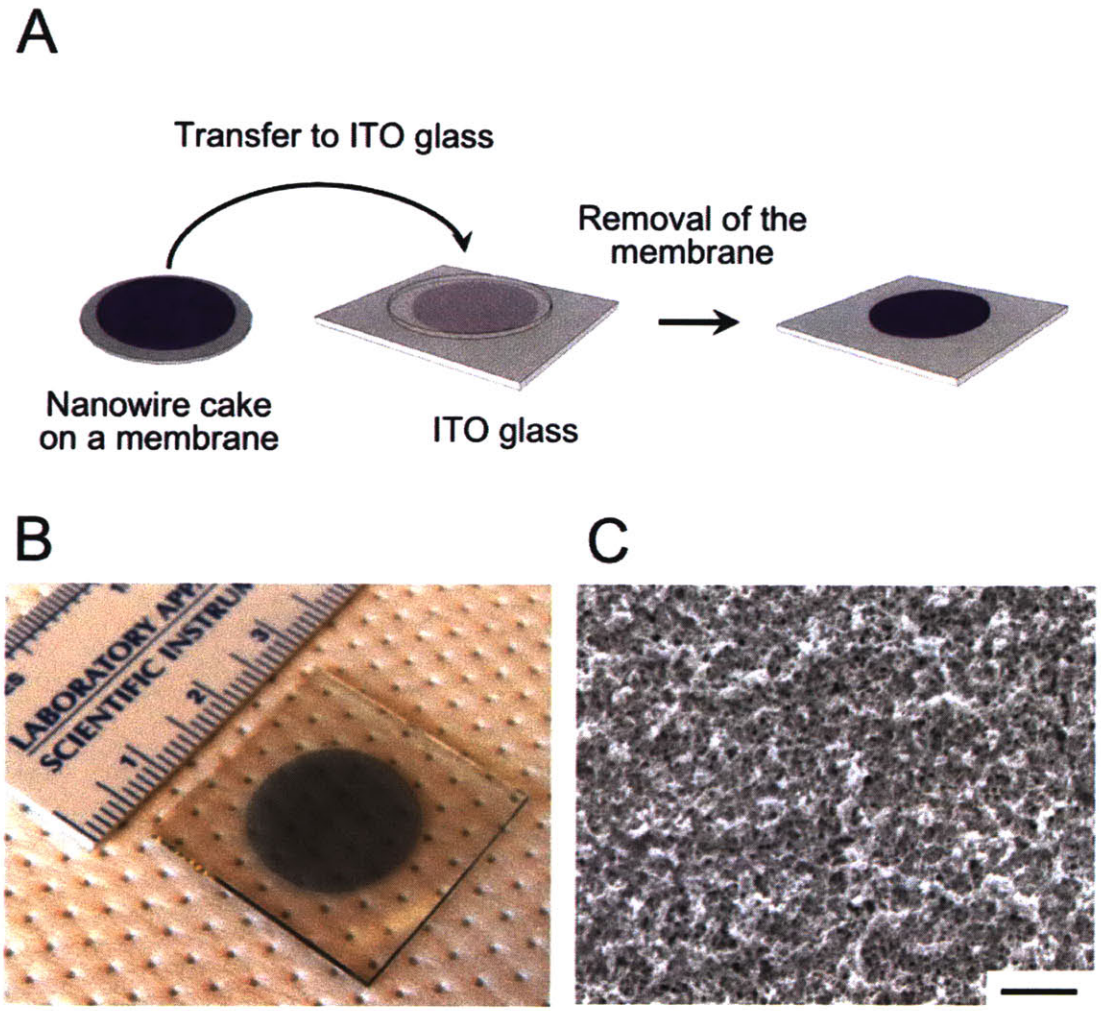

Figure 5-2: **IrO_2 nanowire films on ITO glass slide.** **A**, Fabrication procedures of a nanowire film on an ITO glass slide via vacuum filtration and stamping. **B** and **C**, Photograph (**B**) and SEM image of the surface morphology (**C**) of as-prepared IrO_2 nanowire film on an ITO glass slide. Scale bar = 5 μm.

temperature. As expected, compared with other alkali metal electrolytes, $HClO_4$ has the highest conducitivity at the same concentrations. However, the ion conductivities are quite similar among different alkali metal perchlorates. This behavior can be explained from the definition of ion conductivity (σ): $\sigma = \sum_i |z_i| F u_i c_i$, where $z_i \equiv$ the valence of the i_{th} species, $F \equiv$ Faraday constant ($\sim$ 96,500 C mol^{-1}), $u_i \equiv$ the ion mobility (cm^2 V^{-1} s^{-1}), $c_i \equiv$ concentration (moles cm^{-3}). The ion diffusivity is proportional to the ion mobility as described in the Einstein relationship (5.2). The ion mobilities and diffusivities at 25°C in aqueous solution are listed in Table 5.1. Note that the ion diffusivity is in the order of $K^+ > Na^+ > Li^+$. The ion dissociation constant of perchlorates is expected to be in the order of $Li^+ > Na^+ > K^+$, and thus at the same molar concentration the actual ion number in the $LiClO_4$ solution is higher than that in other solutions. Therefore, the product of the ion diffusivity and the ion concentration should be similar between the different perchlorates. This is the reason their ion conductivities are similar at a given salt concentration and temperature.

$$\frac{D_i}{u_i} = \frac{RT}{|z_i| F} \approx \frac{25.7}{|z_i|}\text{mV at 25°C} \tag{5.2}$$

$$\sigma \equiv R\frac{d}{A} \tag{5.3}$$

Table 5.1: Ion mobilities and diffusion coefficients at 25°C.

Species	u_i (cm^2 V^{-1}sec^{-1})	D_i (cm^2 sec^{-1})
H_3O^+	3.63 x 10^{-3}	9.33 x 10^{-5}
Li^+	4.01 x 10^{-4}	1.03 x 10^{-5}
Na^+	5.19 x 10^{-4}	1.33 x 10^{-5}
K^+	7.62 x 10^{-4}	1.96 x 10^{-5}

To determine the rate limiting step of the redox reaction of IrO_2 nanowires, it was hypothesized that the redox switching speed increases with increasing the ion

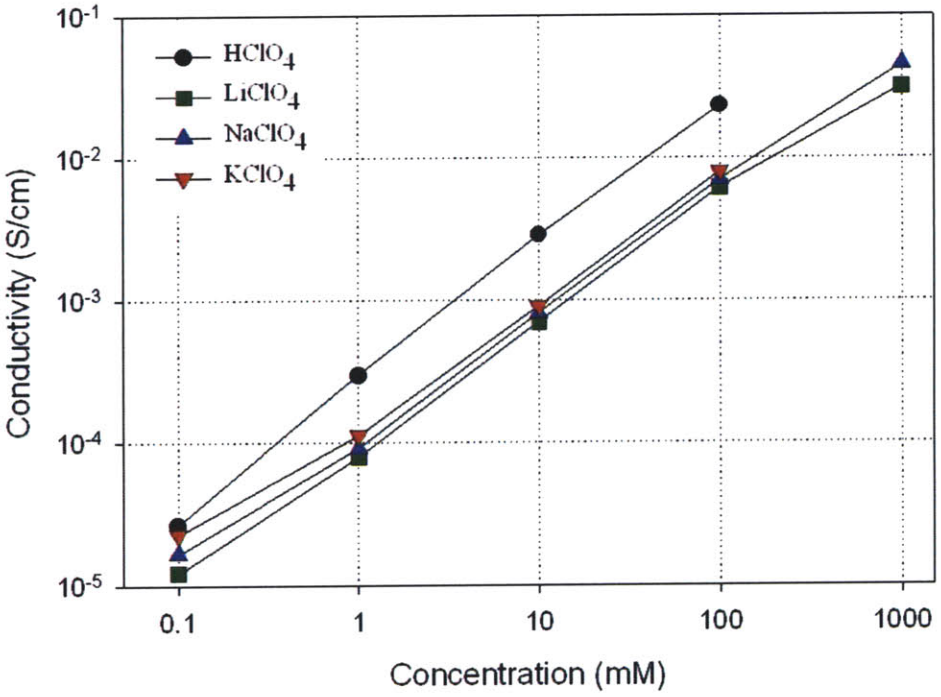

Figure 5-3: **Ion conductivities of aqueous electrolytes of $HClO_4$, $LiClO_4$, $NaClO_4$, and $KClO_4$ as a function of the dissolved salt concentration.**

conductivity of electrolytes and then is saturated at a specific conductivity, σ_{min}, above which the switching speed is independent of the conductivity.

The electrochemical properties of the IrO_2 nanowire film on the ITO glass slide were analyzed using a potentiostat (PGSTAT302, Autolab) with a Pt counter electrode and a Ag/AgCl reference electrode. The redox potentials of the IrO_2 nanowires were determined via cyclic voltammetry in 100 mM $HClO_4$ (*aq.*) (Figure 5-4A). The cathodic peak is due to the intercalation of proton into the hydrated IrO_2 layer, while the anodic peaks derive from proton ejection. The redox reactions of the IrO_2 nanowires were accompanied by an intense color change between dark blue and transparent states. The IrO_2 nanowires exhibited anodic electrochromism at two oxidation potentials, + 0.43 V and + 0.63 V, while the cathodic transition was one-step process around + 0.50 V. A similar phenomenon has been observed in IrO2 films prepared by pulsed anodic electrodeposition. It was found that IrO_2 showed anodic blue and black electrochromism at + 0.50 V and + 0.85 V (*vs.* a saturated calomel electrode) in phosphate buffered saline (pH 7.2, 126 mM NaCl), respectively, while a cathodic scan exhibits only a single transition from black to a transparent state. This phenomenon might be related to the fact that during anodic polarization the H^+ ejection induces the changes in Ir valence; *i.e.*, insulating $Ir(OH)_3$ to metallic IrO_2. Two distinctive peaks suggest that IrO_2 has two distinctive layers, hydrated and dried, that have different reaction kinetics. Deeper in the nanowires only free H^+ can penetrate, while H_3O^+ ions can be transported only through amorphous, hydrated domains. In the case above, $Ir(OH)_3$ is partially changed into IrO_2 at + 0.5 V and the remaining $Ir(OH)_3$is completely converted to IrO_2 at + 0.85 V.

It was expected that the electrochromic responses of the IrO_2 nanowires were not limited by the ion conduction because of their relatively short path-length of ion transport. The redox potentials of the IrO_2 nanowires were measured as a function of the ion conductivity (σ) of the $HClO_4$ solution. Figure 5-4B shows that the cathodic

peak voltage increases with increasing ion conductivity, while the proton ejection from the IrO_2 nanowires is independent of the ion conductivity. The cathodic peak shift seems to be caused by the slower redox reaction in the IrO_2 nanowires than the voltage-sweeping rate. However, at $\sigma >$ about 20 mS cm^{-1}, the proton injection into IrO_2 nanowires became fast enough, and thus the electrochromic responses was no longer affected by the ion conductivity. This result was confirmed by the chronoamperometric change of the IrO_2 nanowires. A step-wise voltage was repeated applied between - 0.2 V and + 1.0 V with predetermined intervals. Figure 5-4C shows the redox switching time of the IrO_2 nanowires as a function of the ion conducitivity. The measured redox switching time, defined as the time it takes to decrease to 50 % of the peak current value, decreases with increasing ion conductivity. However, at $\sigma >$ 20 mS cm^{-1}, it reaches a plateau value, about 1 s for oxidation and about 0.3 s for reduction, respectively. These results are consistent with those of the cyclic voltammograms in Figure 5-4c, where no change of the redox potentials was observed at $\sigma >$ 20 mS cm^{-1}.

The thickness (or amount) of the electrochromic materials correlates with their response kinetics. In this study, when 6.9 μg cm^{-2} IrO_2 nanowires were deposited on ITO, the response times were 96 msec for oxidation and 40 ms for reduction with the optical contrast of 6.1 $\pm$ 2.1 %. The redox responses were relatively fast, but not useful because of the low optical contrast. Note the optical contrast is a critically important parameter for the practical applications of electrochromic devices, and about 60 % transmission change is known to be required for an efficient display. As expected, the redox responses became slower as the amount of IrO_2 nanowires deposited increased (Figure 5-4D). The highest optical contrast, 52.8 $\pm$ 4.6 %, was observed when the nanowire thickness was about 104.6 μg cm^{-2}. This amount of the nanowires corresponds to the thickness of 1.21 $\pm$ 0.34 μm, as determined by a Tencor P10 profilometer. However, this high optical contrast was achieved through

the sacrifice of the redox kinetics: 1.33 s for oxidation and 0.54 s for reduction. Particularly, the proton ejection (oxidation) became much slower as compared to its injection (reduction). This result suggested that the oxidation of the IrO_2 nanwires was determined by the electron mobility through the nanowire layer rather than the ion conduction. In a non-porous structure, the reduction occurs from the outermost layer, which is in contact with electrolytes, and thus during anodic polarization electrons can be extracted from insulating $Ir(OH)_3$ through the underlying well-connected metallic IrO_2 layer. However, in a highly porous nanowire film, the oxidation can occur ubiquitously in any part of the nanowire film due to its short charge transfer path-length. This feature can complicate the oxidation processes: if the nanowires bound to the electrode is still in a reduced state, they can work as an insulating barrier that electrically isolates the upper nanowire layer from the electrode. Therefore, a highly porous morphology is advantageous for ion transport but detrimental for electron mobility in the nanowires.

5.4 Solid Polymer Electrolytes

A SPE has attracted great attention due to their application to a wide range of solid-state electronic devices with high energy density, geometrical flexibility, and safety. General drawback of the solid electrolytes is their relatively low ion conductivity. Therefore, there have been a lot of investigations on a SPE to increase the ion conductivity, while maintaining favorable mechanical and chemical properties. Other factors of a SPE for ECD applications include optical and interfacial properties. In this study, two different types of SPEs were examined: PMMA (poly(methyl metacrylate)-based gel electrolytes and crosslinked polymer electrolytes.

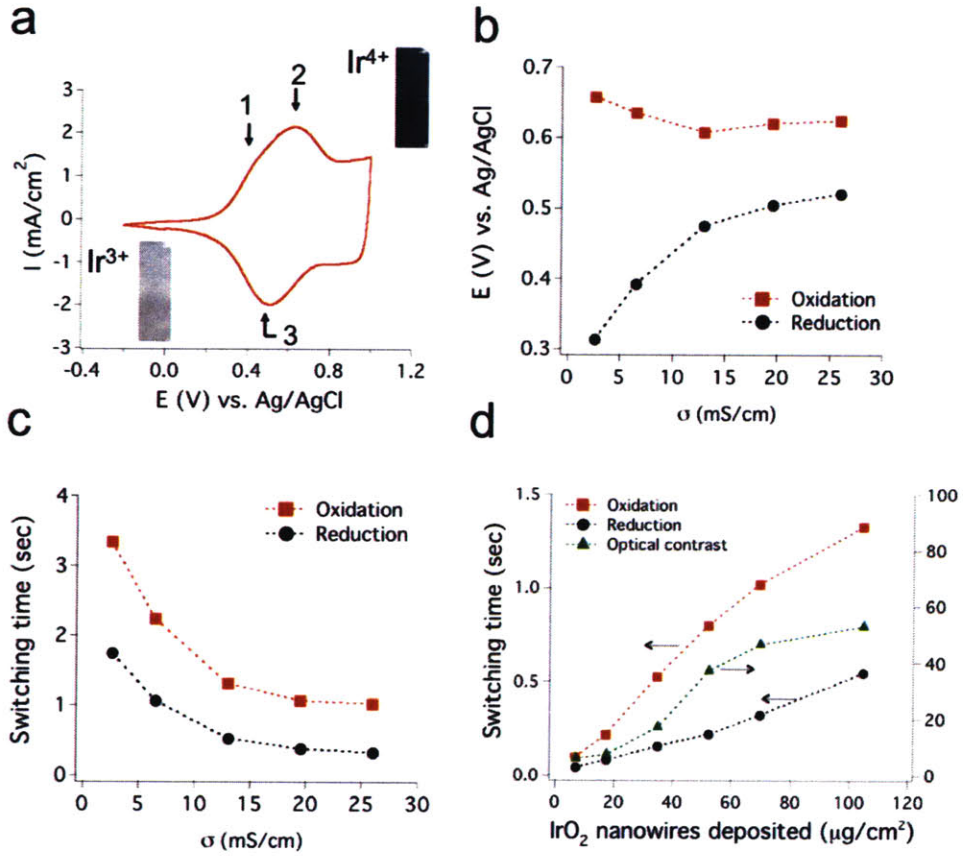

Figure 5-4: **Electrochemical characterization of IrO_2 nanowire films.** **A**, Cyclic voltammograms (CV) of the IrO_2 nanowires scanned at 10 mV s^{-1} in 100 mM $HClO_4$ (σ = 26.0 mS cm^{-1}) with photographic images of an IrO_2 nanowire film in the bleached (left) and colored (right) states. **B** and **C**, redox potentials (**B**) and switching times (**C**) of the IrO_2 nanowires as a function of the ion conductivity of the electrolyte. **D** and **E**, switching times (**D**) and percent transmission at 580 nm (**E**) as a function of the amount of the IrO_2 nanowires deposited.

5.4.1 PMMA-based Gel Electrolytes

A PMMA-based gel electrolyte has been widely used since Iijima and his colleagues suggested PMMA as a gelating agent for lithium ion electrolytes. PMMA is optically transparent, electrically insulating, and mechanically acceptable. It has thus been used for motorcycle helmet visors and replacement intraocular lenses in the eye, both of which can be categorized into an optical device. Moreover, due to the superior compatibility with a plasticizer, the PMMA gel electrolyte does not have any macroscopic phase separation in a wide range of conditions. Otherwise, the polymer matrix becomes opaque because of different refractive indices of the polymer-rich phase and the plasticizer-rich phase.

Briefly, PMMA (MW 120 kDa, Aldrich) and $LiClO_4$ (battery grade, dry, 99.99 %, Aldrich) were dissolved in propylene carbonate (PC, anhydrous, 99.7 %, Aldrich) at 80°C under magnetic stirring. The final lithium ion concentration was set to 1.0 M, while the PMMA concentration was changed from from 10 wt% to 25 wt%. The ECD was assembled by joining an IrO_2 nanowire-deposited electrode with a counter electrode. Polished ITO glass slides ($4 \sim 8\ \Omega\ Sq^{-1}$, SiO_2 passivated, CG-41IN-S107, Delta Technologies, Ltd.) were used as an electrode. A silicone spacer (Silicone Isolators, JTR13R, Grace Bio Labs, Inc.) was used to keep the distance between the two electrodes of 0.5 mm. The electrolyte solution was injected into the device using a 10 mL plastic syringe with a 21-gauge stainless steel needle. The syringe and needle were pre-warmed at 80°C. The electrolyte solution was then solidified to form a gel at ambient temperatures.

Figure 5-5 shows that the colored (oxidized) and bleached (reduced) states of IrO_2 nanowire-coated ITO glass electrodes operated at $\pm$ 3 dc voltages. The coloration/bleaching process takes a few seconds. There were no significant effects of different PMMA concentrations on the coloration efficiency and switching speed of IrO_2 nanowires. This observation is consistent with a previous report describing the

effect of the PMMA concentration on the ion conductivity of gel electrolytes. The reported Li^+ ion conductivities were about 8 x 10^{-3} S cm^{-1} in the absence of PMMA and 1 x 10^{-3} S cm^{-1} at 25 wt% PMMA concentration, respectively. The presence of the PMMA (MW 90 kDa) imparts a very high viscosity to the system without significantly decreasing the ion conductivity, *i.e.*, the conductivity of the gel remains very close to that of a liquid electrolyte. They concluded that PMMA acts primarily as a 'stiffener' and ion transport occurs through a continuous conduction path of PC molecules.

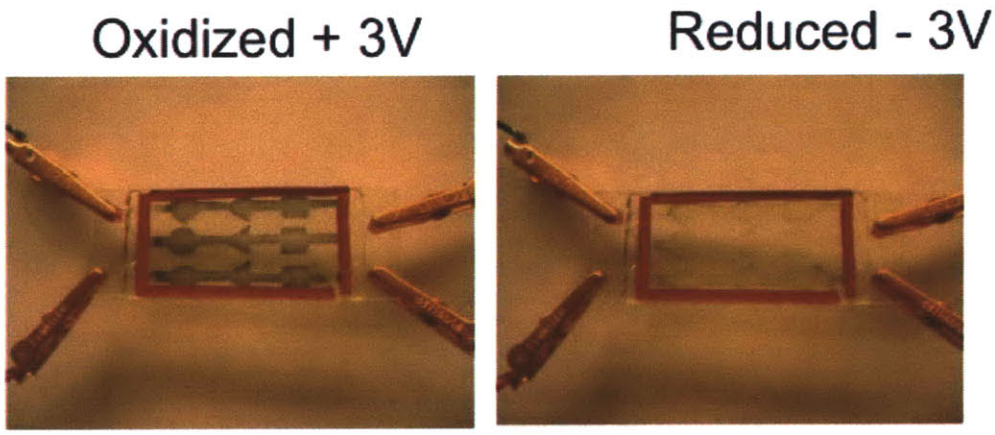

Figure 5-5: **the colored (oxidized) and bleached (reduced) states of IrO_2 nanowire-coated ITO glass electrodes with lithium-PC-PMMA electrolytes operated at ± 3 dc voltages.**

To avoid the electrolyte leakage problem of an ECD, it is highly desirable to increase the viscosity of polymer electrolytes while maintaining high ion conductivity. It seems likely that a tradeoff point of the PMMA concentration exist between the ion conductivity and the viscosity. However, the situation is actually more complicated, because the 'processability' to fabricate devices using the polymer electrolytes also needs to be considered. If the viscosity of polymer electrolytes is above the order of 10^3 Pa s, they are quite difficult to manipulate for ECD assembly. The ideal polymer solution has a low viscosity during ECD fabrication, but is completely solidified at

ambient temperatures. However, when the PMMA concentration was increased above 20 wt%, the electrolyte became too viscous to inject into a device, although at room temperature the solidification was not still enough as a leakage-free solid device.

To solve this problem, a higher molecular weight PMMA was tried because the viscosity of a polymer solution can be effectively increased by raising the molecular weight, as represented by the Mark-Houwink equation. At the same polymer concentration, the 350 kDa PMMA gel electrolyte had an higher apparent viscosity than 120 kDa. It worked very well as an electrolyte for an ECD; however, the solution was slightly opaque in a glass vial (3 cm in diameter) even at a relatively low concentration (*ca.* 15 wt%). Another problem is that the high molecular weight PMMA is very difficult to handle for the device assembly due to the high viscosity even at 80^{o}C, while the increased molecular weight could not completely solidify the gel electrolyte.

5.4.2 Crosslinked Polymer Electrolytes

To more effectively solidify the polymer electrolyte while maintaining a high ion conductivity, crosslinked polymer system was employed. Crosslinked polymer electrolytes have been studied by many research groups since it was found that crosslinked polyethylene glycol dimethacrylate (PEGDMA) electrolytes containing a plasticizer have high ionic conductivity, around 10^{-3} S cm^{-1}, at ambient temperature. However, crosslinked polymer electrolytes are typically glassy and hence are not mechanically stable under external forces. It was suggested that this brittleness can be reduced using different combinations of lithium salts and plasticizers, but this has always accompanied the reduction of ion conductivity. To solve this problem, polymer blend or copolymer systems have been investigated. For example, a highly conducting (5 x 10^3 S cm^{-1}), non-brittle polymer electrolyte film was fabricated by crosslinking polyethylene glycol diacrylate (PEGDA) and polyvinylidene fluoride (PVDF) in a mixed solvent containing EC-DMC (ethylene carbonate-dimethyl car-

bonate) (2:1), in which PVDF is slightly soluble. A series of highly conductive and flexible SPEs has also been suggested using crosslink polymerization of PEGDMA and alkyl methacrylate in the presence of 1.3 M $LiPF_6$ dissolved in a plasticizer. Thermal polymerization with 2,2-azobisisobutyronitrile (AIBN) as an initiator could result in a flexible freestanding SPE film having a Li^+ ion conductivity of 3.3 x 10^3 S cm^{-1} at room temperature.

In this study, the *in situ* crosslink polymerization of PEGDMA and methyl methacrylate (MMA) was used to obtain a SPE, which is highly ion conducting (> 10^3 S cm^{-1}), self-supporting, transparent in a wide range of temperature, and easy to prepare. Sixteen different combinations of PEGDMA (Mn 550, Aldrich), MMA, and PC were tested for polymerization with $LiClO_4$ in PC. The final concentration of lithium ion was set to 1.0 M. The ratio of PEGDMA:MMA examined was 8:2, 7:3, 6:4 and 5:5. The percentage of the monomers was set to 10, 20, 30 or 40 % of the total weight of polymer electrolytes. The polymerization was carried out at 80°C for 3 h. Highly transparent, freestanding polymer gels could be made from all of the formulations examined. This indicates that this approach can guarantee a good dimensional stability and transparency of polymer electrolytes. In addition, the ECD fabrication was much easier due to low viscosity of monomer solutions, and air bubble entrapment was easily avoided. However, the ECD did not work at all when the crosslinked polymer electrolytes were used. It is still not clear what inactivated electrochromic properties of IrO_2 nanowires after *in situ* radical polymerization. It is suspected that the generated radicals react with the IrO_2 nanowires, resulting in chemical changes of the nanocrystals. This inactivation can be associated with the high temperature, 80°C, during polymerization. Another possibility is that the IrO_2 nanowires are detached from the ITO electrode because of mechanical tension caused by polymerization-induced structural changes. MMA can infiltrate into small gaps between nanowires and an electrode.

5.5 Device Assembly and Sealing

Moisture must be suppressed in the device because it can significantly affect the lifetime and open circuit memory of ECDs even at a ppm level. When electric potential is applied, water molecules might be able to react with electrons in IrO_2 nanowires, resulting in generation of hydrogen gas.

$$2H_2O + 2e \rightleftharpoons H_2 \uparrow + 2OH^-, -0.828(E^o/V)$$

This is why, as repeating the ECD test, the formation of small bubbles are observed in the device. Moisture contained in the air can be entrapped during device fabrication or it can permeate into the device through small crevices through or between silicon spacers and electrodes.

Another source of moisture can be water moleucles bound to the materials used, such as electrodes, IrO_2 nanowires, PMMA, PC, and lithium salts. Until now, our prototype ECDs have been fabricated in air without comprehensive drying procedures. Briefly, high purity PC and $LiClO_4$ were used as received, but they were used in a glove box. PMMA was dried in a dry oven at 80°C for 3 days. ITO glass and IrO_2 nanowire-coated electrodes were just dried in a dry oven at 80°C for 30 min. These conditions are so mild that we cannot completely dehydrate the materials. To more rigorously eliminate the moisture, PMMA was dried under vacuum at 120°C for 3 days and are placed in a glove box. Dehydration methods for the nanowires is yet determined because we do not know the effects of vacuum drying on physicochemical properties of IrO_2 nanowires.

5.6 Conclusion

Virus-templated IrO_2 nanowires were prepared using a electropulsing technique, and electrochromic films were prepared by depositing the prepared nanowires on transparent conducting electrodes. The prepared IrO_2 nanowire film has a highly open macroporous morphology that facilitates ion transport. Accordingly, the electrochromic responses of the IrO_2 nanowires are limited by the electron mobility in the nanowire film.

Chapter 6

Photochemical Decomposition of Bisphenol A using Multilayered TiO_2 Nanoparticles on Electrospun Fibers

Endocrine disruptors (e.g., bisphenol A) are environmental pollutants that interfere with the bodys endocrine system because of their structural similarity to natural and synthetic hormones. Due to their strong oxidizing potential to decompose such organic pollutants, colloidal metal oxide photocatalysts have attracted increasing attention for water detoxification. However, achieving both long-term physical stability and high efficiency simultaneously with such photocatalytic systems poses many challenges. Here we report a layer-by-layer (LbL) deposition approach for immobilizing titanium dioxide (TiO_2) nanoparticles while maintaining a high catalytic efficiency for photochemical decomposition of bisphenol A. Anatase TiO_2 nanoparticles of approximately 7 nm in diameter self-assemble in consecutive layers with positively charged polyhedral oligomeric silsesquioxanes on a high surface area, porous electrospun polymer fiber

mesh. Under the air mass 1.5 global illumination, the TiO_2 LbL nanofibers decompose approximately 2.2 mg bisphenol A per mg of TiO_2 in 40 hours of illumination, maintaining first-order kinetics with a rate constant (k) of 0.15 h^{-1} for over 40 hours. Although the colloidal TiO_2 nanoparticles initially show significantly higher photocatalytic activity ($k \approx 0.84\ h^{-1}$), the rate constant drops to $k \approx 0.07\ h^{-1}$ after 4 hours of operation, seemingly due to particle agglomeration. In the BPA solution treated with the multilayered TiO_2 nanofibers for 40 hours, the estrogenic activity, based on human breast cancer cell proliferation, is significantly lower than that in the BPA solution treated with colloidal TiO_2 nanoparticles under the same conditions. This study demonstrates that the LbL deposition effectively immobilizes TiO_2 nanoparticles on electrospun polymer nanofibers for efficient, stable photochemical water remediation.

6.1 Background

Endocrine disruptors are thought to comprise a wide range of substances, including various pharmaceuticals, dioxin, polychlorinated biphenyls, pesticides, and some plasticizers. They have been shown to produce adverse developmental, reproductive, neurological, and immune effects in both humans and wildlife [112, 3, 15, 4, 2]. Bisphenol A (4,4-isopropylidenediphenol or BPA) is a well-known endocrine disruptor, which mimics the action of estrogen and causes neuro-developmental and hormone disorders, oxidative stress, and inflammation [118, 119, 120, 121]. Over 4 million metric tons of BPA are produced annually and consumed in phenoxy resins, polycarbonate plastic products, and dental sealants. BPA is released from polymer resins via hydrolytic degradation of polymers and is often found in aquatic environments [54, 59]. BPA has long been known to elicit very weak estrogenic activity. However, recent findings on its molecular mechanisms have shown a variety of pathways through which BPA can stimulate cellular responses at very low doses [57, 122]. In

particular, when BPA is metabolized in the body, it can cause DNA damage by forming chemical adducts such as deoxyguanosine 3-monophosphate-bisphenol-o-quinone or bisphenol A-3,4-quinoneguanine-N7, and it can provoke a very strong estrogenic activity by forming metabolites such as 4-methyl-2,4-bis(p-hydroxyphenol)pent-1-ene [125, 56, 25, 5, 6]. A number of chemical and biological methods have been reported to eliminate endocrine disruptors in the aqueous environment; however, the biological processes usually take too long for practical applications, and most chemical methods do not completely remove organic carbon molecules and additionally generate oxidative byproducts from secondary reactions [36, 21, 114, 128, 20, 40]. Photocatalysts (e.g., titanium dioxide, or TiO_2) have drawn much attention because their oxidizing potential is strong enough to decompose most organic pollutants to carbon dioxide completely [1, 52, 117, 101]; organic compounds degrade on the surface of these catalysts through a series of radical reactions [99]. Nano-sized colloidal photocatalysts are particularly effective for degrading a wide range of organic pollutants in water. However, there are two problems. First, the retrieval of such catalysts is very difficult because of their small particle size [104], and the residual nano-sized catalysts are considered very undesirable due to their potential cytotoxic effects [79]. Second, colloidal instability may significantly reduce catalytic activities, making them inappropriate for long-term use.

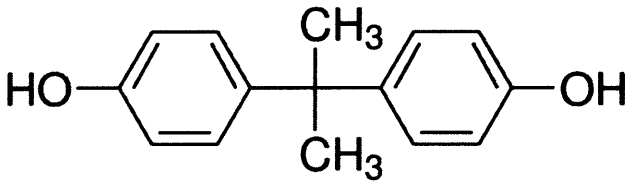

Figure 6-1: **Chemical structure of bisphenol A (BPA).**

To overcome such limitations, a variety of immobilization approaches have been studied. The most widely used supporting material is silicon dioxide (SiO_2) in the

form of gels [129, 19], beads [11], sand [123], and fiber meshes or fabrics [88, 14]. Other materials include microporous cellulose membranes [10], alumina silicate microspheres [94], and zeolites [123, 106, 34, 35]. Unfortunately, despite such diverse attempts, it has been commonly observed that the immobilization process decreases the intrinsic photocatalytic activity of supported catalysts because of reduced active surface area. It has also been reported that photocatalytic activity decreases with increasing adhesion strength of catalyst to the support [104]. Yet, without the strong binding of catalyst to the substrate, the prolonged duration of photocatalysis often leads to the detachment of catalyst from the supporting substrate. Therefore, it is very challenging to develop a technique that can guarantee both long-term structural stability and photocatalytic activity.

Here we show that the layer-by-layer (LbL) assembly technique allows the sufficient binding of a multilayered nano-sized colloidal photocatalyst to a supporting substrate to permit stable photochemical oxidation of organic pollutants in an aqueous phase for long periods. To increase the active catalytic sites exposed to the aqueous reactants, a highly porous electrospun poly(dimethylsiloxane-block-etherimide) (PSEI) nanofiber mesh with high surface area to volume ratio was employed as the supporting substrate (Figure 6-2A) [72]. The adsorption isotherm and photochemical degradation profiles of BPA by the multilayered TiO_2 nanoparticles on electrospun fibers were analyzed and are compared with those of BPA by colloidal TiO_2 nanoparticles. The estrogenic activity of the treated water was measured by assaying the proliferation of a human breast cancer cell line to evaluate the biological effects of the photochemical water treatment.

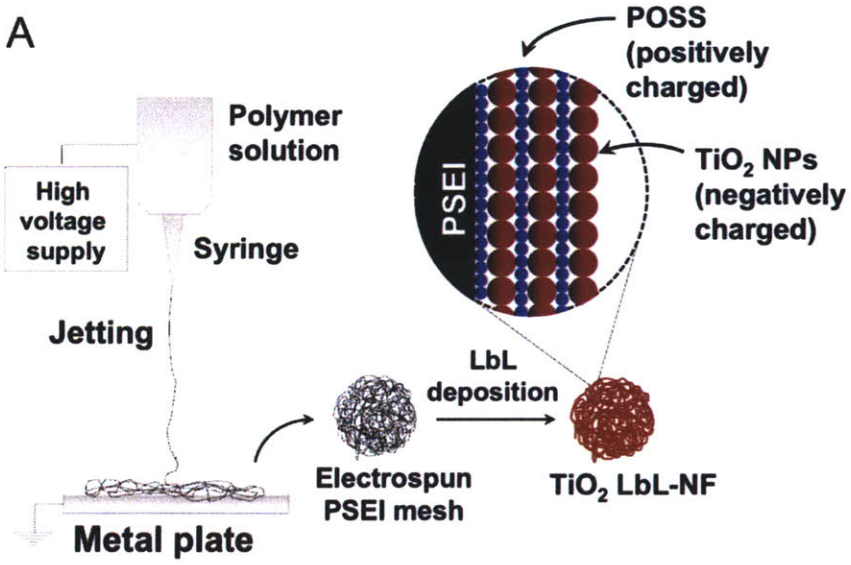

Figure 6-2: **Electrospun PSEI fibers coated with multilayered TiO_2. A**. Schematic of the fabrication of electrospun PSEI fibers deposited with TiO_2 NPs via LbL assembly. **B**, Photographic image of electrospun PSEI nanofiber mats (1) and PSEI nanofiber mats coated with TiO_2 and POSS via LbL assembly (TiO_2 LbL-NF, 2).

6.2 Preparations of TiO_2 LbL nanofibers and TiO_2 colloidal nanoparticles

The PSEI nanofibers were electrospun from 22 wt% solution of PSEI (Gelest) in an 8:2 (v/v) mixture of DMF (source, grade if relevant) and pyridine (source, grade if relevant), using a custom-built parallel plate electrospinning apparatus [110]. The voltage, solution flow rate, and plate-to-plate distance were set to 30 kV, 0.01 mL min^{-1}, and 35 cm, respectively. BET surface areas of electrospun bers were measured with an ASAP 2020 accelerated surface area analyzer (Micromeritics Instrument Co., Norcross). The negatively charged colloidal TiO_2 nanoparticles were synthesized by slowly combining a 1:50 (v/v) mixture of tetrabutyl ammonium hydroxide (Sigma-Aldrich) and ethanol with a 1:6 (v/v) mixture of titanium (IV) isopropoxide (Sigma-Aldrich) and ethanol. The combined solution was then slowly diluted with deionized water to 4 times its original volume under rapid stirring, and refluxed for 2 days at 95°C. The particle size and zeta potential of the colloidal TiO_2 nanoparticles (at pH 10.0) were measured using a Delsa^{TM} Nano C Particle Analyzer (Beckman Coulter), and their crystalline structure was determined using a Rigaku powder X-ray diffractometer. A 10 mM aqueous dipping solution of POSS-$8NH^{3+}8Cl^{-}$ (octa(3-ammoniumpropyl)octasilsesquioxane octachloride, Hybrid Plastics) was prepared with pH 7.5. The pH of the dipping solution and rinsing water was adjusted using 1 N NaOH or HCl prior to LbL assembly. LbL deposition of TiO_2 nanoparticles on electrospun fibers was carried out after plasma treatment of the electrospun fibers for 1 min (Harrick PCD 32G). A Carl Zeiss DS50 programmable slide stainer was used for LbL deposition. An electrostatically bonded coating on fibers was prepared by alternating dipping in POSS-NH^{3+} and TiO_2 solutions. The dipping time in each solution was 30 min, followed by three rinse steps, 1 min for each, in pH adjusted Milli-Q water.

SEM images of electrospun nanofibers were obtained by a JEOL 6320FV field-emission high-resolution SEM instrument. A Kratos Axis Ultra XPS X-ray photoelectron spectroscopy instrument (Kratos Analytical, Manchester) with a monochoromatized Al Kα X-ray source was used to analyze the surface chemistry of the TiO_2 coated nanofibers. The take-off angle relative to the plane of the sample substrate was located at 90^o (data not shown here). TiO_2 LbL nanofibers were embedded in epoxy resin (LR White-Medium Grade, Ladd Research) and microtomed at room temperature into $50 \sim 100$ nm thick sections for TEM analysis. The samples were examined using TEM (JEOL-200 CX).

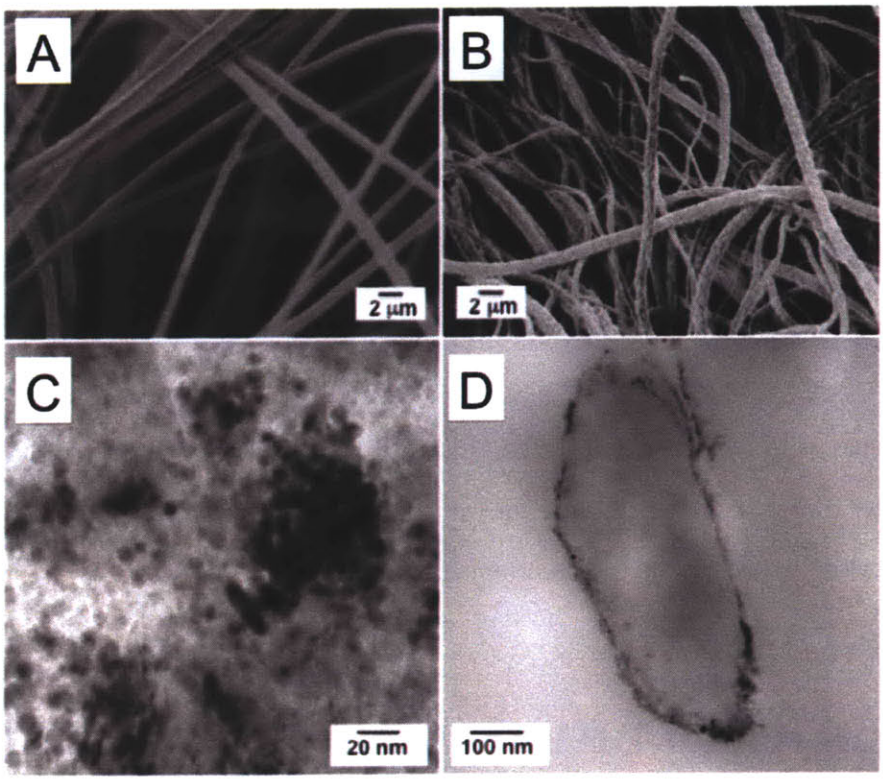

Figure 6-3: **Electron micrographs of TiO_2 LbL nanofibers.** Scanning electron micrographs of A) electrospun PSEI nanofibers and B) TiO_2 LbL-NF. Transmission electron micrograph of C) TiO_2 NPs and D) the cross-section of TiO_2 LbL-NF.

Polymer nanofibers were electrospun from 22 wt% PSEI in a mixture of dimethyl formamide (DMF) and pyridine. PSEI is a random block copolymer containing 35

$\sim$ 40 wt% of siloxane copolymerized with polyetherimide (PEI) units. The siloxane unit provides the nanofibers with flexibility as well as long-term resistance against ultraviolet light and variations in temperature. Figure 6-2B shows photographic images of an electrospun PSEI nanofiber mesh before and after the deposition of colloidal anatase TiO_2 nanoparticles (denoted TiO_2 NPs) . The average diameter of the PSEI fibers is 650 $\pm$ 180 nm, as shown in Figure 6-3A. The surface area was 12 m^2 g^{-1} as determined by Brunauer-Emmett-Teller (BET) analysis using nitrogen gas. Anatase TiO_2 NPs were synthesized via the hydrolysis of titanium (IV) isopropoxide with tetrabutyl ammonium hydroxide. The resulting colloidal particles had a hydrodynamic diameter of about 7 nm with a zeta potential of - 34 mV. A transmission electron microscopy (TEM) image of these TiO_2 NPs is shown in Figure 6-3B. Ten bilayers of negatively charged colloidal TiO_2 nanoparticles and positively charged polyhedral oligomeric silsesquioxanes (POSS) were LbL-assembled on a plasma-treated PSEI nanofiber mesh (denoted TiO_2 LbL-NF). Positively charged POSS was chosen because of its high oxidation resistance and high thermal stability. Scanning and transmission electron micrographs (Figure 6-3C and D) indicated that POSS/TiO_2 layers were uniformly deposited on the PSEI fibers. The amount of TiO_2 on the PSEI was 16.9 μg mg^{-1} or 1.4 mg m^{-2} of the nanofibers, as determined using inductively coupled plasma-atomic emission spectroscopy (ICP-AES) analysis.

6.3 Adsorption of BPA on TiO_2

TiO_2 LbL nanofiber meshes were immersed in Milli-Q water and placed under vacuum at room temperature overnight to remove any gas bubbles entrapped in the electrospun nanofiber mesh. The nanofibers were then incubated with BPA at the concentration of 0.15 to 1 μM in the dark. Colloidal TiO_2 nanoparticles were also incubated with BPA as controls. At pre-determined time intervals, aliquots of the BPA

solution incubated with TiO_2 LbL nanofiber meshes or colloidal TiO_2 nanoparticles were centrifuged at 18,000 × g, and the supernatants were filtered through Centricon filter membranes having a molecular weight cut-off (MWCO) of 3 kDa. The BPA concentration was determined by measuring the absorbance of the filtered supernatant at 278 nm. The experimental data for the adsorption isotherm were analyzed in the form of the double reciprocal of the Langmuir equation, or the Lineweaver-Burk equation:

$$\frac{1}{\Gamma} = \frac{1}{\Gamma_{max}} + \frac{1}{\Gamma_{max} K C} \tag{6.1}$$

where Γ = the amount of BPA adsorbed, Γ_{max} = the maximum amount of BPA adsorbed as the bulk concentration of BPA increases, K = Langmuir equilibrium constant, and C = the bulk concentration of BPA. A plot of Γ^{-1} versus C^{-1} yields a slope of $\Gamma_{max} K^{-1}$ and a y-intercept of $\Gamma_{max} K^{-1}$.

The adsorption isotherm of BPA on TiO_2 NPs exhibited Langmuir-type adsorption, as represented in the Lineweaver-Burk regression of the adsorption isotherm (Figure 6-4). The calculated binding constant (K) was about 0.26 L μmol^{-1}. The maximum amount of BPA adsorbed per unit area of colloidal TiO_2 NPs (Γ_{max}), indicated by the inverse of the y-intercept in Figure 6-4, was 1.1 × 10^{-3} μmol m^{-2}. The TiO_2 LbL-NF also showed Langmuir-type adsorption behavior with $\Gamma_{max} \approx$ 1.3 × 10^{-3} μmol m^{-2}, as calculated using the surface of the nanofibers (12 m^2 g^{-1}) obtained from the BET analysis. This value indicates that one BPA molecule binds per 117 nm^2 of TiO_2 LbL-NF. Hence, the number of sites per unit area on TiO_2 LbL-NF available for the adsorption of BPA is around 1.2 times greater than that on colloidal TiO_2 NPs, despite losing active sites by adsorption. Although there was a marginal increase in the number of adsorption sites in the TiO_2 LbL-NF, BPA bound to TiO_2 LbL-NF with K = 0.58 L μmol^{-1}, which was approximately 2.2 times greater than that of colloidal TiO_2 NPs. Such an increase in binding affinity of BPA to TiO_2

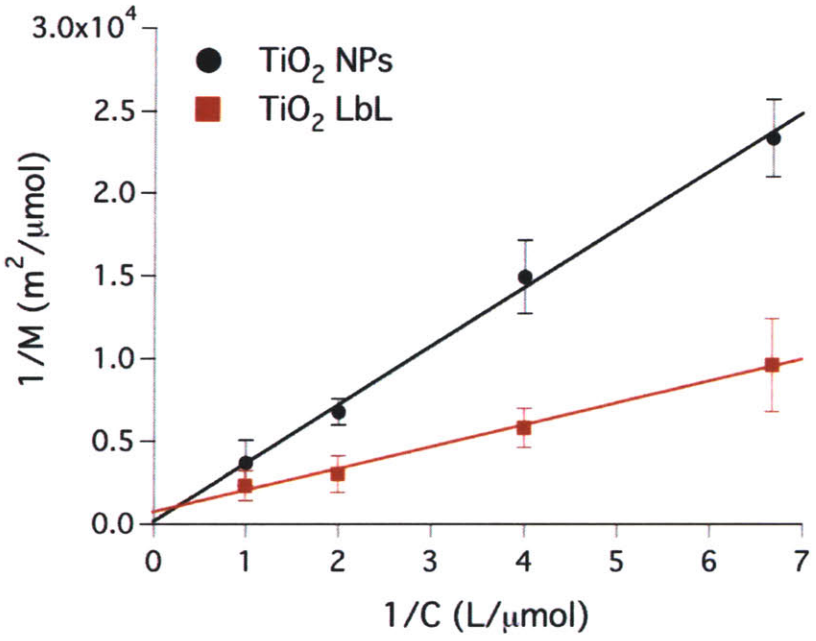

Figure 6-4: **Adsorption of BPA on TiO_2.** Lineweaver-Burk plot of the inverse of the concentration of BPA in solution versus the inverse of the amount of BPA adsorbed on the colloidal TiO_2 NPs (black) and TiO_2 LbL-NF (red). Symbols represent the means and standard deviations ($n = 3 \sim 4$).

LbL-NF implies the existence of additional interactions between BPA and the surface of TiO_2 LbL-NF. It is likely that hydrogen bonds were formed between the protons of the aromatic hydroxyl of BPA and the primary amines of POSS in a similar manner to the hydrogen bonding of phenols to amines [28, 78]. This phenol-NH_3 interaction is a well-known model for proton-coupled electron transfer that can generate organic radicals. Such hydrogen bonding can also decrease the oxidation potential by decreasing the reorganization energy, according to the Marcus theory [28, 80]. This observation has the intriguing implication that the oxidation reaction of BPA can contribute to the persistent generation of phenoxyl radical cations and may lead the conversion of BPA to oxidized forms, such as bisphenol o-quinone, one of the BPA metabolites found *invivo* [5, 111].

6.4 Photocatalytic degradation of BPA

A disc of TiO_2 LbL nanofibers (1.1 cm in diameter, 101.4 μg TiO_2) was pre-treated to remove entrapped gas bubbles and immersed into 20 μM BPA solution in water for BPA adsorption as described above. The TiO_2 LbL nanofiber dish was incubated at ambient temperature for 48 h and was exposed to the AM 1.5G illumination using a solar simulator (SS80B, about 100 mW cm^{-2}, Photo Emission Tech., Inc) for 40 h. AM 1.5G illumination is defined as terrestrial solar spectral irradiance on a surface at 37^o tilt toward the equator, representing a solar spectrum of average conditions in the 48 contiguous states of the United States published by the American Society of Testing and Materials (ASTM). An aliquot of the solution was taken to monitor the concentration of BPA at predetermined time intervals. Following photocatalytic reaction, the used TiO_2 photocatalysts were removed from the solution by centrifugation at 18 $\times$ g followed by filtration (MWCO = 3 kDa, Centricon). The concentration of BPA (Sigma-Aldrich) was determined by HPLC (Agilent 1100 series) equipped with

a C18 reversed-phase column (Nova-Pak C18, 3.9 × 150 mm, Waters). A 6:4 (v/v) mixture of acetonitrile and water was used as an isocratic mobile phase at a rate of 1.0 mL min^{-1}.

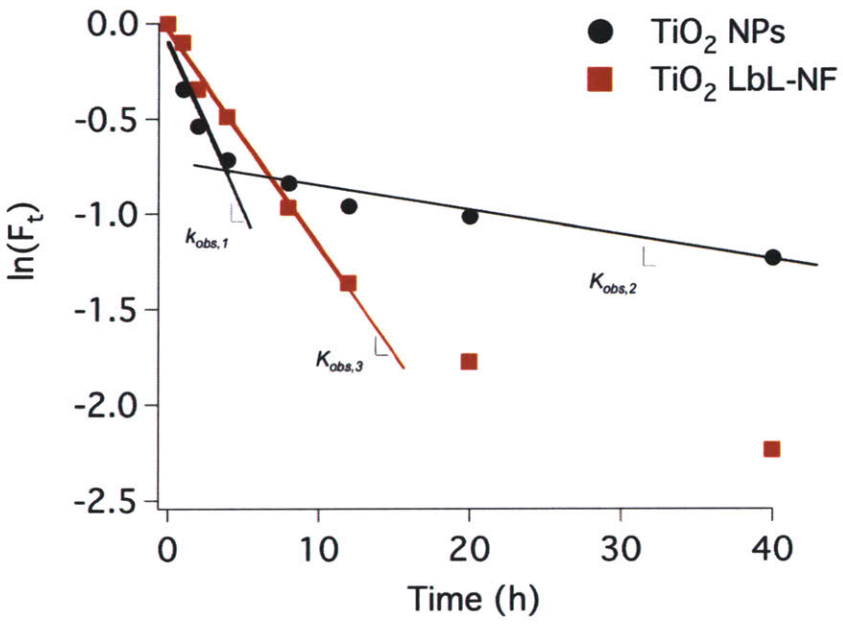

Figure 6-5: **Photodegradation kinetics of BPA by TiO_2.** Photodegradation kinetics of BPA by colloidal TiO_2 NPs (black) and TiO_2 LbL-NF (red) in water. The solid lines represent a linear fit to the experimental data and the slope of the curves indicates the reaction rate constant ($R_1^2 > 0.90$, $R_2^2 > 0.93$, and $R_3^2 > 0.93$).

To evaluate the photocatalytic activities of TiO_2 LbL-NF, the light-induced degradation of BPA in Milli-Q water was monitored using reverse phase high performance liquid chromatography (RP-HPLC). A disc of TiO_2 LbL-NF (1.1 cm in diameter, 101.4 mg TiO_2) was incubated in 20 μM BPA in water for 48 h, followed by the exposure to AM 1.5G illuminations at ambient temperature. An aliquot of the solution was taken to monitor the concentration of BPA at predetermined time intervals. In the absence of TiO_2, only a marginal decrease (about 4 %) of the BPA concentration was observed. Figure 6-5 shows the kinetics of BPA degradation by colloidal TiO_2 nanoparticles and TiO_2 LbL-treated nanofibers, respectively. The time-dependent

relative conversion, Ft, is defined as the ratio of the residual concentration of BPA at time t to the initial BPA concentration at $t = 0$. Colloidal TiO_2 NPs decomposed 70.9 % of BPA within 40 h under irradiation. The BPA degradation followed pseudo-first order kinetics over a certain range of time, as shown in Figure 6-5, and the slope of the linear fit yields the observed degradation rate constant, k_{obs}, based on the equation: $ln(Ft) = - k_{obs}t$. The rate constant for BPA decomposition for the first 4 h of irradiation was $k_{obs,1} \approx 0.84\ h^{-1}$ ($R_1^2 > 0.90$), but in the later stages of photocatalysis it dropped to $k_{obs,2} \approx 0.07\ h^{-1}$ ($R_2^2 > 0.93$). By contrast, TiO_2 LbL-NF exhibited a significantly lower rate constant, $k_{obs,3} \approx 0.15\ h^{-1}$ ($R_3^2 > 0.93$), than colloidal TiO_2 NPs in the early stage of illumination; however, the TiO_2 LbL-NF maintained pseudo-first order kinetics over 12 h, and thus the total decomposition of BPA reached 89.3 %, resulting in an 18.4 % greater degradation of BPA compared to colloidal TiO_2 NPs.

It was hypothesized that the faster loss of the photocatalytic activity in TiO_2 NPs is related to their colloidal instability. Figure 6-6A presents the photographs of the colloidal TiO_2 nanoparticle suspension before and after illumination for 40 h. Precipitation of colloidal TiO_2 NPs was caused by agglomeration induced by photochemical reactions, resulting in a dramatic decrease of surface active sites in colloidal TiO_2 NPs. Particle aggregates were clearly observed using an optical microscope (Figure 6-6B). In contrast, the illumination caused no apparent structural changes of TiO_2 LbL-NF, implying that the TiO_2 multilayer structure prepared via the LbL deposition is stable enough for prolonged photochemical oxidation reactions. Such structural stability may contribute to long-term structural integrity and thus lead to the improvement in overall reaction efficiency. These results suggest that the physical stability of nanoparticle photocatalysts is a critical factor for maintaining catalytic activity over a long period of operation time.

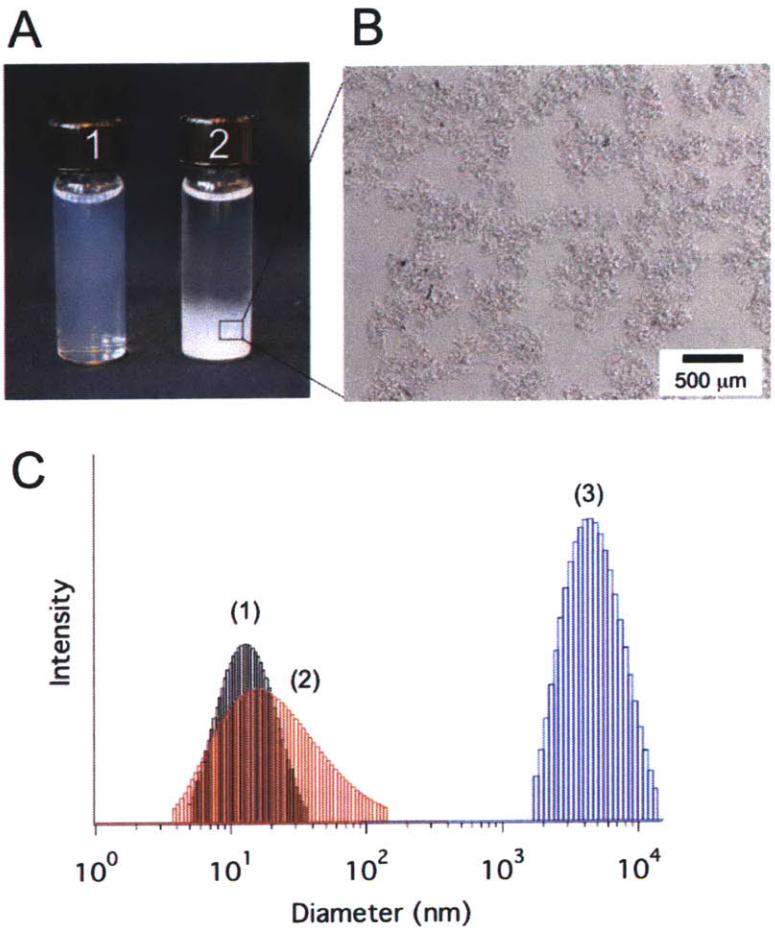

Figure 6-6: **Physical stability of TiO_2 nanoparticles.** **A**, Photographic images of colloidal TiO_2NPs in 20 μM BPA before (1) and after (2) AM 1.5G illumination for 40 h. **B**, Optical microscopic image of colloidal TiO_2 NPs after irradiation. **C**, Size distribution of colloidal TiO_2 NPs as prepared (1), after incubation with 20 μM BPA for 2 days (2), and after illumination for 40 h (3).

6.5 Biological evaluation of the treated BPA solutions

MCF-7 cells were cultured in Dulbeccos Modified Eagles Medium (DMEM) (Gibco, Grand Island, NY) supplemented with 5 % fetal bovine serum (FBS) (Hyclone, Logan, UT), 0.01 % bovine insulin, and penicillin/streptomycin at 37°C in an atmosphere of 5 % CO_2 under saturating humidity. The cells were trypsinized and plated into 24-well plates at the initial cell density of 10^4 cells per well. They were allowed to attach to the well surface for 24 h and then the seeding medium was replaced by phenol red-free DMEM with 5 % charcoal-stripped FBS (Invitrogen) and penicillin/streptomycin. One part of the BPA solutions, treated with the colloidal TiO_2 nanoparticles or the TiO_2 LbL nanofibers under the AM 1.5G illumination for 40 h, was added to 9 parts of the cell medium. Autoclaved Milli-Q water and 20 μM BPA (the final concentration of BPA used was 0.6 μM after dilution with the cell medium) were used as negative and positive controls, respectively. The cell number was determined using a CyQUANT cell proliferation assay kit (Invitrogen).

To verify the biological detoxification of the BPA solution treated with the colloidal TiO_2 NPs or the TiO_2 LbL-NF, the proliferation enhancing effects of the treated BPA solution were determined using a human breast adenocarcinoma cell line, MCF-7 (Figure 6-7). MCF-7 cells have been widely used to test for chemicals and environmental contaminants, including 17β-estradiol, dieldrin, toxaphene, flavonoids, genistein, and kaempferol, because MCF-7 cells express human estrogen receptors (ERs) on their surfaces [113, 77]. Estrogen and estrogen-like molecules can act as an effective mitogen through binding to the ERs, ligand-receptor translocation to the nucleus and dimerization. The ligand-receptor complex dimer can modulate the transcriptional activity of DNA containing palindromic estrogen-responsive elements (EREs), including the immediate early genes *c-myc* and *fos*. Recent studies have

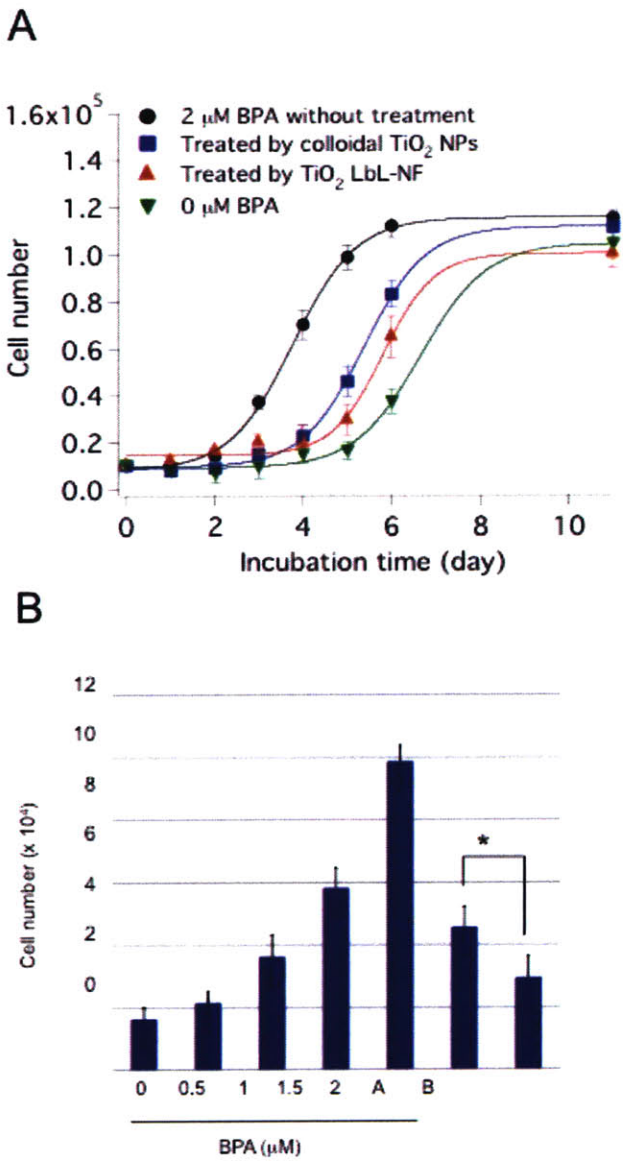

Figure 6-7: **Proliferation enhancing effects of the treated BPA solution determined using MCF-7. A**, Cell proliferation curves of MCF-7. Symbols represent the means and standard deviations (n = 5 $\sim$ 6). **B**, Cell numbers of MCF-7 supplemented by 10% of 0 $\sim$ 20 μM BPA solutions without the treatment and 20 μM BPA solutions treated by colloidal TiO_2 NPs (A) and TiO_2 LbL-NF (B) under AM 1.5G illumination for 40 h. The cell numbers were counted at day 5 of incubation. Asterisk indicates a significant lower estrogenic activity of B relative to A ($p < 0.01$, Students t-test).

shown that ER activation can induce the cytoplasmic signaling cascade of mitogen-activated protein kinases. Therefore, the cell proliferation of MCF-7 can be correlated with the estrogenic activity of BPA. Figure 6-7A compares the proliferation profiles of MCF-7 in the medium supplemented by BPA solutions treated with the colloidal TiO_2 NPs or the TiO_2 LbL-NF for 40 h under AM 1.5G illumination. For the BPA solutions treated by either of the photocatalytic systems, the cell proliferation rates were considerably reduced, compared with the proliferation rate in the untreated BPA solution at the same initial concentration (20 μM, the final concentration used for the cell proliferation experiments was reduced to 2 μM due to the dilution with cell medium). The residual BPA concentrations of the treated solutions were 5.8 $\pm$ 1.1 μM and 2.1 $\pm$ 0.6 μM for the solutions treated with colloidal TiO_2 NPs and the TiO_2 LbL-NF, respectively. Accordingly, the estrogenic activities of the solutions treated with colloidal TiO_2 NPs (A, Figure 6-7B) and the TiO_2 LbL-NF (B, Figure 6-7B) showed approximately 46 % and 29 %, respectively, of the estrogenic activity of the untreated one. Particularly, in comparison with the BPA solution treated with colloidal TiO_2 NPs, the BPA solution treated in the presence of the TiO_2 LbL-NF showed a significantly lower estrogenic activity, indicating that the level of BPA is a determining factor of the estrogenic activities. However, it was also found that the residual BPA concentration was not fully correlated with the estrogenic activities. Figure 6-7B represents the estrogenic activities of the untreated BPA solutions as a function of the BPA concentrations. The BPA solution treated with colloidal TiO_2 NPs for 40 h had about 5.8 μM of the residual BPA; however, the estrogenic activity of the same solution was significantly higher than the untreated 10 μM BPA solution. The BPA solution treated with the TiO_2 LbL-NF for 40 h also exhibited an activity greater than that of 5 μM BPA, despite the much smaller residual concentration of BPA (about 2.1 μM). Another consistent finding was that the solution treated for up to 4 h did not show any significant reduction in the estrogenic activity, although

the actual BPA concentration was apparently reduced as shown in Figure 6-5. We suspect that these results are related to the secondary estrogenic activities of the phenolic intermediates generated as a result of the breakdown of BPA [100]. Identification of such oxidative intermediates is underway in order to clarify the correlation of the biological responses with the water remediation by photocatalytic systems.

6.6 Conclusion

In this chapter, a layer-by-layer technique was employed to immobilize TiO_2 nanoparticles onto porous substrates having high surface area to volume ratio in order to improve the photocatalytic activities for long-term photochemical water remediation. Negatively charged colloidal TiO_2 nanoparticles were directly deposited onto porous electrospun polymer nanofibers using LbL electrostatic assembly with positively charged POSS molecules. This LbL assembly on electrospun nanofibers leads to a stable immobilization of photocatalytic TiO_2 nanoparticless without losing catalytically active sites. The photocatalytic efficiency of the TiO_2 LbL nanofibers to decompose BPA in water was measured and compared with that of colloidal TiO_2 nanoparticles under AM 1.5 illumination. The multilayer-assembled TiO_2 nanofibers exhibited a higher degree of BPA decomposition and maintained the first-order kinetics for over 12 h, while the photocatalytic activities of colloidal TiO_2 nanoparticles was initially greater but quickly decreased due to particle agglomeration. In particular, the adsorption of BPA on TiO_2 LbL-NF is much greater than that on TiO_2 nanoparticles. The additional adsorption sites presented by POSS molecules, which was introduced as the cation for TiO_2 LbL assembly, could explain such increased binding affinity. For the estrogenic activity test based on human breast cancer cell proliferation, the water treated with TiO_2 LbL-NF showed a significantly lower estrogenic activity than the one treated with TiO_2 nanoparticles.

Bibliography

[1] MA Aguado, MA Anderson, and CG HILL. Influence of light-intensity and membrane-properties on the photocatalytic degradation of formic-acid over tio2 ceramic membranes. *J Mol Catal*, 89(1-2):165–178, Jan 1994.

[2] Matthew D Anway, Charles Leathers, and Michael K Skinner. Endocrine disruptor vinclozolin induced epigenetic transgenerational adult-onset disease. *Endocrinology*, 147(12):5515–23, Dec 2006.

[3] Matthew D Anway, Mushtaq A Memon, Mehmet Uzumcu, and Michael K Skinner. Transgenerational effect of the endocrine disruptor vinclozolin on male spermatogenesis. *J Androl*, 27(6):868–79, Jan 2006.

[4] Matthew D Anway and Michael K Skinner. Epigenetic transgenerational actions of endocrine disruptors. *Endocrinology*, 147(6 Suppl):S43–9, Jun 2006.

[5] A Atkinson and D Roy. In vitro conversion of environmental estrogenic chemical bisphenol a to dna binding metabolite(s). *Biochem Biophys Res Commun*, 210(2):424–33, May 1995.

[6] A Atkinson and D Roy. In vivo dna adduct formation by bisphenol a. *Environ Mol Mutagen*, 26(1):60–6, Jan 1995.

[7] S Bahatyrova, RN Frese, KO van der Werf, C Otto, CN Hunter, and JD Olsen. Flexibility and size heterogeneity of the lh1 light harvesting complex revealed by atomic force microscopy - functional significance for bacterial photosynthesis. *J Biol Chem*, 279(20):21327–21333, Jan 2004.

[8] Vincenzo Balzani, Alberto Credi, and Margherita Venturi. Photochemical conversion of solar energy, Jan 2008.

[9] James Barber. Photosynthetic energy conversion: natural and artificial. *Chem Soc Rev*, 38(1):185–96, Jan 2009.

[10] IR Bellobono, M Bonardi, L Castellano, E Selli, and L Righetto. Photosynthetic membranes. 22. energy-conversion efficiency of photoelectrochemical cells employing a titanium-dioxide film anodic membrane and a hydrogen or oxygen cathode. *J Photoch Photobio A*, 66(2):253–258, Jan 1992.

[11] M Bideau, B Claudel, C Dubien, L Faure, and H Kazouan. On the immobilization of titanium-dioxide in the photocatalytic oxidation of spent waters. *J Photoch Photobio A*, 91(2):137–144, Jan 1995.

[12] A Boal, F Ilhan, J DeRouchey, T Thurn-Albrecht, T Russell, and V Rotello. Self-assembly of nanoparticles into structured spherical and network aggregates. *Nature*, 404(6779):746–8, Apr 2000.

[13] Imenne Bouamaied, Leslie-Anne Fendt, Daniel Häussinger, Markus Wiesner, Sandra Thöni, Nicolas Amiot, and Eugen Stulz. Porphyrin-dna: a supramolecular scaffold for functional molecules on the nanometre scale. *Nucleosides Nucleotides Nucleic Acids*, 26(10-12):1533–8, Jan 2007.

[14] V Brezova, A Blazkova, M Breznan, P Kottas, and M Ceppan. Phenol degradation on glass-fibers with immobilized titanium-dioxide particles. *Collect Czech Chem C*, 60(5):788–794, Jan 1995.

[15] Hung-Shu Chang, Matthew D Anway, Stephen S Rekow, and Michael K Skinner. Transgenerational epigenetic imprinting of the male germline by endocrine disruptor exposure during gonadal sex determination. *Endocrinology*, 147(12):5524–41, Dec 2006.

[16] Myung-Seok Choi, Takuzo Aida, Tomoko Yamazaki, and Iwao Yamazaki. Dendritic multiporphyrin arrays as light-harvesting antennae: effects of generation number and morphology on intramolecular energy transfer. *Chemistry (Weinheim an der Bergstrasse, Germany)*, 8(12):2668–78, Jun 2002.

[17] Myung-Seok Choi, Tomoko Yamazaki, Iwao Yamazaki, and Takuzo Aida. Bioinspired molecular design of light-harvesting multiporphyrin arrays. *Angew. Chem. Int. Ed.*, 43(2):150–8, Jan 2004.

[18] George W Crabtree and Nathan S Lewis. Solar energy conversion. *Phys Today*, 60(3):37–42, Jan 2007.

[19] JC Crittenden, Y Zhang, DW Hand, DL Perram, and EG Marchand. Solar detoxification of fuel-contaminated groundwater using fixed-bed photocatalysts. *Water Environ Res*, 68(3):270–278, Jan 1996.

[20] Marie Deborde, Sylvie Rabouan, Patrick Mazellier, Jean-Pierre Duguet, and Bernard Legube. Oxidation of bisphenol a by ozone in aqueous solution. *Water Res*, 42(16):4299–308, Oct 2008.

[21] PB Dorn, CS Chou, and JJ Gentempo. Degradation of bisphenol-a in natural-waters. *Chemosphere*, 16(7):1501–1507, Jan 1987.

[22] Charles Michael Drain. Self-organization of self-assembled photonic materials into functional devices: photo-switched conductors. *Proc. Natl. Acad. Sci. U.S.A.*, 99(8):5178–82, Apr 2002.

[23] Charles Michael Drain, James D Batteas, George W Flynn, Tatjana Milic, Ning Chi, Dalia G Yablon, and Heather Sommers. Designing supramolecular porphyrin arrays that self-organize into nanoscale optical and magnetic materials. *Proc. Natl. Acad. Sci. U.S.A.*, 99 Suppl 2:6498–502, Apr 2002.

[24] Joshua R Dunetz, Claire Sandstrom, Elizabeth R Young, Paul Baker, Steven A Van Name, Terry Cathopolous, Robert Fairman, Julio C de Paula, and Karin S Akerfeldt. Self-assembling porphyrin-modified peptides. *Org Lett*, 7(13):2559–61, Jun 2005.

[25] JS Edmonds, M Nomachi, M Terasaki, M Morita, BW Skelton, and AH White. The reaction of bisphenol a 3,4-quinone with dna. *Biochem Biophys Res Commun*, 319(2):556–561, Jan 2004.

[26] Masayuki Endo, Mamoru Fujitsuka, and Tetsuro Majima. Porphyrin light-harvesting arrays constructed in the recombinant tobacco mosaic virus scaffold. *Chemistry (Weinheim an der Bergstrasse, Germany)*, 13(31):8660–6, Jan 2007.

[27] Masayuki Endo, Mamoru Fujitsuka, and Tetsuro Majima. Porphyrin light-harvesting arrays constructed in the recombinant tobacco mosaic virus scaffold. *Chem-Eur J*, 13(31):8660–8666, Jan 2007.

[28] Y Fang, L Liu, Y Feng, XS Li, and QX Guo. Effects of hydrogen bonding to amines on the phenol/phenoxyl radical oxidation. *Journal of Physical Chemistry A*, 106(18):4669–4678, Jan 2002.

[29] Leslie-Anne Fendt, Imenne Bouamaied, Sandra Thöni, Nicolas Amiot, and Eugen Stulz. Dna as supramolecular scaffold for porphyrin arrays on the nanometer scale. *J. Am. Chem. Soc.*, 129(49):15319–29, Dec 2007.

[30] W Fudickar, J Zimmermann, L Ruhlmann, J Schneider, B Roder, U Siggel, and JH Fuhrhop. Fluorescence quenching and size selective heterodimerization of a porphyrin adsorbed to gold and embedded in rigid membrane gaps. *J. Am. Chem. Soc.*, 121(41):9539–9545, Jan 1999.

[31] Masamichi Fujihira, N Ohshi, and T Osa. Photocell using covalently-bound dyes on semiconductor surfaces. *Nature*, 268(5617):226–228, Jan 1977.

[32] Akira Fujishima and KI Honda. Studies on photosensitive electrode reactions .3. electrochemical evidence for mechanism of primary stage of photosynthesis, Jan 1971.

[33] Akira Fujishima and KI Honda. Electrochemical photolysis of water at a semiconductor electrode. *Nature*, 238(5358):37–8, Jul 1972.

[34] S Fukahori, H Ichiura, T Kitaoka, and H Tanaka. Capturing of bisphenol a photodecomposition intermediates by composite tio2-zeolite sheets. *Appl Catal B-Environ*, 46(3):453–462, Jan 2003.

[35] S Fukahori, H Ichiura, T Kitaoka, and H Tanaka. Photocatalytic decomposition of bisphenol a in water using composite tio2-zeolite sheets prepared by a papermaking technique. *Environ Sci Technol*, 37(5):1048–1051, Jan 2003.

[36] DT Gibson. Microbial degradation of aromatic compounds. *Science*, 161(3846):1093–&, Jan 1968.

[37] Michael Gratzel. Light-induced charge separation and water cleavage in microheterogeneous aqueous systems. *Faraday Discussions of the Chemical Society*, Jan 1980.

[38] Michael Gratzel. Artificial photosynthesis - water cleavage into hydrogen and oxygen by visible-light, Jan 1981.

[39] Harry B Gray and Jay R Winkler. Long-range electron transfer. *Proc. Natl. Acad. Sci. U.S.A.*, 102(10):3534–9, Mar 2005.

[40] Zhaobing Guo and Ruo Feng. Ultrasonic irradiation-induced degradation of low-concentration bisphenol a in aqueous solution. *J Hazard Mater*, 163(2-3):855–60, Apr 2009.

[41] Devens Gust, Thomas A Moore, and Ana L Moore. Solar fuels via artificial photosynthesis, Jan 2009.

[42] Michikazu Hara, JT Lean, and Thomas E Mallouk. Photocatalytic oxidation of water by silica-supported tris(4,4 '-dialkyl-2,2 '-bipyridyl)ruthenium polymeric sensitizers and colloidal iridium oxide. *Chem. Mater.*, 13(12):4668–4675, Jan 2001.

[43] Michikazu Hara and Thomas E Mallouk. Photocatalytic water oxidation by nafion-stabilized iridium oxide colloids. *Chemical Communications*, (19):1903–1904, Jan 2000.

[44] Michikazu Hara, CC Waraksa, JT Lean, BA Lewis, and Thomas E Mallouk. Photocatalytic water oxidation in a buffered tris(2,2 '-bipyridyl)ruthenium complex-colloidal iro2 system. *Journal of Physical Chemistry A*, 104(22):5275–5280, Jan 2000.

[45] Anthony Harriman, GS Nahor, S Mosseri, and P Neta. Iridium oxide hydrosols as catalysts for the decay of zinc porphyrin radical cations in water. *Journal of the Chemical Society*, Jan 1988.

[46] Anthony Harriman, IJ Pickering, and JM Thomas. Metal oxides as heterogeneous catalysts for oxygen evolution under photochemical conditions. *Journal of the Chemical Society*, Jan 1988.

[47] Taku Hasobe. Supramolecular nanoarchitectures for light energy conversion, Jan 2010.

[48] Taku Hasobe, Prashant V Kamat, Vincent Troiani, Nathalie Solladié, Tae Kyu Ahn, Seong Keun Kim, Dongho Kim, Anusorn Kongkanand, Susumu Kuwabata, and Shunichi Fukuzumi. Enhancement of light-energy conversion efficiency by multi-porphyrin arrays of porphyrin-peptide oligomers with fullerene clusters. *The journal of physical chemistry B*, 109(1):19–23, Jan 2005.

[49] V Hausser and H Staab. Cyclic cleavage of water into h2 and o2 by visible light with coupled redox catalysts [**'. *Chimia*, Jan 1979.

[50] Paul G Hoertz, Yeong-Il Kim, W. Justin Youngblood, and Thomas E Mallouk. Bidentate dicarboxylate capping groups and photosensitizers control the size of iro2 nanoparticle catalysts for water oxidation. *The journal of physical chemistry B*, 111(24):6845–56, Jun 2007.

[51] Paul G Hoertz and Thomas E Mallouk. Light-to-chemical energy conversion in lamellar solids and thin films. *Inorganic chemistry*, 44(20):6828–40, Oct 2005.

[52] MR Hoffmann, ST Martin, Wonyong Choi, and DW Bahnemann. Environmental applications of semiconductor photocatalysis, Jan 1995.

[53] P Horton, A. V Ruban, and R. G Walters. Regulation of light harvesting in green plants (indication by nonphotochemical quenching of chlorophyll fluorescence). *Plant Physiol*, 106(2):415–420, Oct 1994.

[54] KL Howdeshell, PH Peterman, BM Judy, JA Taylor, CE Orazio, RL Ruhlen, Frederick S vom Saal, and WV Welshons. Bisphenol a is released from used polycarbonate animal cages into water at room temperature. *Environ Health Persp*, 111(9):1180–1187, Jan 2003.

[55] Yu Huang, Chung-Yi Chiang, Soo Kwan Lee, Yan Gao, Evelyn L Hu, James De Yoreo, and Angela Belcher. Programmable assembly of nanoarchitectures using genetically engineered viruses. *Nano. Lett.*, 5(7):1429–34, Jul 2005.

[56] H Ishibashi, N Watanabe, N Matsumura, M Hirano, Y Nagao, H Shiratsuchi, S Kohra, S Yoshihara, and K Arizono. Toxicity to early life stages and an estrogenic effect of a bisphenol a metabolite, 4-methyl-2,4-bis(4-hydroxyphenyl)pent-1-ene on the medaka (oryzias latipes). *Life Sci*, 77(21):2643–2655, Jan 2005.

[57] Alberto Izzotti, Stefano Kanitz, Francesco D'Agostini, Anna Camoirano, and Silvio De Flora. Formation of adducts by bisphenol a, an endocrine disruptor, in dna in vitro and in liver and mammary tissue of mice. *Mutat Res-Gen Tox En*, 679(1-2):28–32, Jan 2009.

[58] Kuppuswamy Kalyanasundaram, J Kiwi, and Michael Gratzel. Hydrogen evolution from water by visible-light, a homogeneous 3 component test system for redox catalysis. *Helv Chim Acta*, 61(7):2720–2730, Jan 1978.

[59] H Kawahata, H Ohta, M Inoue, and A Suzuki. Endocrine disrupter nonylphenol and bisphenol a contamination in okinawa and ishigaki islands, japan - within coral reefs and adjacent river mouths. *Chemosphere*, 55(11):1519–1527, Jan 2004.

[60] Ahmad S Khalil, Jorge M Ferrer, Ricardo R Brau, Stephen T Kottmann, Christopher J Noren, Matthew J Lang, and Angela Belcher. Single m13 bacteriophage tethering and stretching. *Proc. Natl. Acad. Sci. U.S.A.*, 104(12):4892–7, Mar 2007.

[61] Shahed U M Khan, Mofareh Al-Shahry, and William B Ingler. Efficient photochemical water splitting by a chemically modified n-tio2. *Science*, 297(5590):2243–5, Sep 2002.

[62] O Khaselev and John A Turner. A monolithic photovoltaic-photoelectrochemical device for hydrogen production via water splitting. *Science*, 280(5362):425–7, Apr 1998.

[63] J Kiwi, E Borgarello, E Pelizzetti, M Visca, and Michael Gratzel. Cyclic water cleavage by visible-light - drastic improvement of yield of h2 and o2 with bifunctional redox catalysts, Jan 1980.

[64] J Kiwi and Michael Gratzel. Oxygen evolution from water via redox catalysis, Jan 1978.

[65] J Kiwi and Michael Gratzel. Colloidal redox catalysts for evolution of oxygen and for light-induced evolution of hydrogen from water, Jan 1979.

[66] J Kiwi and Michael Gratzel. Hydrogen evolution from water induced by visible light mediated by redox catalysis. *Nature*, Jan 1979.

[67] J Kiwi, Michael Gratzel, and G Blondeel. Water oxidation to oxygen by cerium(iv) ions mediated by ruthenium dioxide catalyst. *J Chem Soc Dalton*, (10):2215–2216, Jan 1983.

[68] Bashkim Kokona, Andrew M Kim, R. Claire Roden, Joshua P Daniels, Brian J Pepe-Mooney, Brian C Kovaric, Julio C de Paula, Karl A Johnson, and Robert Fairman. Self assembly of coiled-coil peptide-porphyrin complexes. *Biomacromolecules*, 10(6):1454–9, Jun 2009.

[69] Anusorn Kongkanand, Rebeca Martínez Domínguez, and Prashant V Kamat. Single wall carbon nanotube scaffolds for photoelectrochemical solar cells. capture and transport of photogenerated electrons. *Nano. Lett.*, 7(3):676–80, Mar 2007.

[70] Brian C Kovaric, Bashkim Kokona, Alexander D Schwab, Margaret A Twomey, Julio C de Paula, and Robert Fairman. Self-assembly of peptide porphyrin complexes: toward the development of smart biomaterials. *J. Am. Chem. Soc.*, 128(13):4166–7, Apr 2006.

[71] DA LaVan and JN Cha. Approaches for biological and biomimetic energy conversion. *Proc. Natl. Acad. Sci. U.S.A.*, 103(14):5251–5255, Jan 2006.

[72] Jung Ah Lee, Kevin C Krogman, Minglin Ma, Randal M Hill, Paula T Hammond, and Gregory C Rutledge. Highly reactive multilayer-assembled tio2 coating on electrospun polymer nanofibers. *Adv. Mater.*, 21(12):1252–+, Jan 2009.

[73] Seung-Wuk Lee, Chuanbin Mao, Christine E Flynn, and Angela Belcher. Ordering of quantum dots using genetically engineered viruses. *Science*, 296(5569):892–5, May 2002.

[74] Soo-Kwan Lee, Dong Soo Yun, and Angela Belcher. Cobalt ion mediated self-assembly of genetically engineered bacteriophage for biomimetic co-pt hybrid material. *Biomacromolecules*, 7(1):14–7, Jan 2006.

[75] Yun Jung Lee, Hyunjung Yi, Woo-Jae Kim, Kisuk Kang, Dong Soo Yun, Michael S Strano, Gerbrand Ceder, and Angela Belcher. Fabricating genetically engineered high-power lithium-ion batteries using multiple virus genes. *Science*, 324(5930):1051–5, May 2009.

[76] Mitch Leslie. Origins. on the origin of photosynthesis. *Science*, 323(5919):1286–7, Mar 2009.

[77] Xiang-Ming Li, Fang-Ni Luo, Gul-Xia Liu, and Ping-Ting Zhu. Bioassay of estrogenic activity of effluent and influent in a farm wastewater treatment plant using an in vitro recombinant assay with yeast cells. *Biomed Environ Sci*, 21(5):381–388, Jan 2008.

[78] Yun-Xiang Lu, Jian-Wei Zou, Zhi-Min Jin, Yan-Hua Wang, Hua-Xin Zhang, Yong-Jun Jiang, and Qing-Sen Yu. Proton exchanges between phenols and ammonia or amines: A computational study. *Journal of Physical Chemistry A*, 110(29):9261–9266, Jan 2006.

[79] Arnaud Magrez, Lenke Horváth, Rita Smajda, Valérie Salicio, Nathalie Pasquier, László Forró, and Beat Schwaller. Cellular toxicity of tio2-based nanofilaments. *ACS Nano*, 3(8):2274–80, Aug 2009.

[80] T Maki, Yoko Araki, Y Ishida, O Onomura, and Y Matsumura. Construction of persistent phenoxyl radical with intramolecular hydrogen bonding. *J. Am. Chem. Soc.*, 123(14):3371–3372, Jan 2001.

[81] Stephen Mann. Molecular recognition in biomineralization, Jan 1988.

[82] Stephen Mann. Molecular tectonics in biomineralization and biomimetic materials chemistry, Jan 1993.

[83] Stephen Mann. Biomineralization and biomimetic materials chemistry. *Journal of Materials Chemistry*, 5(7):935–946, Jan 1995.

[84] Stephen Mann, DD Archibald, JM Didymus, Trevor Douglas, BR Heywood, FC Meldrum, and NJ Reeves. Crystallization at inorganic-organic interfaces - biominerals and biomimetic synthesis. *Science*, 261(5126):1286–1292, Jan 1993.

[85] Chuanbin Mao, Christine E Flynn, Andrew Hayhurst, Rozamond Sweeney, Jifa Qi, George Georgiou, Brent L Iverson, and Angela Belcher. Viral assembly of oriented quantum dot nanowires. *Proc. Natl. Acad. Sci. U.S.A.*, 100(12):6946–51, Jun 2003.

[86] Chuanbin Mao, Daniel J Solis, Brian D Reiss, Stephen T Kottmann, Rozamond Y Sweeney, Andrew Hayhurst, George Georgiou, Brent L Iverson, and Angela Belcher. Virus-based toolkit for the directed synthesis of magnetic and semiconducting nanowires. *Science*, 303(5655):213–7, Jan 2004.

[87] T Markvart and PT Landsberg. Thermodynamics and reciprocity of solar energy conversion, Jan 2002.

[88] M Mikula, V Brezova, M Ceppan, L Pach, and L KARPINSKY. Comparison of photocatalytic activity of sol-gel tio2 and p25 tio2 particles supported on commercial fiberglass fabric. *J Mater Sci Lett*, 14(9):615–616, Jan 1995.

[89] Rebekah A Miller, Andrew D Presley, and Matthew B Francis. Self-assembling light-harvesting systems from synthetically modified tobacco mosaic virus coat proteins. *J. Am. Chem. Soc.*, 129(11):3104–9, Mar 2007.

[90] Gopal K Mor, Haripriya E Prakasam, Oomman K Varghese, Karthik Shankar, and Craig A Grimes. Vertically oriented ti-fe-o nanotube array films: toward a useful material architecture for solar spectrum water photoelectrolysis. *Nano. Lett.*, 7(8):2356–64, Aug 2007.

[91] Gopal K Mor, Karthik Shankar, Maggie Paulose, Oomman K Varghese, and Craig A Grimes. Enhanced photocleavage of water using titania nanotube arrays. *Nano. Lett.*, 5(1):191–195, Jan 2005.

[92] ND Morris, M Suzuki, and Thomas E Mallouk. Kinetics of electron transfer and oxygen evolution in the reaction of [ru(bpy)(3)](3+) with colloidal iridium oxide. *Journal of Physical Chemistry A*, 108(42):9115–9119, Jan 2004.

[93] GS Nahor, S Mosseri, P Neta, and Anthony Harriman. Polyelectrolyte-stabilized metal-oxide hydrosols as catalysts for the photooxidation of water by zinc porphyrins. *J Phys Chem-Us*, 92(15):4499–4504, Jan 1988.

[94] M Nair, ZH Luo, and A Heller. Rates of photocatalytic oxidation of crude-oil on salt-water on buoyant, cenosphere-attached titanium-dioxide. *Ind Eng Chem Res*, 32(10):2318–2323, Jan 1993.

[95] Ki Tae Nam, Dong-Wan Kim, Pil J Yoo, Chung-Yi Chiang, Nonglak Meethong, Paula T Hammond, Yet-Ming Chiang, and Angela Belcher. Virus-enabled synthesis and assembly of nanowires for lithium ion battery electrodes. *Science*, 312(5775):885–8, May 2006.

[96] Ki Tae Nam, Yun Jung Lee, Eric M Krauland, Stephen T Kottmann, and Angela Belcher. Peptide-mediated reduction of silver ions on engineered biological scaffolds. *ACS Nano*, 2(7):1480–1486, Jan 2008.

[97] Ki Tae Nam, Ryan Wartena, Pil J Yoo, Forrest W Liau, Yun Jung Lee, Yet-Ming Chiang, Paula T Hammond, and Angela Belcher. Stamped microbattery electrodes based on self-assembled m13 viruses. *Proc. Natl. Acad. Sci. U.S.A.*, 105(45):17227–31, Nov 2008.

[98] P Neta, P Hambright, A Thompson Jr, and Anthony Harriman. ... photooxidation of water to oxygen on the surface of colloidal iridium oxides: photochemical and .... *The Journal of Physical Chemistry*, Jan 1989.

[99] Kei Nomiyama, Teiji Tanizaki, Koji Arizono, and Ryota Shinohara. Endocrine effects generated by photooxidation of coplanar biphenyls in water using titanium dioxide. *Chemosphere*, 66(6):1138–1145, Jan 2007.

[100] Kei Nomiyama, Teiji Tanizaki, Toyokazu Koga, Koji Arizono, and Ryota Shinohara. Oxidative degradation of bpa using tio2 in water, and transition of estrogenic activity in the degradation pathways. *Arch Environ Con Tox*, 52(1):8–15, Jan 2007.

[101] Y Ohko, I Ando, C Niwa, T Tatsuma, T Yamamura, T Nakashima, Y Kubota, and Akira Fujishima. Degradation of bisphenol a in water by tio2 photocatalyst. *Environ Sci Technol*, 35(11):2365–2368, Jan 2001.

[102] Shinsuke Okada and Hiroshi Segawa. Substituent-control exciton in j-aggregates of protonated water-insoluble porphyrins. *J. Am. Chem. Soc.*, 125(9):2792–6, Mar 2003.

[103] T Osa and Masamichi Fujihira. Photocell using covalently-bound dyes on semiconductor surfaces. *Nature*, 264(5584):349–350, Jan 1976.

[104] RL Pozzo, MA Baltanas, and AE Cassano. Supported titanium oxide as photocatalyst in water decontamination: State of the art. *Catal Today*, 39(3):219–231, Jan 1997.

[105] Grzegorz Raszewski, Wolfram Saenger, and Thomas Renger. Theory of optical spectra of photosystem ii reaction centers: location of the triplet state and the identity of the primary electron donor. *Biophys. J.*, 88(2):986–98, Feb 2005.

[106] EP Reddy, L Davydov, and P Smirniotis. Tio2-loaded zeolites and mesoporous materials in the sonophotocatalytic decomposition of aqueous organic pollutants: the role of the support, Jan 2003.

[107] A William Rutherford and Thomas A Moore. Mimicking photosynthesis, but just the best bits. *Nature*, 453(7194):449, May 2008.

[108] C Sanchez, H Arribart, and MMG Guille. Biomimetism and bioinspiration as tools for the design of innovative materials and systems, Jan 2005.

[109] Luigi Monsu Scolaro, Maria Angela Castriciano, Andrea Romeo, Norberto Micali, Nicola Angelini, Carla Lo Passo, and Franco Felici. Supramolecular binding of cationic porphyrins on a filamentous bacteriophage template: toward a noncovalent antenna system. *J. Am. Chem. Soc.*, 128(23):7446–7, Jun 2006.

[110] YM Shin, MM Hohman, MP Brenner, and GC Rutledge. Experimental characterization of electrospinning: the electrically forced jet and instabilities. *Polymer*, 42(25):9955–9967, Jan 2001.

[111] Martin Sjödin, Tania Irebo, Josefin E Utas, Johan Lind, Gabor Merényi, Björn Akermark, and Leif Hammarström. Kinetic effects of hydrogen bonds on proton-coupled electron transfer from phenols. *J. Am. Chem. Soc.*, 128(40):13076–83, Oct 2006.

[112] Michael K Skinner and Matthew D Anway. Seminiferous cord formation and germ-cell programming: epigenetic transgenerational actions of endocrine disruptors. *Ann N Y Acad Sci*, 1061:18–32, Dec 2005.

[113] A M Soto, C Sonnenschein, K L Chung, M F Fernandez, N Olea, and F O Serrano. The e-screen assay as a tool to identify estrogens: an update on estrogenic environmental pollutants. *Environ Health Persp*, 103 Suppl 7:113–22, Oct 1995.

[114] J Spivack, T K Leib, and J H Lobos. Novel pathway for bacterial metabolism of bisphenol a. rearrangements and stilbene cleavage in bisphenol a metabolism. *J Biol Chem*, 269(10):7323–9, Mar 1994.

[115] G Steinberg-Yfrach, J L Rigaud, E N Durantini, Ana L Moore, Devens Gust, and Thomas A Moore. Light-driven production of atp catalysed by f0f1-atp synthase in an artificial photosynthetic membrane. *Nature*, 392(6675):479–82, Apr 1998.

[116] Ranitendranath Tagore, Robert H Crabtree, and Gary W Brudvig. Oxygen evolution catalysis by a dimanganese complex and its relation to photosynthetic water oxidation. *Inorganic chemistry*, 47(6):1815–23, Mar 2008.

[117] P Théron, P Pichat, C Petrier, and C Guillard. Water treatment by tio2 photocatalysis and/or ultrasound: degradations of phenyltrifluoromethylketone, a trifluoroacetic-acid-forming pollutant, and octan-1 -ol, a very hydrophobic pollutant. *Water Sci Technol*, 44(5):263–70, Jan 2001.

[118] Laura N Vandenberg, Russ Hauser, Michele Marcus, Nicolas Olea, and Wade V Welshons. Human exposure to bisphenol a (bpa). *Reprod Toxicol*, 24(2):139–77, Jan 2007.

[119] Laura N Vandenberg, Maricel V Maffini, Cheryl M Schaeberle, Angelo A Ucci, Carlos Sonnenschein, Beverly S Rubin, and Ana M Soto. Perinatal exposure to the xenoestrogen bisphenol-a induces mammary intraductal hyperplasias in adult cd-1 mice. *Reprod Toxicol*, 26(3-4):210–9, Jan 2008.

[120] Laura N Vandenberg, Maricel V Maffini, Carlos Sonnenschein, Beverly S Rubin, and Ana M Soto. Bisphenol-a and the great divide: a review of controversies in the field of endocrine disruption. *Endocr Rev*, 30(1):75–95, Feb 2009.

[121] Laura N Vandenberg, Maricel V Maffini, Perinaaz R Wadia, Carlos Sonnenschein, Beverly S Rubin, and Ana M Soto. Exposure to environmentally relevant doses of the xenoestrogen bisphenol-a alters development of the fetal mouse mammary gland. *Endocrinology*, 148(1):116–27, Jan 2007.

[122] Wade V Welshons, Susan C Nagel, and Frederick S vom Saal. Large effects from small exposures. iii. endocrine mechanisms mediating effects of bisphenol a at levels of human exposure. *Endocrinology*, 147(6 Suppl):S56–69, Jun 2006.

[123] YM Xu and CH Langford. Enhanced photoactivity of a titanium(iv) oxide-supported on zsm5 and zeolite-a at low-coverage. *J Phys Chem-Us*, 99(29):11501–11507, Jan 1995.

[124] Masayuki Yagi, Y Takahashi, I Ogino, and M Kaneko. Dioxygen evolution induced by visible light at layered sensitizer water oxidation catalyst. *J Chem Soc Faraday T*, 93(17):3125–3127, Jan 1997.

[125] Shin'ichi Yoshihara, Tohru Mizutare, Misako Makishima, Noriko Suzuki, Nariaki Fujimoto, Kazuo Igarashi, and Shigeru Ohta. Potent estrogenic metabolites of bisphenol a and bisphenol b formed by rat liver s9 fraction: their structures and estrogenic potency. *Toxicol Sci*, 78(1):50–9, Mar 2004.

[126] W. Justin Youngblood, Seung-Hyun Anna Lee, Yoji Kobayashi, Emil A Hernandez-Pagan, Paul G Hoertz, Thomas A Moore, Ana L Moore, Devens Gust, and Thomas E Mallouk. Photoassisted overall water splitting in a visible light-absorbing dye-sensitized photoelectrochemical cell. *J. Am. Chem. Soc.*, 131(3):926–7, Jan 2009.

[127] Hongtao Yu, Xie Quan, Shuo Chen, and Huimin Zhao. Tio2-multiwalled carbon nanotube heterojunction arrays and their charge separation capability. *J Phys Chem C*, 111(35):12987–12991, Jan 2007.

[128] Chang Zhang, Guangming Zeng, Li Yuan, Jian Yu, Jianbing Li, Guohe Huang, Beidou Xi, and Hongliang Liu. Aerobic degradation of bisphenol a by achromobacter xylosoxidans strain b-16 isolated from compost leachate of municipal solid waste. *Chemosphere*, 68(1):181–90, May 2007.

[129] Y Zhang, JC Crittenden, DW Hand, and DL Perram. Fixed-bed photocatalysts for solar decontamination of water. *Environ Sci Technol*, 28(3):435–442, Jan 1994.

Appendix A

Conjugation of zinc porphyrins to M13 viruses

The following protocol shows a typical conjugation condition that was used for M13KE and IrO_2-binding M13 viruses.

1. Dehydrate dimethyl sulfoxide (DMSO) using molecular sieves (3 Å). This step is important in increasing the conjugation efficiency by preventing a hydrolytic reverse reaction.

2. Dissolve fresh ZnDPEG (Zn(II) deuteroporphyrin IX-2,4-bis ethylene glycol, or 8,13-bis(1,2 dihydroxyethyl)-3,7,12,17-tetramethyl-21H,23H-porphine- 2,18-dipropionic acid zinc(II), Frontier Scientific, Inc.) at a concentration of 8 mM in anhydrous DMSO. We usually purchased 25 mg ZnDPEG from Frontier Scientific, Inc., http://www.frontiersci.com/, catalog No. ZnD630-9, Formula Weight 694.04).

3. Prepare 10 mM N,N'-dicyclohexylcarbodiimide (DCC, Sigma-Aldrich) by dissolving 50 mg DCC in 24.2 mL anhydrous DMSO.

4. Prepare 10 mM N-hydroxysuccinimide (NHS, Sigma-Aldrich) by dissolving 26 mg NHS in 22.4 mL anhydrous DMSO.

5. Preactivate carboxylic acids in ZnDPEG (0.5 mM) by incubating with 1 mM DCC and 1 mM NHS in anhydrous DMSO for 1 h at room temperature. Mix the following solutions.

   (a) 11.8 mL DMSO

   (b) 1 mL 8 mM ZDPEG in DMSO

   (c) 1.6 mL 10 mM DCC in DMSO

   (d) 1.6 mL 10 mM NHS in DMSO

6. Add the activated ZnDPEG to a virus suspension in 1 mM phosphate-buffered saline (PBS, pH 7.4) and incubated for 15 h with magnetic stirring at about 100 rpm. The virus concentration was usually 10^{10} pfu μL^{-1} as determined by the standard bacteriophage titer analysis. The detailed procedures are available at the New England Biolabs website (http://www.neb.com).

7. Centrifuge the reaction mixture at 8,000 rpm for 2 min to remove the insoluble urea byproducts.

8. Remove the unreacted ZnDPEG via dialysis (Spectra/Por membrane 4, molecular cut-off: $12 \sim 14$ kDa, Spectrum, Rancho Dominguez, CA) against excess amount of deionized water in the dark for 2 days.

Appendix B

One Liter-Scale Amplification of M13 Viruses

1. **Amplification**

   (a) Start an overnight *E.coli* culture. Pick a colony from an ER2738 [1] LB-agar plate and disperse it in 50 mL LB-Tet medium. Use a blue tip for picking. Don't use the plate unless it was prepared within a couple of months. Use an orbital shaker at 250 rpm, 37°C.

   (b) Autoclave 1 L of LB medium (dissolve 25 g in 1 L Milli-Q water). Use a > 2 L flask for vigorous shaking.

   (c) Dilute the overnight culture by mixing 5 ml the culture with 45 ml fresh LB. You can adjust the optical density of the culture to 0.5 at 600 nm. This corresponds to 5 x 10^8 cells/mL (= 2.5 × 10^{10} cells for 50 mL culture).

   (d) Inoculate the culture with 500 μL of 3.5 x 10^7 pfu/μL and then incubate it for 4 hrs.

   (e) Cool the autoclaved LB medium below to 70°C and then add 1 mL of 1,000× tetracycline (20 mg/ml in methanol. Store at -20°C in the dark. Vortex before use.

   (f) Further cool the LB-tet medium < 37°C.

   (g) Pour the culture into 1 L autoclaved LB-Tet medium.

   (h) Incubate for about 20 h. Use an orbital shaker at 250 rpm, 37°C.

   (i) Autoclave 6 of 500 mL polypropylene centrifuge bottles and 8 of 500 ml polycarbonate centrifuge bottles at 121°C for 15 min.

   (j) Stand the culture without agitation for 20 min.

   (k) Spin down the culture at 9 × g for 15 min.

   (l) Transfer the supernatant to autoclaved polycarbonate centrifuge bottles. Use 300 ~ 350 mL per bottle.

[1] New England Biolabs

(m) Add 1 part of PEG/NaCl to 6 parts of the supernatant. PEG/NaCl: 20% (w/v) polyethylene glycol 8,000, 2.5 M NaCl. Autoclave. Store at room temperature.

(n) Incubate at 4^oC for 2 days.

(o) Take 4 bottles out of the refrigerator.

(p) Spin down the phage at 16 × g for 20 min. Remove the supernatant as much as possible.

(q) Add 50 mL PBS to a bottle and vortex it. TBS: 50 mM Tris-HCl (pH 7.5), 150 mM NaCl, Autoclave. Store at room temperature.

(r) Transfer the solution to another bottle. Repeat it until you get the solution in the last bottle.

(s) Repeat the dissolution procedures twice so that you get about 150 mL solution in the last bottle.

(t) Take the rest 4 bottles out of the refrigerator.

(u) Repeat the dissolution procedures twice so that you get about 150 mL solution in the last bottle.

(v) Combine two bottles into one.

(w) Add 1 part of PEG/NaCl solution to 6 parts of the supernatant.

(x) Incubate at 4^oC for 1 day.

(y) Spin down the phage at 16 × g for 20 min. Remove the supernatant as much as possible. Add 50 mL PBS and vortex it.

(z) Add 150 mL buffer and filtrate the virus solution through 0.45 μm membrane filter to remove residual bacteria.

2. **Titration**

(a) Start 10 mL *E. coli* culture.

(b) Place 4 LB-agar (IPTG/X-gal/Tet) plates at 37^oC incubator.

(c) Put agarose top into 80^oC oven for a couple of hrs. Note that 5 mL is necessary for each plate.

(d) Remove the agarose top from the oven and keep it at 50^oC oven.

(e) Prepare the dilutions of phages in eppendorf tubes. Note that you must thoroughly mix the phages between dilutions.

(f) Check the O.D. of E. coli culture. $\text{Abs}_{600nm} = 0.5$. Transfer 190 μl culture to an EP tube.

(g) Add 10 μL phage dilutions to each tube.

(h) 5 min incubation.

(i) Prepare

i. 15 mL Falcon tubes

ii. Phage + E.coli in EP tubes

iii. LB-agar (IPTG/X-gal/Tet) plates

iv. Agarose top

v. Pipetman (200 μL and pipet aid)

(j) Add 5 mL agarose top into 15 mL Falcon tubes.

(k) Add 200 μL of a phage + *E.coli* mixture.

(l) Vortex.

(m) Pour on LB-agar (IPTG/X-gal/Tet) plates.

(n) Label.

(o) Wait for about 30 min until the plate is completely sodified.

(p) Incubate at 37°C overnight.

Appendix C

Synthesis of Colloidal Iridium Oxide Nanoparticles

Iridium oxide hydrosols can be prepared by hydrolyzing hexachloroiridate (III) or (IV) by a chemical method. This protocol is basically based on Harriman *et al.* (1988) published in *J. Chem. Soc., Faraday Trans.* **84**: 2821 - 2829.

1. Prepare an oil bath equilibrated at 90°C.
2. Clean a 500 mL Pyrex glass bottle and a magnetic bar thoroughly (with ethanol and deionized water).
3. Add 500 mg sodium citrate dihydrate (Mallinckrodt Chemicals, AR ACS grade, 99.0%, VWR catalog No. MK075412 or MK075406).
4. Add 200 mL deionized water pre-equilibrated at 80°C at least overnight.
5. Dissolve 300 mg sodium hexachloroiridate(IV) hexahydrate, $Na_2IrCl_6 \cdot 6H_2O$, (Alfa Aesar, catalog No. 11890, $231 for 5 gram) in 50 mL deionized water.
6. Add the iridium chloride precursor solution to the citrate solution while magnetic stirring.
7. Magnetically stir the solution at 400 rpm at 90°C for 4 hours. Don't close the bottle lid: in other words, keep it open and just cover it with aluminium foil.
8. Cool the solution in a water bath at ambient temperature. Use an autoclave bin.
9. Stir with 20 gram of ion-exchange resin Monobed MB-1 (BDH Chemicals) to remove excess citrate for 1 h and then filter the resin out.
10. Dilute to 350 mL and add 10 mL of 6% hydrogen peroxide (H_2O_2) (Mix 2 mL 30% H_2O_2 with 8 mL water).
11. Stand overnight for complete decomposition of the hydrogen peroxide.

Appendix D

Oxygen Evolution Measurement

1. Prepare oxygen evolution buffer (2.5×) without sodium persulfate.
   (a) Clean 1 liter amber bottle and a magnetic bar.
   (b) 117.5 grams sodium sulfate (1.25 M, Na_2SO_4) (FW 142.04, Mallinckrodt Chemicals, catalog No. MK802406). It may take about 30 min to dissolve it with magnetic stirring.
   (c) 3.8 grams sodium borate (4 mM, $Na_2B_4O_7$ $10H_2O$, Molecular Weight: 381.37, EM Science, catalog No. SX035511).
   (d) Add reagent grade deionized water to approximately 900 mL.
   (e) Adjust pH to 11.0 with 10 N NaOH (about 2 mL).
   (f) Add water to 1.0 liter.
2. Clean and dry a glass vial.
3. Put 100 mg sodium persulfate (sodium peroxydisulfate, FW 238.10, 98%, Alfa Aesar, stock No. 54100 or L15748) into a transparent glass vial (1 × = 29.8 mg so 95 mg = 3.18 ×).
4. Add 10 mL 2.5 × oxygen evolution buffer to a clean glass vial.
5. Add 5 mL iridium oxide colloids.
6. Add 10 mL Milli-Q water.
7. Add 600 μL 8 mM ZnDPEG (Zn(II) deuteroporphyrin IX-2,4-bis ethylene glycol, $C_{34}H_{36}N_4O_8Zn$, FW 694.04), Frontier Scientific, Inc. (catalog No. ZnD630-9, $84 for 25 mg, http://www.frontiersci.com/)).
8. Wrap it with aluminium foil.
9. Make sure two valves in a nitrogen tank are open (pressure gauge = a little above 5 psi).
10. Put the gasket into the cap (it can be prepared using No. 12 and 22 punches).

11. Connect the vial with the cap unit.
12. Completely seal the sample assembly. If bubbling stops, the sealing and the nitrogen pressure are good.
13. Connect the flow controller. It must say around 200. If not, check vial sealing and nitrogen pressure.
14. Set up a condition in the computer.
    (a) Duration: 720 min
    (b) Step length: 1 second
    (c) Turn light on after : 120 min
    (d) Turn light off after 600 min
15. Click the start button.
16. After the measurement, name and save the data manually.
17. Save experiment.
18. Unplug the flow controller (important - do not turn off the nitrogen gas pressure.)
19. Recover your sample.